Chapter 5

Eastern Mediterranean Oil Spill Accident

This chapter is based on the results described in (García-Sánchez et al., 2022b). To ensure that everything is complete and precise, the methodological aspects discussed in Chapter 2 and the results in Chapters 3, 4 used in this chapter are reviewed for better understanding.

At the beginning of 2021 the coastline of several Middle Eastern countries in the Eastern Mediterranean was affected by the presence of oil from unknown source(s). Figure 5.1 illustrates the affected geographical areas marked with pink and yellow bullets. A more detailed report on the impacted zones along the Israeli coast may be found in the interactive map whose link is provided in (Sarah Ben-Nun , 2021). Israeli authorities estimated that more than 1000 tons of tar (Z. Rinat and A. Ben Zikri, 2021) landed along 180 km of the israeli and lebanese shoreline (Kaplan-Zantopp, 2021; News Agencies, 2021; Polidura, 2021; Rutgers Staff, 2021; T. Joffre and R. Tercatin , 2021; Tercatin, 2021) in mid February. Gaza also reported that similar arrivals of tar reached their beaches days afterwards (Monitor, 2021). This sequence of events has caused one of the worst ecological disasters reported in decades in the affected countries, which will require years of cooperative action for the affected areas to be restored (Z. Rinat and A. Ben Zikri, 2021). Numerous photographs and visual material documented the nature of the oil and actions taken by governments to mitigate the disaster (Kaplan-Zantopp, 2021; News Agencies, 2021; Polidura, 2021; Rutgers Staff, 2021; T. Joffre and R. Tercatin , 2021; Tercatin, 2021; Wikimedia Foundation, 2021). The type of tar visible on the images is consistent with a degradation of the released oil for time periods of around a month.

What was the origin of these spills? Perhaps they could have been a ‘deliberate’ oil spills, in line with findings by Pavlakis et al. (1996) who report that such oils spills appear with considerably higher frequency than oil spills corresponding to ship accidents. Also these could have been caused by operative discharges from ships, since according to the ESA (1998) 45% of the oil pollution comes from these. There exist systematic efforts to prevent

such events. Such as, for instance, the activities of the CleaSeaNet Service of the European Maritime Safety Agency (EMSA), operating since 2007, to locate and identify polluters in areas under their jurisdiction. EMSA received a request from the Israeli authorities concerning this particular event (T. Joffre and R. Tercatin , 2021).

Is any attempt to reconstruct the sequence of events of this spill with the available information doomed to failure? Indeed, there exist recent examples in the literature that confirm that predictions on oil spill evolution still raise big questions. For instance, in 2015 the fishing ship Oleg Naydenov caught fire and sank in the south of Gran Canaria. There exist models for the spreading of the oil that however did not report neither the date or its arrival point to the coast of Gran Canaria (Ivorra et al., 2017); in 2018 the Iranian oil tanker Sanchi collided with a cargo ship, caught fire, and sank in the East China Sea. After the event, researchers tried to assess where pollutants from the Sanchi would travel, but there was no consensus between predictions from groups in China and the United Kingdom (Carswell, 2018); recently, on August 23rd, 2021 a spill from Syria's largest refinery spread across the Mediterranean. Predictions expected its arrival to Cyprus on the 31 August 2021 (CMCC et al., 2021), however by the 6th of September 2021 such a landing had not yet been reported (Kundu, 2021). Many other examples could have been added to this list. One aspect that makes the pollutant event addressed in this article particularly challenging is the fact that the date and geographical location where the spill, or the spills, were released are unknown. That is, if oil spills, such as those just quoted, are difficult to predict even if the time and position of the event that has produced them are known, the difficulty increases substantially if this information is not known.

The first models for oil spill spreading used simplified linear superposition techniques to model ocean currents that employed a vector sum of the mean flows, tides, wind/waves and turbulent dispersion (Asce, 1996; Stolzenbach et al., 1977). In contrast, nowadays there exist sophisticated models that integrate all these effects to predict ocean currents and all relevant ocean variables. These models are run operationally and provide unprecedented conditions to produce accurate oil spill predictions. One natural question in this context is if it is possible to provide answers for the event under consideration with currently available tools? Among these are those provided by Copernicus, one of the most ambitious programmes in Earth Observation (European Commission, 2014). Copernicus encompasses the Sentinel programme, which provides very high-resolution satellite images in radar and visible frequencies, and the CMEMS, which provides data on ocean currents on a daily basis. Despite the availability of these new products, oil spill forecasts are still uncertain since the underlying ocean flow, and the associated transport, is very chaotic. Importing into this setting dynamical systems concepts, which use concepts from chaos theory, may

provide a wealth of new ideas that could assist in this struggle. One of these consist of identifying geometrical features on the ocean surface that help to interpret colectively the behaviour of masses of fluid parcels, instead of considering individual fluid trajectories. The development of these geometrical ideas was begun by Poincaré in the context of his work on celestial mechanics. In the setting of geophysical flows these geometrical structures have been referred to as Lagrangian Coherent Structures (LCS). For oil spills this global vision has provided very satisfactory results. Using this perspective García-Garrido et al. (2016) were able to identify the date and arrival point of the oil to the coast of Gran Canaria after the Oleg Naydenov fishing ship accident; García-Sánchez et al. (2021) used this viewpoint to describe the Volcan Tamasite event and to compare the performance of different ocean models (García-Sánchez et al., 2022a). It is important to remark that these episodes occurred in different space and time scales ranging from the mesoscale, to the submesoscale, and from hours to days. Above the mesoscale Olascoaga and Haller (2012) found that oil in the Gulf of Mexico, released after the Deepwater Horizon accident, was lined up with configurations obtained from LCS, which highlighted attracting material curves. Notably this approach has succeeded for events that involved different type of oils, from light fuel oil in (García-Sánchez et al., 2021), to denser IFO 380 oil (García-Garrido et al., 2016) and to a variety of crude elements (Olascoaga and Haller, 2012). Encouraged by these results we will address the description of the oil spill event described above. With the aid of LCS we identify attracting material curves along which oil spills tend to become aligned (see García-Sánchez et al. (2022a); Olascoaga and Haller (2012)). Indeed, this article reports strong correlations between satellite observations and attracting material curves highlighted by LCS computed with the CMEMS data. These connections have been very valuable for identifying the sources of the contamination event. The agreement between satellite observations and modelling results supports the correctness of our approach. It is expected that these scientific and technological advances will be systematically implemented in the near future and will allow investigators to identify violators and take appropriate measures to protect the environment.

5.1. Satellite Data

During the time period and geographic region of interest a set of publicly available satellite data has been analyzed. The aim was to identify spills on the sea surface that could be linked to the reported spills along the coastline.

One source for these satellite images is the Synthetic Aperture Radar (SAR) high-resolution data from Sentinel 1 (A,B), Level-1 IW GRDH (Interferometric Wide Swath Ground Range Detected). SAR data were processed using the SNAP - ESA Sentinel Ap-

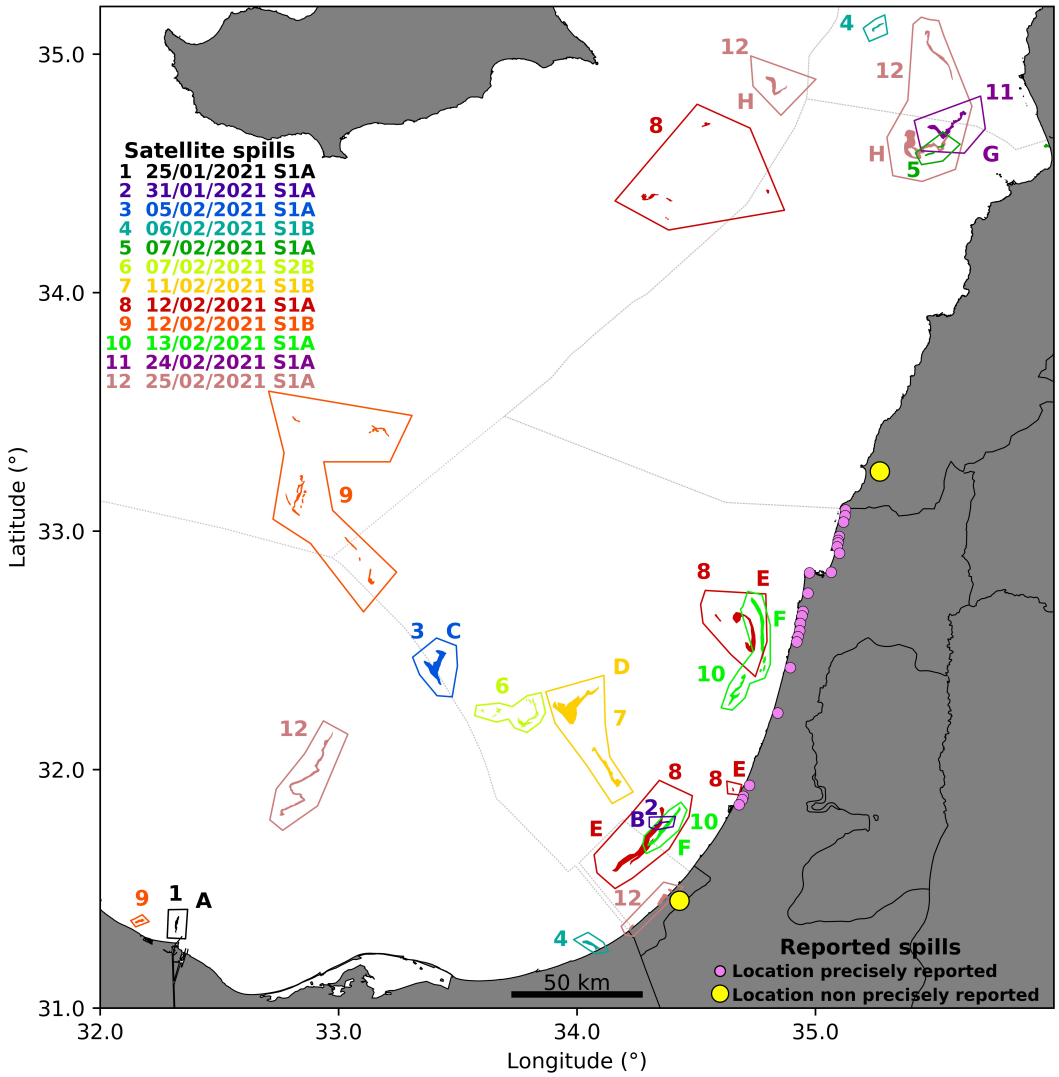

Figure 5.1 Scenario of affected areas. Exclusive Economic Zones (EEZ) are marked with a dotted line. Pink and yellow bullets mark coastal areas for which, according to mass media reports, there were in situ observations of oil or tar. Satellite observations are listed with numbers and colors according to the day in which they were detected. Some of them are double labelled with a letter since they are also reported in Figure 5.2. The figure has been created using python 3.8.10 and matplotlib module 3.1.2 (https://www.python.org/downloads/release/python-3810/). Coastlines and country boundaries have been obtained from GSHHG - A Global Self-consistent, Hierarchical, High-resolution Geography Database 2.3.7 version (https://www.ngdc.noaa.gov/mgg/shorelines/gshhs.html). EEZ have been obtained from https://www.marineregions.org/. The satellite observations vector representations have been created using QGIS software 3.10 version (https://qgis.org/) and the SAR processed images.

plication Platform v8.0.3 Graphics Processing Tool (GPT) operators [https://step.esa.int/main/toolboxes/snap/]. During the study period there were days around the third week of February in which, due to the atmospheric conditions, SAR images were not useful. The occurrence of storms, and their associated strong wind fields, produced atmospheric signals that were detected in SAR images. This prevented the information corresponding to surface sea phenomena from being showed. For this reason, SAR images interpretation require wind field data, and to support SAR image analysis, wind data with moderate resolution were obtained from Copernicus Marine Segment [https://marine.copernicus.eu/]. The selected product is identified with product code 012_004V6. This product corresponds to global near real time wind data every 6 hours with a spatial resolution of one-quarter degree. This product combines data from wind models of the ECMWF (European Centre for Medium-Range Weather Forecasts) with data from available wind scatterometers. Additionally, instantaneous wind fields were derived from SAR data using the corresponding GPT operator.

Both mineral oil and biogenic slicks are visible in SAR images at moderate wind speeds. The wind range for which both types of slicks are recognizable is not the same, although they overlap. In order to contradistinguish mineral oil slicks from natural origin surface films, the SAR images were analyzed not only with available wind fields but also with ocean colour data. To this end, Sentinel 2 (A, B) optical data from MultiSpectral Instrument (MSI) Level 1C and Sentinel 3 (A,B) Ocean and Land Colour Instrument (OLCI) Level 1B were downloaded from the Sentinel Data Hub [https://scihub.copernicus.eu/]. Sentinel 2 MSI data atmospheric correction was conducted using(Vanhellemont, 2019) the acolite toolbox [https://odnature.naturalsciences.be/remsem/software-and-data/acolite]. Sentinel 3 OLCI data were processed using SeaDAS 7.5.3 version [https://seadas.gsfc.nasa.gov/].

5.2. Satellite Results

Figure 5.2 displays a set of satellite images selected in the area and period of interest after performing the analysis described above. This selection is chosen also in the light of the numerical simulations reported next. Panel a) shows a spill detected close to the Suez Canal on the 25th of January 2021. As we will argue in the discussion, this spill has been detected shortly after its release and marks the origin of some of the spills that reached the coastline. Panel b) shows a second spill closer to the coast on the 31st of January 2021. As discussed later we conjecture that this observation is a second origin for those spills that reached the coastline. Panel c) displays one spill visible on the 5th of February 2021. Panel d) identifies spills on the 11th of February, not too far from the position in c). Panel e) shows spills very close to the Israeli coast on the 12th February 2021. Panel f) shows the evolution of these

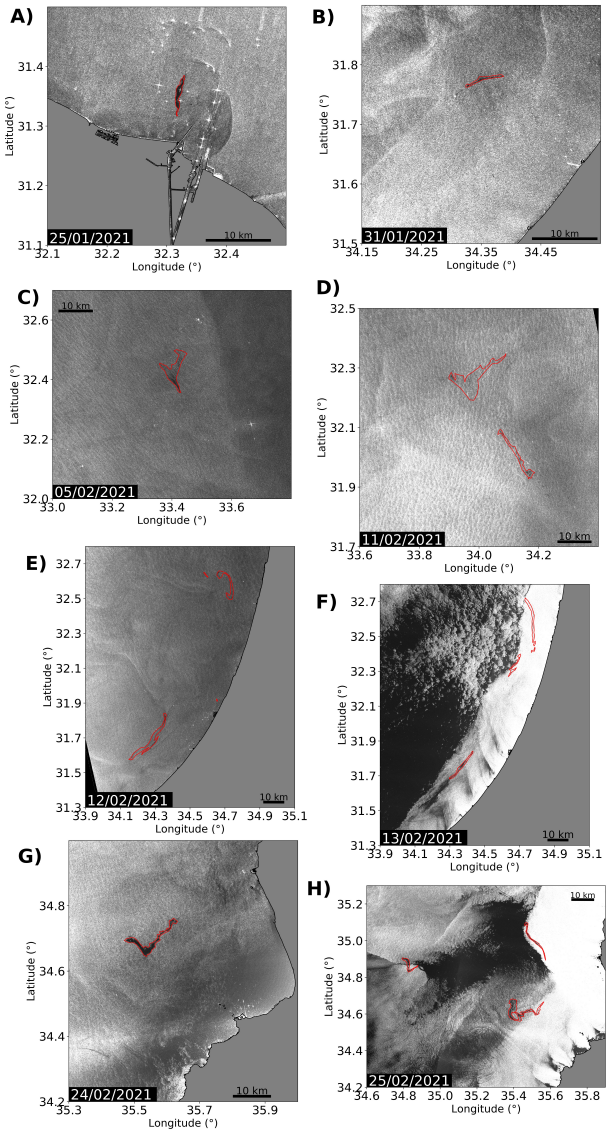

Figure 5.2 Satellite radar images. a) Sentinel 1A on the 25th January 2021; b) Sentinel 1A on the 31st January 2021; c) Sentinel 1A on the 5th February 2021; d) Sentinel 1B on the 11th February 2021; e) Sentinel 1A on the 12th February 2021; f) Sentinel 1A on the 13th February 2021 ; g) Sentinel 1A on the 24th February 2021; h) Sentinel 1A on the 25th February 2021. The figure has been created using python 3.8.10 and matplotlib module 3.1.2 (https://www.python.org/downloads/release/python-3810/). Coastlines have been obtained from https://osmdata.openstreetmap.de/data/land-polygons.html. The satellite observations vector representations have been created using QGIS software 3.10 version (https://qgis.org/) and the SAR processed images.

spills on the 13th February 2021. Panels g) and h) show a sequence of images detected close to the Syrian coast on the 24th February and 25th February 2021, respectively.

Spots in Figure 5.2 are displayed by zooming into smaller areas. In order to acquire a vision of their global distribution they are also represented in Figure 5.1. Figure 1 shows the position of all spills located from satellite images in the Eastern Mediterranean during the period of interest. Each shape appearing in Figure 5.2 is labelled in Figure 5.1 with the same letter. Figure 5.1 shows additional spills, some of them reported in the media (Surkes, 2021), for which we have not found relations to their arrival to the shoreline. These are labelled only with numbers, and their observation day is listed in the figure. Satellite images confirm that waters of the Exclusive Economic Zones (EEZ) of Egypt, Syria and Cyprus were also affected, and not only those of Israel, Gaza, and Lebanon. In this figure it is remarkable that spills in panels a) and b), which we have identified as the *sources*, are seen very small when compared to others. We remark that according to Schrope (Schrope, 2013) spills are often larger than detected, and their size very often is not correctly determined from remote sensing images. This is particularly true at the early stages when their spreading in the ocean surface has barely started. On the other hand, structures displayed in panels c), d), e), f), g) and h), which are more extended and present distorted shapes, suggest that they have been affected by the chaotic motion of ocean transport.

5.3. The transport problem

One natural question regarding those oil spills observed by satellite and at the coast is whether they are connected among themselves? Are they part of the same event? We provide answers to these questions in this section.

Oil transport can be described by a concentration field, C, whose evolution is affected by the flow, represented by the velocity field $\mathbf{v}(\mathbf{x}(\mathbf{t}),t)$, and molecular diffusion. At the ocean scales under consideration, the diffusion transport is much smaller than the convective transport (Monroy, 2019) and therefore it can be neglected. On the other hand, particles with a finite size and different density to that of water may not instantly follow fluid velocities: other mechanisms besides passive advection contribute to their transport, such as gravity forces, their finite size, inertia and history dependence, etc. Results in (Monroy et al., 2017) confirm, however, that for a wide range of particles, the description of passive tracers is appropriate, except for the addition of a constant vertical velocity arising from the particle weight. However, for the case under study, that correspond to oil that remains floating for a long time, weight effects should be negligible and therefore we considered that it closely follows the 2D horizontal motions of fluid parcels. This is a simplified approach, but studies such as (García-Garrido et al., 2016; García-Sánchez et al., 2021; Lekien and Marsden, 2005; Olascoaga and Haller, 2012) confirm that considering horizontal advection as the

dominant contribution to pollutant transport provides very good results. Similar approaches in other contexts of ocean transport confirm the same (Garcia-Garrido et al., 2015). Finally, we will assume that the crude oil moves horizontally, close to the surface, but a bit below the waterline and therefore it is not subjected to direct wind sailing effects. Wind effects, jointly with tides, waves, etc., are included in the sophisticated ocean models that provide the velocity fields of the ocean currents, $\mathbf{v}(\mathbf{x}(\mathbf{t}),t)$, (see Section 5.4 below for more details) and we assume that oil parcels follow instantly water fluid velocities. The accuracy of this approach is supported, by the agreement between the predictions made by the simulations, the oil sightings from satellite and in situ observations. Under this approach oil parcels follow trajectories $\mathbf{x}(\mathbf{t})$ that evolve according to the dynamical system:

$$\frac{d\mathbf{x}}{dt} = \mathbf{v}(\mathbf{x},t) \tag{5.1}$$

In this equation the position $\mathbf{x}$ is described in longitude (λ) and latitude (ϕ) coordinates, that is, $\mathbf{x} = (\lambda,\phi)$, and $\mathbf{v}$ represents the velocity field. In longitude/latitude coordinates, the dynamical system (5.1) can be rewritten as:

$$\frac{d\lambda}{dt} = \frac{u(\lambda,\phi,t)}{R\cos(\phi)}, \quad \frac{d\phi}{dt} = \frac{v(\lambda,\phi,t)}{R}, \tag{5.2}$$

where R is the Earth's radius. This system assumes that the vertical velocity component in the ocean is small compared to the horizontal ones and for that reason it has been disregarded. The two velocity components are determined by the zonal (u) and meridional (v) velocities, which are obtained from the currents provided by CMEMS.

There exist diverse software packages that are able to track oil spills, of which for instance a list is found in (García-Sánchez et al., 2021). Most of these models are focused on tracking individual fluid parcels, and in order to maintain a good representation of the spill they play with a sufficiently large number of initial parcels. Contrary to these approaches, in the results reported in this work, we track in time the whole area where the fuel is extended, and the algorithm self regulates the number of fluid parcels on the contour to ensure its accurate representation at all times. At the beginning the area is a simple shape, but while it evolves, it becomes distorted and convoluted. The shape is tracked with contour advection algorithms developed by Dritschel and Ambaum (1997), including some modifications explained in (Mancho et al., 2004, 2006, 2003). Typical oil spill software packages include models to represent the weathering process according to different oil properties. In our approach we do not describe oil transformation. We consider that weathering does not affect to the transport process. Spill contours are evolved uncoupled from degrading effects. Degrading effects

could have been considered at representative levels *a posterior* (García-Sánchez et al., 2021) as a change in the color intensity of the oil spill. It could be that weathering implies oil evaporation, and in that case the evolved contour would be an upper bound to the oil evolution. Similarly would occur if oil forms clots that are denser and sink. In both cases the region of dispersion for the oil is a subset of our approach. Given that we do not have information on the type of floating oil and our focus is just on transport.

5.4. Ocean Data

The ocean velocity fields used in this work were obtained from the CMEMS [http://marine.copernicus.eu/]. In particular, we have used the datasets provided by the high-resolution Global Ocean Model (the global analysis and forecast product). The horizontal resolution of the model is 1/12° (approximately 8 km) with regular longitude/latitude equirrectangular projection and 50 vertical geopotential levels. Data are served on a daily and hourly basis. Hourly data rapidly fluctuate around daily data, which represent smooth averaged values. All the calculations reported in this article have been performed with the daily data, because they better match observations. Additionally, CMEMS provides a specific service with hourly and daily data for the Mediterranean area. The resolution of the Mediterranean Model is higher than that of the Global Model: on the horizontal plane it is 1/24° with regular longitude/latitude equirrectangular projection and along the vertical coordinate it has 141 depth levels. This resolution allows a representation of sub-mesoscale features, however calculations performed with the Mediterranean Model do not reproduce many of the transport features related to the oil spill event. Additionally we have found that small scale features from this Model do not accurately correspond to those observed from satellites.

5.5. The Dynamical Systems Perspective

A challenge to studying Equation (5.1) is that even flows with smooth velocity fields may exhibit complex particle trajectories. An approach taken from nonlinear dynamical systems theory, seeks to understand the behavior of large ensembles of particle trajectories by finding geometrical structures, known as Lagrangian Coherent Structures (LCS), that form time dependent material surfaces. This perspective has been successfully employed in pollution contexts (García-Garrido et al., 2016; García-Sánchez et al., 2021; Lekien and Marsden, 2005; Olascoaga and Haller, 2012). The LCS spatio-temporal template can be constructed with a recent technique referred to as Lagrangian Descriptors (LDs). The particular LD that we use is a function referred to as M (Madrid and Mancho, 2009; Mancho et al., 2013;

Mendoza and Mancho, 2010) which is defined as follows:

$$M(\mathbf{x}_0, t_0, \tau) = \int_{t_0-\tau}^{t_0+\tau} \|\mathbf{v}(\mathbf{x}(t), t)\| \, dt = \int_{t_0}^{t_0+\tau} \|\mathbf{v}(\mathbf{x}(t), t)\| \, dt + \int_{t_0-\tau}^{t_0} \|\mathbf{v}(\mathbf{x}(t), t)\| \, dt \,, \tag{5.3}$$

Singular features visible in this field represent attracting and repelling material surfaces. Of particular interest for our study are attracting material surfaces, visible from the backward integration (the second term) of Equation (5.3), along which oil blobs eventually tend to be elongated and aligned. More specifically, there exist regions in the ocean, characterized by high contraction and expansion rates, referred to as hyperbolic regions, such that blobs placed in the neighbourhood of trajectories in these regions (hyperbolic trajectories) evolve in time rapidly expanding and filamenting to become aligned with the attracting material curves. This effect has direct implications on our study since blobs that are originally located in small ocean regions, if they go close to these expansive/contractive regions, will spread in filaments affecting large sea areas. Alternatively, repelling material curves are obtained from the forward integration (the first term) of Equation (5.3). These curves describe how blobs placed in the neighbourhood of the hyperbolic region evolve in backward time. They also tend to form filaments, but as these are formed in reverse time, they are not observable and for this reason they are referred to as repelling material curves. A physical way to look into these curves is as follows: material spread on the ocean surface lined up with these filaments evolves in time contracting towards the neighbourhood of the hyperbolic trajectory.

The computation of fluid particle trajectories $\mathbf{x}(t)$ is necessary in order to evaluate the function M in Equation (5.3). For a given initial condition $\mathbf{x}_0(t)$ this function evaluates the arc length of trajectories when they are evolved forwards and backwards in time for a period τ. Trajectories are integrated with a 5^{th} order Runge-Kutta method, and arc length is computed by the addition of linear segments connecting successive steps of the Runge-Kutta method.

5.6. Transport Results

Figure 5.3 represents in gray tones the field M as evaluated from Equation (5.3) with $\tau =$ 15 days, which is a choice appropriate for the time scale of the described events (1 month). In maroon tones are highlighted the attracting material curves. Repelling material lines are also visible, but we do not highlight them as they are not of interest for our discussion at this moment. This figure represents the time evolution of orange and blue blobs that have

been released on the 25th and 31st of January, respectively, at the positions marked in panels a) and b), which are linked to spills detected in panels a) and b) of Figure 5.2. Initial blobs have a radius of 4 km, in agreement with the resolution of the CMEMS global model. It is clear from the evolution that blobs tend to end up elongated and aligned with the maroon features of the attracting material curves. Panel c) illustrates the evolution of these blobs on the 12th of February and the red shapes highlight satellite spills spotted on that day. The good agreement between parts of the evolved orange and blue blobs and these spills is remarkable. Panels d) and e) illustrate their evolution on the 16th and 17th of February and the arrival to the Israeli coast at points marked in pink and also reported in Figure 5.1. Panel f) illustrates the arrival at further points on the Israeli and Lebanon coasts on the 20th of February, in good agreement with reports marked in Figure 5.1.

Figure 5.4 is similar to Figure 5.3. It also represents in gray tones the field M and the attracting material curves highlighted in maroon. Panels a) and b) complete the description of Figure 5.3. Panel a) illustrates the blue and orange blobs on the 24th of February. Their structure is extremely filamented, closely following the attracting material curves. The red shape illustrates the spill visible in panel 5.2g) suggesting that this could have been related to the spill detected in panel 5.2b), associated with the blue blob. Panel 5.2h) confirms the connection between the "V" shaped spill in g) with the one observed in h) confirming the quality of the model (5.1) to provide a consistent connection of this spill with what is obtained from satellite observations. In this panel it is also remarkable the proximity between all satellite observations (in red), the blue blob and the attracting material curves. This suggests that these spots observed on the 25th of February close to the Syrian coast could also been related to the spill detected in Figure 5.2b). Finally on the Gaza coast are visible two red spots that highlight satellite observations of oil. There is a remarkable agreement between these observations and the spreading of the orange blob.

Panels c) and d) illustrate the position, respectively, of spills detected in panels c) and d) of Figure 5.2. The green blob in panel 5.3c) is released at the position of the spill of panel 5.2c) on the 5th of February and its evolution on the 11th of February according to the model (5.1) is illustrated in panel 5.3d). It is remarkable the connections established by the simulations between both satellite observations, suggesting that these spills correspond to the same event. Also we want to emphasize that these spills are not related to spills arriving to the coast. Arrivals to the coast are only achieved by the blue and orange blobs visible in Figure 5.3 and in panels a) and b) previously discussed. The movie supplied in the supplementary material completes the description given in Figures 5.2 and 5.3.

In all panels of figure 5.3 there exist V-shaped observed satellite spills. We conjecture that these shapes are again an effect of advection dominated transport. Indeed the convoluted

forms adopted by blobs while being transported, visible in Figures 5.2 and 5.3, present many corners with this kind of shape, at different orientations. Even the green blob in panels 5.3c) and d) is distorted into a V-shape. 'V' shapes are a footprint of typical stretching and folding mechanisms related to hyperbolicity and non-linearity present in equations like (5.1), adopted to describe oil transport (Ottino et al., 1994).

Finally, we discuss the perspective that searches for contamination sources by considering backwards integration of trajectories in the spirit of (Shu et al., 2018, 2014). Figure S1 [1] shows these results. Panel a) of this figure locates a blob in the neighbourhood of the Israeli coast on the date that tar was reported to reach the beach, the 16th February 2021. Panel b) in this figure, represents the backward evolution of this blob on the 31st January 2021. As anticipated, the backward evolution of the original blob becomes aligned with the repelling material curves that are highlighted in blue in the figure and spread over a large ocean region. This points out the difficulty in locating the spill point through this methodology.

5.7. Discussion and Conclusions

This paper discusses our findings concerning a recent oil spill event that we have studied by importing dynamical systems ideas. We have found evidence that our perspective recovers the essential features of the oil spill dispersion at large scale. Indeed oil spills form clots and its pieces tend to be aligned with segments of attracting material curves, Lagrangian Coherent Structures, confirming the assumptions. Indeed, the attracting material curves of the CMEMS Global model are closely related to SAR satellite spill observations for this Eastern Mediterranean event. Remarkably, several of these observed scattered spills emerge from two particular observations on the 25th and 31st January 2021 and are directly linked to the coastal spill arrivals. We also find that some observations of spills on the 5th and 11th of February 2021 visible from Sentinel SAR images are unrelated to spills observed at coastal points, however they seem to be connected between themselves. The entire description of the event, according to our findings, spans a period of almost one month and this is consistent with the fact that what has been reported to reach the coast is tar, a form of degraded oil after several weeks on the sea surface.

Connections and links between scattered pieces of oil observed from satellites and on coastal arrivals have been established for the CMEMS global model. However these types of connections are not found from other CMEMS models such as that in the Mediterranean sea domain. This suggest that CMEMS global model is particularly good for describing transport phenomena.

[1] This figure is available via the following hyperlink: https://shorturl.at/ruGK9

Dynamical system tools have provided concepts such as that of attracting material curves which have provided a simple global overview of the event and suggested connection routes for dispersed and scattered spills, helping to answer questions about where and when the spill originated. It is remarkable that these connections have been established for events that extend for a one month period, taking oil spill forecast capacities to their limit (Barker et al., 2020).

As a conclusion we have found that the synergistic combination of Copernicus services has provided a powerful technology that should be exploited in an operational manner to better predict and target the evolution at sea of spill events. These technologies will allow a better environmental protection of all seas and coasts, given that, as in this case, oil spills pay no attention to international borders.

In this chapter, we have presented our findings on the analysis of a recent oil spill event using dynamical systems concepts. In the next, we propose a new uncertainty measure to evaluate the performance of CMEMS Global and Mediterranean models in assessing the origin of observations. We call the proposed measure Backward Lagrangian Uncertainty Quantification (BLUQ) and is related to the invariant dynamical structures of the model in the neighborhood of the observation. We illustrate the implementation of this measure in the context of this oil spill event in the Eastern Mediterranean in 2021, providing a quantitative analysis of the performance of ocean data sets. Our approach provides a promising tool for evaluating the accuracy and reliability of models in predicting the origin of observed material transport events, and can contribute to better environmental protection of seas and coasts.

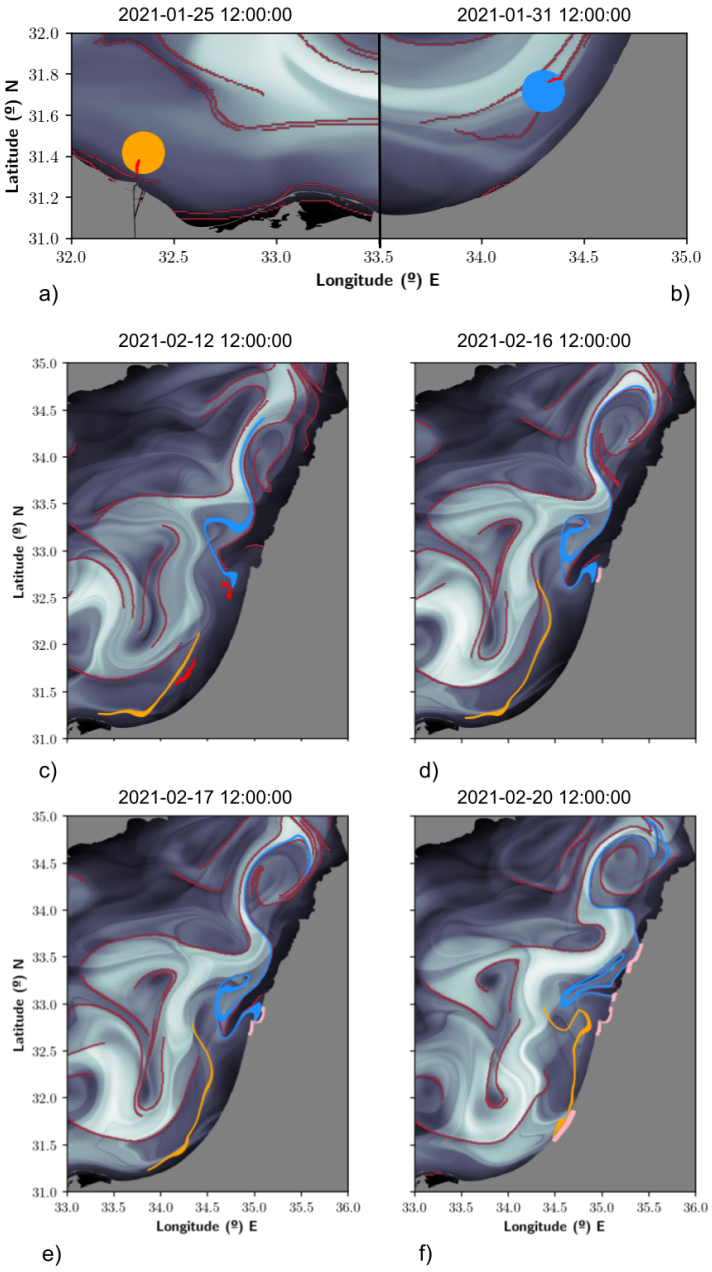

Figure 5.3 Simulations that reproduce the spreading on the sea and the arrival of the oil to the coast. The function M at the background is represented at t_0 equal to the corresponding date. a) 1st release on the 25th January 2021 and satellite observation; b) 2nd release on the 31st January 2021 and satellite observation; c) evolution on the 12th February 2021 and satellite observations; d) evolution on the 16th February 2021 and arrival to the coast; e) evolution on the 17th February 2021 and arrival to the coast; f) evolution on the 25th February 2021 and arrival to the coast. These masks indicate regions that correspond to the continental shelf. These figures have been created with Python 3.9.2 (https://www.python.org/downloads/release/python-392/). The maps shown have been generated with a mask provided by OpenStreetMaps (https://osmdata.openstreetmap.de/data/land-polygons.html).

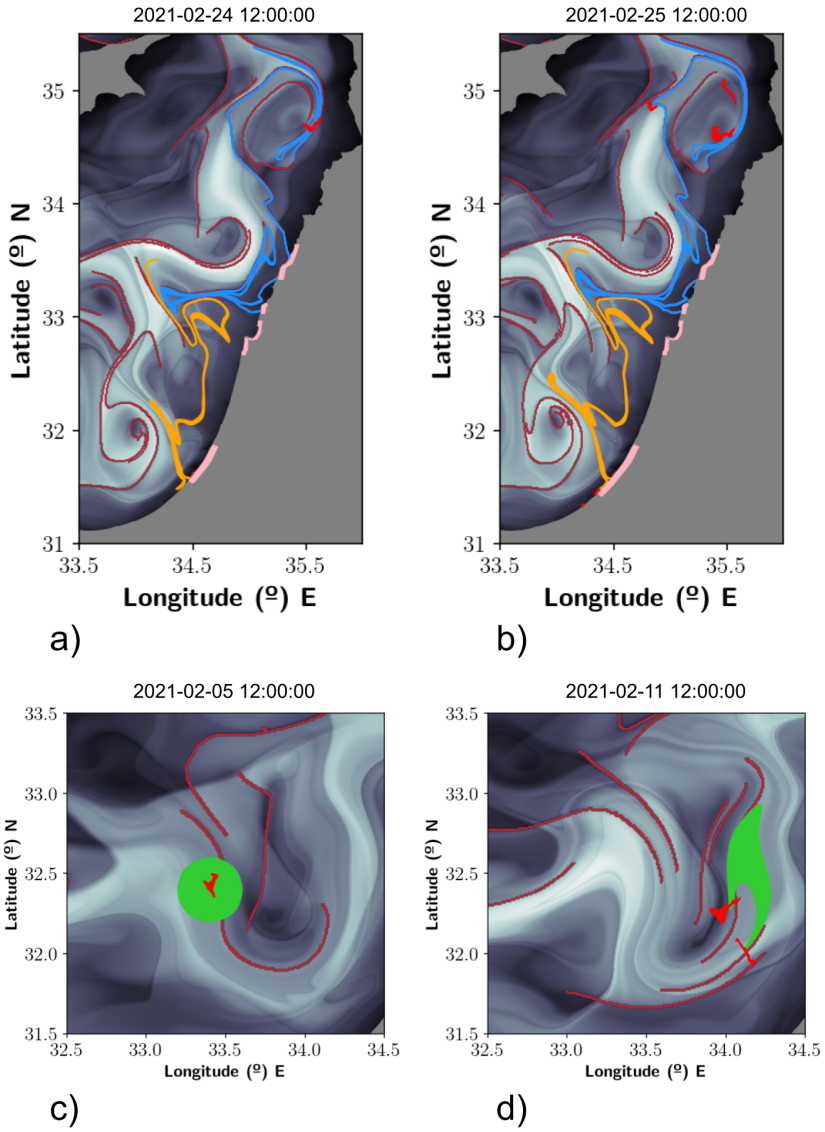

Figure 5.4 Simulations that connect successive oil spill observations. The function M at the background is represented at t_0 equal to the corresponding date. a) Evolution on the 24th February 2021 and satellite observations; b) evolution on the 25th February 2021 and satellite observations; c) satellite observation on the 5th February 2021 and a 1st release attached to the observation; d) evolution on the 11th February 2021 and satellite observations. These figures have been created with Python 3.9.2 (https://www.python.org/downloads/release/python-392/). The maps shown have been generated with a mask provided by OpenStreetMaps (https://osmdata.openstreetmap.de/data/land-polygons.html).

Chapter 6

Backward Time Lagrangian Uncertainty Quantification

This chapter is based on the results described in (García-Sánchez et al., 2023a). To ensure completeness and accuracy, methodological aspects discussed in Chapter 2 and the results in Chapters 4, 5 are recalled.

Models in real-world applications are subjected to uncertainty in their results, and this is particularly notorious in models that describe the ocean or the atmosphere state. In these geophysical contexts, the availability of tools that quantify the uncertainty of model outputs is very much desired as this allows the evaluation of their reliability and the assessment of their use in real applications. Uncertainty quantification is a very broad question and it has been addressed from different perspectives. One approach to this problem involves performing a sensitivity analysis, which determines what inputs in the model, which typically is a partial differential equation, affect the outputs the most. A related issue, referred to as forward propagation of uncertainty, consists of examining how uncertainty in the model parameter inputs affects uncertainty in the model outputs. In this framework it may happen that experimental data are available. In this case, it is possible to infer the set of parameters that better fit the outputs for the proposed model. This setting can be precisely formulated as a Bayesian inverse problem, which for a given observation, and an assumed noise model, determines the parameters that are most likely to have produced the data. Typically, Bayesian analyses provide the framework for many inverse uncertainty quantification applications (Domitr et al., 2022; Wu et al., 2018). These methods employ Bayesian inference theory along with exploring the posterior Probability Density Function (PDF) by Markov Chain Monte Carlo (MCMC) sampling. Other methods include statistical methods based on maximum likelihood estimation (MLE) (de Crècy, 1996) and data assimilation methods. Data assimilation methods combine experimental observations with code predictions and their

respective errors to provide an improved estimate of the system state and of the associated uncertainty (Petruzzi, 2019). All of these approaches assume that the model is known, with undetermined parameters, and perform adaptations on the model inputs. However, there is a different type of problem for which only an approximate model is available and its exact expression is unknown. We delve into an explanation of such problems.

Recently, García-Sánchez et al. (2022a) have proposed to quantify uncertainty associated with transport by currents in settings in which the exact model connecting two successive observations (or the currents producing the observed transport) was not known. They have quantified uncertainty motivated by the need to judge the performance of ocean model outputs to describe oil spill events such as that described in (García-Sánchez et al., 2021). In this reported event an identified spill occurs at a certain time and it is required to describe its evolution to determine if it will affect critical areas, and there is a need to assess ocean models to this end. García-Sánchez et al. (2022a) approach evaluates the reliability of the ocean currents with respect to the transport that they produce. Indeed, transport in the ocean surface is produced by fluid parcels that follow trajectories $\mathbf{x}(t)$ that evolve according to the dynamical system:

$$\frac{d\mathbf{x}}{dt} = \mathbf{v}(\mathbf{x},t), \tag{6.1}$$

This system is a nonlinear non-autonomous dynamical system in which there are uncertainties in the velocities $\mathbf{v}(\mathbf{x},t)$, because they are not exactly known given that they come from solving highly sensitive partial differential equations. This is what we mean by *not knowing* the exact problem: the right-hand side of Equation (6.1) is only an approximation. Typically, in other problems where uncertainty has been studied, the system obeys an explicitly known partial differential equation where the unknowns are not within the model itself but rather in adjustable parameters of the equation or in the observations. However, our case is of a different nature because the right-hand side of Equation (6.1) is a key part of the equation and not exactly known. The uncertainties in the velocities $\mathbf{v}(\mathbf{x},t)$ produce uncertainties in the solutions $\mathbf{x}(t)$. García-Sánchez et al. (2022a) quantified this type of uncertainty by means of error measures in settings where the initial observation was known, $\mathbf{x_0}$, and a target state at a later final time, $\mathbf{x}^*$. This approach was adequate to quantify the suitability of the model given in Equation (6.1) to represent this sequence of observations in forward time. In doing so they found links between the uncertainty and the stable invariant manifolds of hyperbolic trajectories present in the system (6.1).

This chapter aims to complete the described picture as follows. While results in (García-Sánchez et al., 2022a) consider the uncertainty of a model based on ocean currents in order to describe the final fate of an observation as it evolves *forward* in time, the new setting considers the uncertainty of a similar model in order to identify the original location of an

observation in a *past* time, once the position, $\mathbf{x_1}$, of this observation is known at the present time. In a nutshell, previous results were about: where do trajectories end up? How could it be measured if they are consistently described by a model constructed from approximate velocities? Now the results we desire are about: where do trajectories come from? how could it be measured if their origin is consistently described by a model that is constructed from approximate velocities? In this context, this chapter provides a new approach to measuring uncertainty using errors adequate for the backward time setting. We find that similar to what was found in García-Sánchez et al. (2022a), this uncertainty has a *structure* in a neighborhood of the observation $\mathbf{x_1}$, and this structure is related to the unstable invariant manifolds of the hyperbolic trajectories present in the vector field of Equation (6.1).

Once this new type of uncertainty is introduced, we proceed to assess ocean data capabilities in real events that demand this type of perspective. In particular, a recent contamination event that occurred in 2021 in the Eastern Mediterranean is considered. Specifically in this event, thoroughly described in (García-Sánchez et al., 2022b), several beaches were affected by a spill of unknown origin. In contrast to the results by García-Sánchez et al. (2022a), now observations are done at the arrival point and the identification of their source is the goal. Equipped with the new tool we describe in detail its use to quantify the performance of different ocean data sets for describing observations adequately. There are other attempts to identify the best dataset for predicting the drift of oil spills (Brushett et al., 2011; Zhang et al., 2020). However, their approach consists of using uncertainty estimators in forward time.

In summary, the goal of this article is to propose a new uncertainty measure appropriate for quantifying the suitability of a model to describe the origin of trajectories. It is found that the considered uncertainty has a structure correlated with the unstable manifolds of the hyperbolic trajectories of the model. The capacity of this new measure is exploited for characterizing the performance of ocean data sets in real events. Accordingly, the structure of this article is as follows. Section 6.1 provides a new definition for uncertainty quantification suitable to describe the new setting and, in a simple example, discusses links with unstable manifolds of hyperbolic trajectories. In Section 6.2 a formal proof of this observation is given. Section 6.3 presents the application of this tool to the mentioned oil spill event that affected the Eastern Mediterranean, and shows how it helps to discriminate between two data sets, and supports the identification of the most suitable one for searching the spill source. In Section 6.4, the chapter concludes with a discussion of the implications and potential applications of this approach.

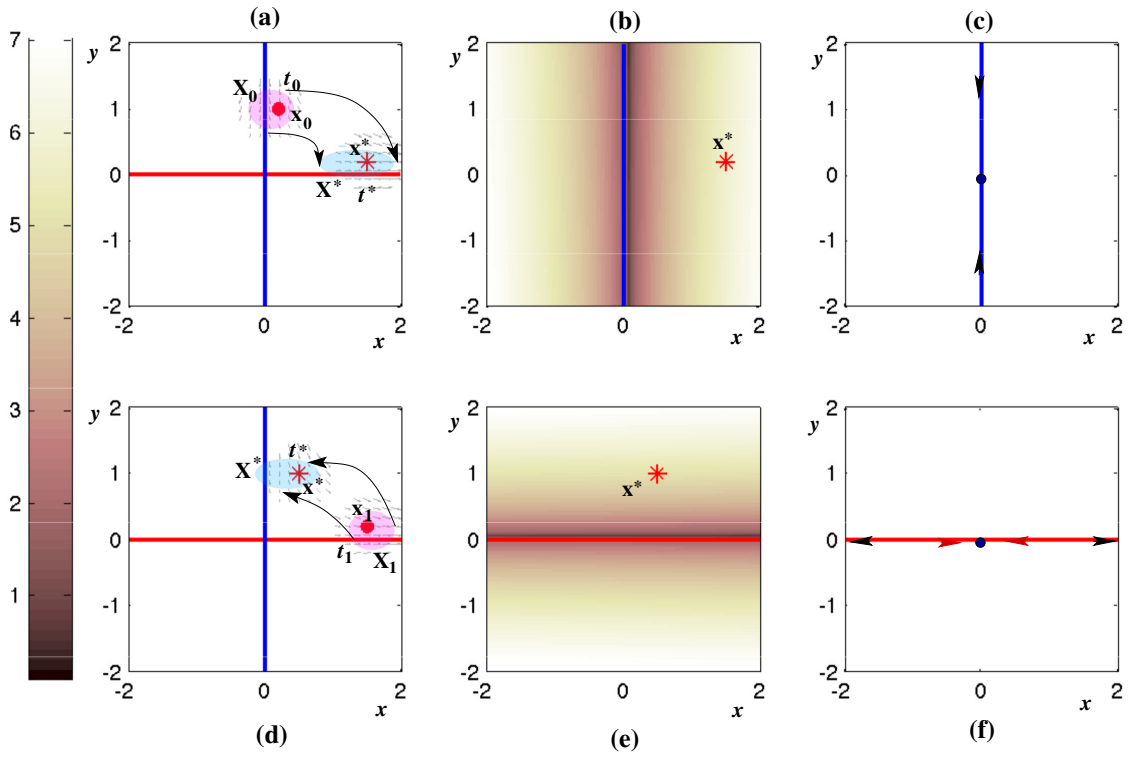

Figure 6.1 Panels a), b) and c) display a graphical representation of two sequential observations and their forward time evolution. a) The initial observation at time t_0 is expressed by the red circle with initial condition $\mathbf{x_0}$. The final observed state $\mathbf{x}^*$ at time t^* is referred to as the "target". In general, the evolution law linking these observations is unknown, but in our setting, it is approximated by Equation (6.2), a system with a hyperbolic fixed point at the origin with stable and unstable manifolds in blue and red, respectively. The forward evolution of $\mathbf{X_0}$ (the pink blob) to $\mathbf{X}^*$ (the light blue blob) according to this model is illustrated; b) a representation of L_{UQ}, in a domain beyond the neighbourhood X_0 for $\tau = 3$, where singular features are identified aligned with the stable manifold (in blue); c) a representation of the stable manifold. Black arrows point out the forward time evolution for initial condition on the stable manifold towards the fixed point at the origin; Panels d), e) and f) display a graphical representation of two sequential observations and their backward time evolution, d) the final observation at time t_1 is expressed with the red circle at the position $\mathbf{x_1}$. Although both the origin and the model of this observation are unknown, its evolution is approached by Equation (6.2), a system with a hyperbolic fixed point at the origin with stable and unstable manifolds in blue and red respectively. The backward evolution of $\mathbf{X_1}$ (the pink blob) to $\mathbf{X}^*$ (the light blue blob) according to this model is illustrated; e) a representation of L_{BUQ}, in a domain beyond the neighborhood X_1 for $\tau = 3$, where singular features are identified aligned with the unstable manifold (in red); f) a representation of the unstable manifold. Red arrows point out the evolution in backward time towards the fixed point for initial conditions on the unstable manifold. Black arrows point out the evolution forward time moving away from the fixed point. The color bar at the top indicates a color scale for L_{UQ} and L_{BUQ} in panels b) and e).

6.1. Uncertainty Quantification in Backward Time

This section is focused on proposing a new definition of uncertainty quantification to describe the uncertainty in the origin or source of certain observations based on predictions by a model constructed from velocities. This section is limited to present the definition and to discuss its implementation in one simple example. This simplified scenario enables us to establish connections between the new definition of uncertainty and the unstable manifolds of hyperbolic trajectories. The objective, however, is to apply this definition to distinguish the most appropriate velocity field among various options, the one that best matches the observations.

We start by recalling results reported in (García-Sánchez et al., 2022a) in the context of the simple example illustrated in Figure 6.1. Panel a) within this figure shows an initial observation, $\mathbf{x}_0$, at time t_0 marked with a red circle. At a later time, t^*, this observation is at a target position, $\mathbf{x}^*$, marked with a red asterisk. This evolution is assumed to be following the model provided by Equation (6.2), with a vector field in the background, which is represented at time t_0, in the neighborhood of $\mathbf{x}_0$ and at time t^* in the neighborhood of $\mathbf{x}^*$. This vector field is chosen to be stationary, therefore its representation at later times, t^*, is the same as at t_0. However, in general, this vector field will be time-dependent and therefore its representation at t^* is different from that at t_0. The explicit expression for this vector field is:

$$\begin{cases} \frac{dx}{dt} = x, \\ \frac{dy}{dt} = -y, \end{cases} \tag{6.2}$$

This system has a stable manifold aligned with the vertical axis at $x = 0$ (blue line in Figure 6.1) and an unstable manifold aligned with the horizontal axis at $y = 0$ (red line in Figure 6.1).

García-Sánchez et al. (2022a) proposed several expressions to measure the error in a neighborhood $\mathbf{X}_0$ of $\mathbf{x}_0$. Among those we consider this one:

$$L_{UQ}(\mathbf{X}_0, t_0, \tau, p) = \sum_{i=1}^{n} |x_i(t_o + \tau) - x_i^*|^p \,,\ p \leq 1,\ \mathbf{X}_0 \in \mathbb{R}^n, \tau > 0. \tag{6.3}$$

Here, $\mathbf{X}_0$ represents a set of initial conditions whose coordinates $(x_1, x_2, .., x_n)$, belong to a n dimensional system (6.1) and are in the neighbourhood of the observation $\mathbf{x}_0$. The coordinates of the target, towards which the system is assumed to evolve in a time interval τ, are $(x_1^*, x_2^*, .., x_n^*)$. Panel a) in Figure 6.1 illustrates the evolution from the set $\mathbf{X}_0$ (the pink blob) to $\mathbf{X}^*$ (the light blue blob). Panel b) displays L_{UQ} evaluated in the whole domain. This

representation expresses how much uncertainty would be associated with the system (6.2) beyond the neighborhood $\mathbf{X}_0$, assuming that initial observations start at different points of the representation domain and that they evolve towards the assumed observed target position at the red asterisk in $\tau = 3$. It is clear from the representation, that L_{UQ} presents a structure that consists of singular features aligned with the stable manifold of the hyperbolic fixed point present in the vector field, as discussed and proven in (García-Sánchez et al., 2022a).

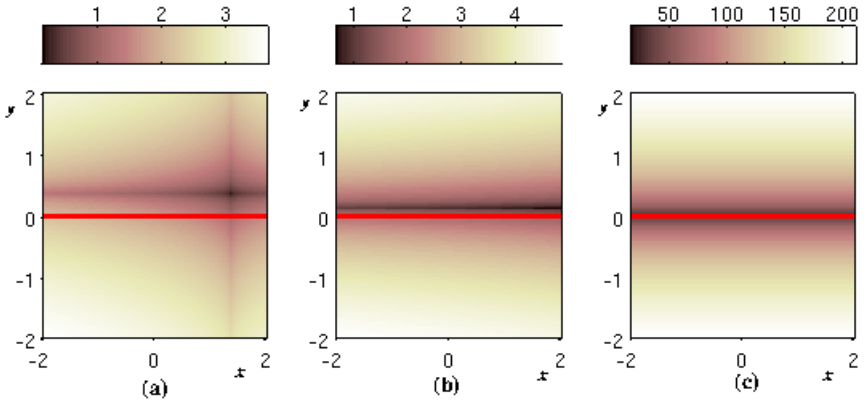

Figure 6.2 A representation in the plane of L_{BUQ} for the dynamical system (6.2) with target $x^* = (0.5, 1)$. a) $\tau = 1$; b) $\tau = 2$; c) $\tau = 15$. The red line represents the position of the unstable manifold.

In this chapter, our interest is in quantifying the uncertainty of a model for identifying a target source $\mathbf{x}^*$, which is consistent with a later observation $\mathbf{x}_1$ at time t_1. In this way, the target source, $\mathbf{x}^*$, is located at an earlier time $t^* = t_1 - \tau$. Similarly to the previous definition, for this setting, we propose the uncertainty to be:

$$L_{BUQ}(\mathbf{X}_1, t_1, \tau, p) = \sum_{i=1}^{n} |x_i(t_1 - \tau) - x_i^*|^p, \; p \leq 1, \; \mathbf{X}_0 \in \mathbb{R}^n, \tau > 0. \tag{6.4}$$

where now $\mathbf{X}_1$ represents a neighbourhood around the observation $\mathbf{x}_1 = (x_1, x_2, .., x_n)$ at time t_1 being n the dimension of the system (6.1), which in our specific examples is $n = 2$. The coordinates of the target are (x_1^*, x_2^*), and uncertainty is provided in terms of a distance metric between the target and the *backward* evolution of points near to $\mathbf{x}_1$ for a period τ.

Panel d) in Figure 6.1 illustrates the backward in time evolution of $\mathbf{X}_1$ (the pink blob) to $\mathbf{X}^*$ (the light blue blob) In the background, the panel also illustrates the vector field in a neighborhood of $\mathbf{x}_1$ at time t_1, and in the neighborhood of $\mathbf{x}^*$ at time t^*. Given that this vector field is stationary, its representation at an earlier time, $t^* = t_1 - \tau$, will be the same as at t_1, although in general this vector field is time-dependent and therefore its representation at t^* is different from that at t_1.

Panel e) displays in the whole domain, that is beyond the neighborhood $\mathbf{X}_1$, L_{BUQ} evaluated for $p = 0.5$, assuming $\tau = 3$. This representation expresses how much uncertainty is associated to the system (6.2), assuming that observations $\mathbf{x}_1$ could be anywhere in the domain and that they have evolved there from the target position $\mathbf{x}^*$ at $t^* = t_1 - \tau$. It is clear from the representation that L_{BUQ} presents a structure that consists of singular features aligned with the unstable manifold of the hyperbolic fixed point present in the vector field. A formal proof of this observation is given in the Section 6.2. In the proof it is shown how a sufficiently large τ is required for the singular structures obtained from Equation (6.4) to become aligned with the unstable manifolds. This is more clearly visualized in Figure 6.2. Panel a) shows the evaluation of L_{BUQ} for $\tau = 1$, where clearly the alignment with the unstable manifold is not yet achieved. Panels b) and c) confirm the convergence of the alignment towards the unstable manifold for, respectively, $\tau = 2$ and $\tau = 15$. This result completes the link between invariant dynamical structures and uncertainty quantification.

Panels c) and f) in Figure 6.1 graphically illustrate why the forward time uncertainty for system (6.2) is related to the stable manifold of the hyperbolic fixed point, while the backward time uncertainty is linked to the unstable manifold of that fixed point. Indeed, the forward time integration for initial conditions that stay on the stable manifold, for a sufficiently large τ, approach the fixed point at the origin, maintaining a fixed distance to the target, while all other initial conditions in the plane will increase their distance to the target for increasing τ. This is the origin of the singular features aligned with the stable manifold in forward time. Analogously, the backward time integration of initial conditions that stay on the unstable manifold, for a sufficiently large τ, approaches the fixed point at the origin, maintaining a fixed distance to the target. All other initial conditions in the plane will increase their distance to the target for increasing backward integration. This is the origin of the singular features aligned with the unstable manifold in backward time. Analogously this explanation also illustrates why both L_{UQ} and L_{BUQ} take minimum values along the unstable manifold. Indeed, they express the finite distance between the fixed point and the target, while the value of L_{UQ} and L_{BUQ} diverge for growing τ for all other points in the plane.

Figure 6.3 illustrates further these ideas. Panel a) represents the evolution versus τ of L_{UQ} at points: (0,2) in red – which is on the stable manifold– and (0,0) in black –the hyperbolic fixed point– as a function of τ, both with a target $\mathbf{x}^* = (1.5, 0.2)$ and $p = 0.5$. There is a transient behavior in τ for the point on the stable manifold, while in the limit of large τ both values converge to $|1.5|^{0.5} + |0.2|^{0.5} \sim 1.672$, which is the distance, in the defined metric, between the fixed point and the target. Similarly, panel b) represents the evolution of L_{BUQ} at points: (2, 0) in red –which is on the unstable manifold– and (0,0) in black –the hyperbolic

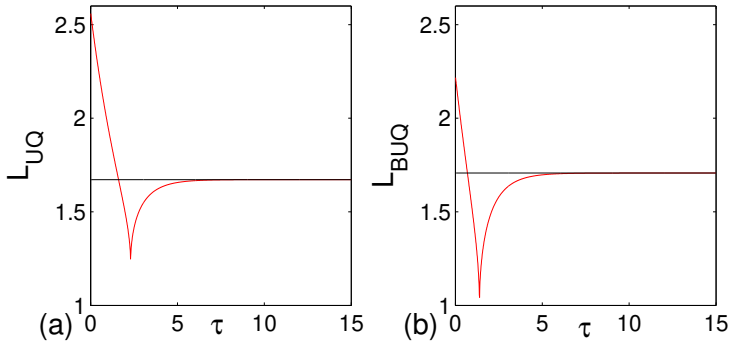

Figure 6.3 For the system given by Equation (6.2), a) evolution of L_{UQ} versus τ on the fixed point (black line) and on a point on the stable manifold (red line) with target $\mathbf{x}^* = (1.5, 0.2)$; b) evolution of L_{BUQ} versus τ on the fixed point (black line) and on a point on the unstable manifold (red line) with target $\mathbf{x}^* = (0.5, 1)$.

fixed point– as a function of τ, both with a target $\mathbf{x}^* = (0.5, 1)$ and $p = 0.5$. In the limit of large τ, both converge to the constant ~ 1.71.

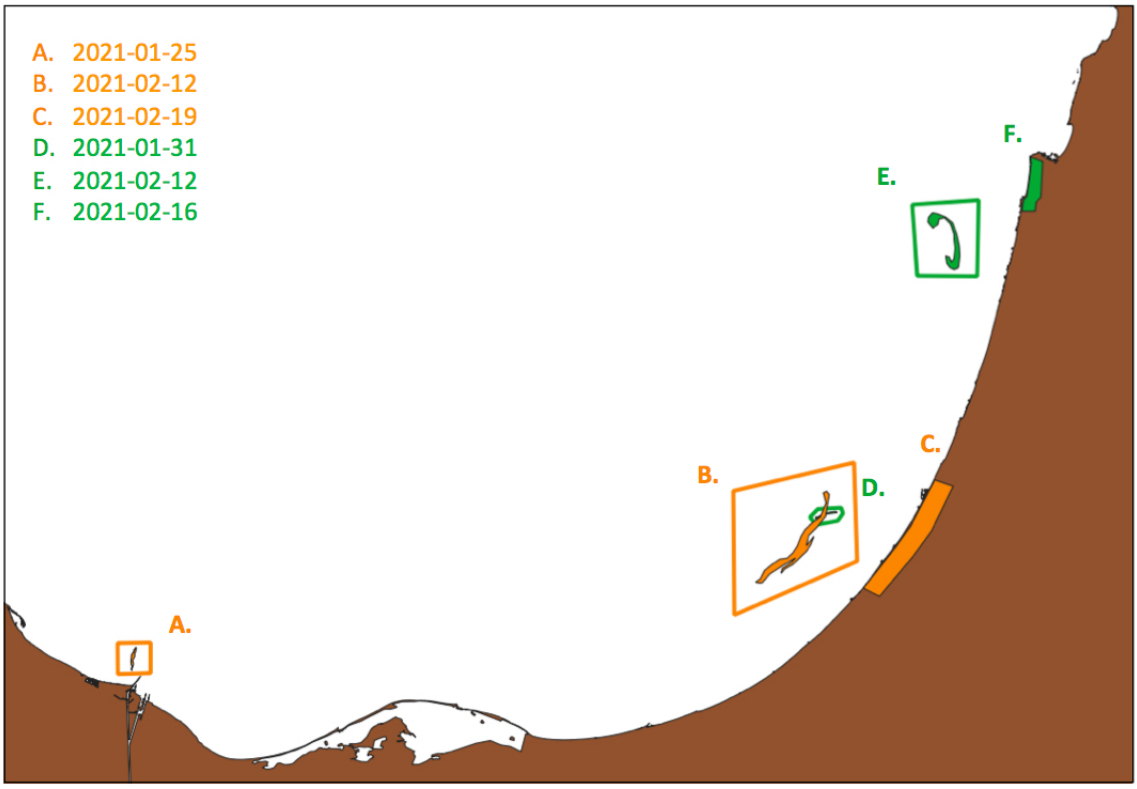

Figure 6.4 A graphical representation of the spills observed along the coastline of the Eastern Mediterranean and satellite observations matching the sources.

6.2. A proof for singularites in L_{BUQ}

Our proof follows the spirit of the work in Chapter 4 and by García-Garrido et al. (2018); Lopesino et al. (2015, 2017). We assume the definition of singular features given there, by considering that these are features of L_{BUQ} (we consider for simplicity the expression for L_{BUQ} given in Equation 6.4) on which the transversal derivative is not defined. We prove that, for the simple case of the linear saddle, the unstable manifold of the hyperbolic fixed point is aligned with singular features of L_{BUQ}.

We study the vector field of the autonomous saddle case, where the equations of motion are the following:

$$\begin{cases} \frac{dx}{dt} = \lambda x, \\ \frac{dy}{dt} = -\lambda y, \end{cases} \qquad \lambda > 0 \tag{6.5}$$

The system has a unique solution for a given condition (x_1, y_1) at time $t = t_1$:

$$\begin{cases} x(t) = x_1 e^{\lambda(t-t_1)} \\ y(t) = y_1 e^{-\lambda(t-t_1)}, \end{cases} \qquad \lambda > 0 \tag{6.6}$$

Notice that the origin $(0,0)$ is a hyperbolic fixed point with stable and unstable manifolds which are the following:

$$W^s(0,0) = \{(x,y) \in \mathbb{R}^2 \colon x = 0, y \neq 0\}, \tag{6.7}$$

$$W^u(0,0) = \{(x,y) \in \mathbb{R}^2 \colon x \neq 0, y = 0\}, \tag{6.8}$$

Since in this chapter we study the backwards uncertainty quantification method we will consider according to (6.4):

$$\begin{aligned} L_{BUQ}(\mathbf{X}_1, t_1, \tau, p) &= \sum_{i=1}^{n} |x_i(t_1 - \tau) - x_i^*|^p \\ &= |x_1 e^{\lambda \tilde{t}} - x^*|^p + |y_1 e^{-\lambda \tilde{t}} - y^*|^p \\ &= |x_1|^p |\omega - a|^p + |y_1|^p \omega^{-p} |1 - b\omega|^p \end{aligned} \tag{6.9}$$

where $\tilde{t} = t_1 - \tau - t_1 = -\tau < 0$, $a = \frac{x^*}{x_1}, b = \frac{y^*}{y_1}$ and $\omega = e^{\lambda \tilde{t}} = e^{-\lambda \tau}$, $p \leq 1$. In order to compute equation (6.9) we will calculate, for simplicity, each of the terms separately. In the first term we notice that the sign of the expression $(\omega - a)$, for $\tau \gg 1$, will be positive when $a < 0$ and could be negative when $a > 0$.

- For $a < 0$:

$$|\omega - a|^p = (\omega - a)^p \tag{6.10}$$
$$= (-a)^p + p\omega(-a)^{p-1} + \frac{1}{2}(p-1)p\omega^2(-a)^{p-2} \tag{6.11}$$
$$+ \frac{1}{6}(p-2)(p-1)p\omega^3(-a)^{p-3} + O\left(\omega^4\right) \tag{6.12}$$
$$= (-a)^p + O\left(e^{-\lambda\tau}\right), e^{-\lambda\tau} \ll 1 \tag{6.13}$$

- For $a > 0$ let be t_L such that for $\tau > t_L$, we get that $(\omega - a) < 0$:

$$|\omega - a|^p = (-\omega + a)^p = a^p + p\omega a^{p-1} + \frac{1}{2}(p-1)p\omega^2 a^{p-2} + \tag{6.14}$$
$$\frac{1}{6}(p-2)(p-1)p\omega^3 a^{p-3} + O\left(\omega^4\right) \tag{6.15}$$
$$= a^p + O(\omega) \tag{6.16}$$

Therefore

$$|\omega - a|^p = |a|^p + O\left(e^{-\lambda\tau}\right), \omega \ll 1. \tag{6.17}$$

Note that $a = x^*/x_1$. Thus

$$|x_1|^p|\omega - a|^p = |x_1|^p|e^{-\lambda\tau} - a|^p = |x^*|^p + O\left(|x_1|^p e^{-\lambda\tau}\right), e^{-\lambda\tau} \ll 1.$$

For the factor $|1 - b\omega|^p$ of the second term there exists a t_L such that if $\tau > t_L$, then $b\omega << 1$ and $(1 - b\omega) > 0$. This is always the case for $b < 0$ and is a plausible assumption for $b > 0$, if $b << \omega^{-1}$. We recall that $b = y^*/y_1$ and that therefore such t_L exists if $y_1 \neq 0$. In this case positiveness is guaranteed for sufficiently large τ, i.e, a Taylor series around $\omega = 0$, attained if $\tau \gg 1$ and $\tau > t_L$, is performed for the binomial:

$$(1 - b\omega)^p = 1 - bp\omega + \frac{1}{2}b^2(p-1)p\omega^2 - \frac{1}{6}\omega^3\left(b^3(p-2)(p-1)p\right) + O\left(\omega^4\right).$$

Therefore,

$$\frac{1}{\omega^p}(1 - b\omega)^p = \omega^{-p} - bp\omega^{(1-p)} + \frac{1}{2}b^2(p-1)p\omega^{(2-p)} - O\left(\omega^{(3-p)}\right).$$

Finally we get:

$$|y_1|^p\omega^{-p}|1-b\omega|^p = |y_1|^p|\omega^{-p}-b|^p \tag{6.18}$$
$$= |y_1|^p|e^{\lambda\tau p}-b|^p \tag{6.19}$$
$$= |y_1|^p e^{\lambda\tau p} + O\left(|y_1|^p be^{-\lambda\tau(1-p)}\right) \tag{6.20}$$

Thus, we can approximate L_{BUQ} as

$$L_{BUQ}(\mathbf{X}_1,t_1,\tau,p) \approx |x^*|^p + |y_1 e^{\lambda\tau}|^p = |x^*|^p + |y_1|^p e^{\lambda\tau p} \tag{6.21}$$

the dominant term is the term $|y_1|^p e^{\lambda\tau p}$. Therefore the unstable manifold at $y=0$, for 'sufficiently large' τ, is aligned with a singular feature of L_{BUQ}, as long as $y_1 \neq 0$, and for any $|y_1| > 0$ for a sufficient large τ satisfying, $\tau > t_L$.

6.3. Results

The backward-time uncertainty definition provided in Equation (6.4), or its analog for the Euclidean distance given by:

$$L_{BUQ}(\mathbf{X}_1,t_1,\tau) = \left[\sum_{i=1}^{n} |x_i(t_1-\tau)-x_i^*|^2\right]^{\frac{1}{2}},\ \mathbf{X}_1 \in \mathbb{R}^n, \tau > 0 \tag{6.22}$$

are very suitable for assessing the performance of ocean models for describing events where the source of a certain observable, for instance, a contaminant, is unknown. This section describes how to implement the use of the definitions given in (6.4) or (6.22) to assess and determine the model that better achieves the observations in a recent oil spill of this type. This event is of a different nature to those described in (García-Sánchez et al., 2021), where after a reported oil spill accident the interest was in describing and controlling its evolution in order to minimize its impact. In contrast, now we are interested in assessing models that provide information about when and where did the spill originate. Good models in the setting described in Figure 6.1d) are expected to have small distances between $\mathbf{X}^*$ (the blue domain) and $\mathbf{x}^*$ (the target) and we will exploit this idea to measure the quality of available ocean data sets.

We describe next the specific event to be considered under this perspective. At the beginning of 2021, the coastline of several Middle Eastern countries in the Eastern Mediterranean

was affected by the presence of oil from an unknown source(s) (Wikimedia Foundation, 2021). No accidents were reported for these spills previous to their arrival at the coast, and therefore there was no hint of their origin. Israeli authorities estimated that more than 1000 tons of tar (Z. Rinat and A. Ben Zikri, 2021) landed along 180 km of the Israeli and Lebanese shoreline (Kaplan-Zantopp, 2021; News Agencies, 2021; Polidura, 2021; Rutgers Staff, 2021; T. Joffre and R. Tercatin , 2021; Tercatin, 2021) in mid-February. They combined the use of satellite images with simulations by Garcia-Sánchez et al. (García-Sánchez et al., 2022b), which provided possible sources for this spill. Their work studied this event both from the remote sensing and modeling perspectives. Figure 6.4 illustrates some affected geographical areas. In this figure, orange and green colors along the coastline mark the oil arrivals. The systematic search of satellite images identified potential sources of these observations and a careful examination concluded that those sources surrounded by green and orange polygons, which correspond to satellite observations, were located in position and time in a manner consistent with the position and dates of the oil that subsequently arrived at the coast. According to (García-Sánchez et al., 2022b), orange polygons labeled as A and B, are successive earlier locations to the orange arrival labeled as C. Analogously green polygons labeled as D and E, correspond to the green arrival labeled as F. The successive dates for each observation are given in the figure.

Simulations in (García-Sánchez et al., 2022b) demonstrated that the spill was closely following fluid parcel trajectories $\mathbf{x}(t)$ that obeyed the equation:

$$\begin{cases} \dfrac{d\lambda}{dt} = \dfrac{u(\lambda,\phi,t)}{R\cos\phi} \\ \dfrac{d\phi}{dt} = \dfrac{v(\lambda,\phi,t)}{R} \end{cases} \tag{6.23}$$

where the position of the fluid parcel at the ocean surface is given in longitude (λ) and latitude (ϕ), and R is the Earth's radius. The system (6.23) is the particular form for our study of the general expression given by Equation (6.1), where $\mathbf{x} = (\lambda, \phi)$ and its right-hand side represent the two components of the vector field $\mathbf{v}$, which are determined by the zonal (u) and meridional (v) velocities. These velocity components are obtained as data sets from the Copernicus Marine Monitoring Environmental Service (CMEMS).

Equation (6.23) is a nonlinear non-autonomous dynamical system in 2D and it is required for implementing the backward evolution of fluid parcels in expression (6.22). L_{BUQ} in Equation (6.22) will have different evaluations for different CMEMS data sets. The goal of this section is to use these outputs to discriminate models. CMEMS provides two data sets describing currents in the Mediterranean Sea. One is the operational Mercator global ocean

analysis and forecast system that provides 10 days of 3D global ocean forecasts updated daily. This product includes daily and monthly mean fields of variables such as temperature, salinity, currents, sea level, mixed layer depth, and ice parameters from the top to the bottom of the global ocean. It also includes hourly mean surface fields for sea level height, temperature, and currents. The global ocean output files are displayed with a 1/12 degree horizontal resolution with an equirectangular longitude/latitude projection and 50 vertical levels ranging from 0 to 5500 meters.

The second data set is the physical component of the Mediterranean Forecasting System (Med-Currents), which is a coupled hydrodynamic-wave model, including tides, implemented over the whole Mediterranean Basin, with a higher resolution than the global model. Indeed, its horizontal grid resolution is 1/24 degree with 141 unevenly spaced vertical levels. The model solutions are corrected with a variational data assimilation scheme (3DVAR) of vertical profiles of temperature and salinity along the satellite track that provides observations of sea level anomalies (SLA).

Given that both models provide information for the same area, a natural question is to determine whether one is more suitable than the other for describing transport in the type of event described above. Models such as that given in Equation (6.23), possess a transport signature based on invariant manifolds associated with hyperbolic trajectories, which following Poincaré's idea, constitute geometrical structures on the ocean surface that organize particles schematically by regions corresponding to qualitatively different types of trajectories. These geometrical features allow a more robust analysis of the transport capacity of ocean currents than that based on individual trajectories. Indeed, there exist mathematical results that discuss the persistence of these geometrical structures in the presence of small perturbations, while individual trajectories may be affected much more drastically by perturbations (García-Garrido et al., 2018; Haller, 2002). In the past these features have been used to assess the transport performance of data sets (Garcia-Garrido et al., 2015; Haza et al., 2007, 2010; Kuznetsov et al., 2002; Mendoza et al., 2014; Shadden et al., 2009). In the context of geophysical flows, these geometrical structures are referred to as Lagrangian Coherent Structures (LCSs). The use of LCS allows a *qualitative* assessment of the performance of data sets, however, definitions such as that given in Equation (6.22) allow a *quantitative* analysis that we will implement next in the context of the oil spill event described in (García-Sánchez et al., 2022b).

In this work, we compute LCS using Lagrangian Descriptors (Mancho et al., 2013; Mendoza and Mancho, 2010), a method based on computing the function defined as:

$$M(\mathbf{x}_0, t_0, \tau) = \int_{t_0-\tau}^{t_0+\tau} ||\mathbf{v}(\mathbf{x}(\mathbf{x}_0, t), t)||\, dt, \tag{6.24}$$

where the Euclidean norm, $||.||$, of the vector field $\mathbf{v}$ is evaluated along fluid parcel trajectories $\mathbf{x}(\mathbf{x}_0,t)$ of Equation (6.23), and therefore the integral in Equation (6.24) evaluates the arclength of this trajectory on the latitude-longitude plane at the ocean surface. In expression (6.24), the forward integration from t_0 reveals by means of singular features the stable manifolds associated to hyperbolic trajectories, whereas the backward integration highlights their unstable manifolds. This is explicitly expressed by splitting the integral (6.24) into two terms as follows:

$$\begin{aligned} M(\mathbf{x}_0,t_0,\tau) &= \int_{t_0-\tau}^{t_0} \mathbf{v}(\mathbf{x}(\mathbf{x}_0,t),t)\,dt + \int_{t_0}^{t_0+\tau} \mathbf{v}(\mathbf{x}(\mathbf{x}_0,t),t)\,dt \\ &= M^{(b)}(\mathbf{x}_0,t_0,\tau) + M^{(f)}(\mathbf{x}_0,t_0,\tau) \end{aligned} \tag{6.25}$$

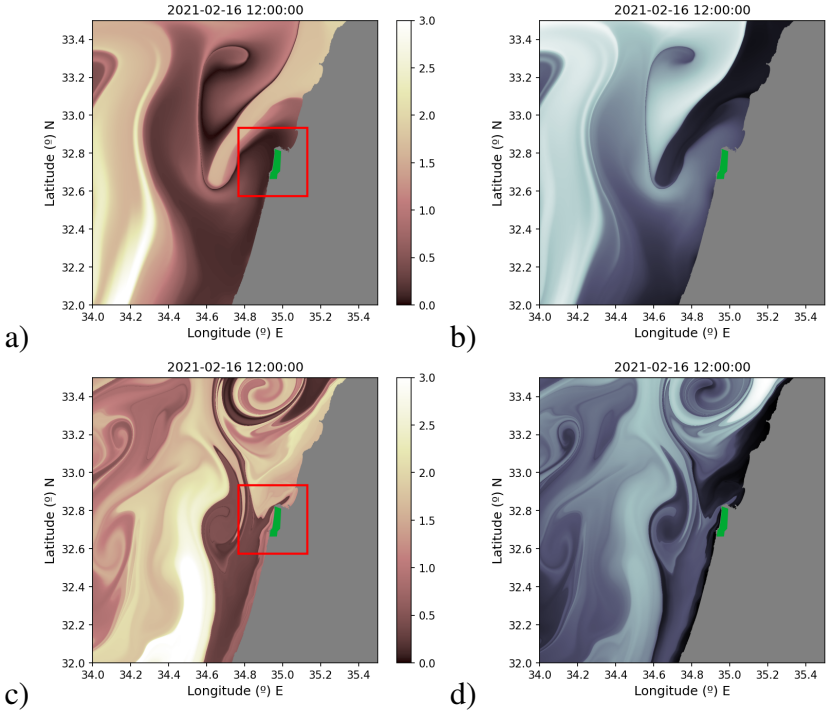

Figure 6.5 Evaluation on the 16th of February 2021 of L_{BUQ} using the target, $\mathbf{x}^* = (34.36°\text{E}, 31.78°\text{N})$ and of $M^{(b)}$ using $\tau = 16$ days; a) L_{BUQ} with the CMEMS global product; b) $M^{(b)}$ with the CMEMS global product; c) L_{BUQ} with the CMEMS Mediterranean product; d) $M^{(b)}$ with the CMEMS Mediterranean product.

We explore next the implementation of the ideas discussed in the previous section, to evaluate the performance of the two CMEMS products in the context of this environmental damage and their links to the unstable manifolds of hyperbolic trajectories present in the system Equation (6.23). Following oil detections displayed in Figure 6.4, we start the

discussion considering the first arrival to the coast on the 16th of February 2021, which is the green mark at the Israeli coast (F) and is considered to be the observation $\mathbf{x_1}$. For it, we consider that the position (D) on the 31st of January 2021 is its backward time target $\mathbf{x}^* = (34.355734°\text{E}, 31.777414°\text{N})$. Figure 6.5a) shows the evaluation of L_{BUQ} according to Equation (6.22) in a large area, considering that the eastward (u) and northward (v) velocity components are provided by the CMEMS global model. It is remarkable that its structure presents important analogies with the $M^{(b)}$, visible in panel b), which has been computed for $\tau = 16$ days. This image highlights, by means of singular features, the unstable manifolds of hyperbolic trajectories present in the vector field supplied by Equation (6.23). This result confirms that the uncertainty associated with the model has a structure closely related to invariant dynamical structures. The red square in panel a) highlights a neighborhood of the observation whose origin is conjectured to be at target $\mathbf{x}^*$. This domain $\mathbf{X_1}$ is used to characterize the performance of the model with respect to the hypothesis, assuming that the model is good if the target is consistent with arrivals in all this domain $\mathbf{X_1}$. The model is characterized through mean values of L_{BUQ} in this box. Panels c) and d) reproduce results for the CMEMS Mediterranean product. It is again clear the close relationship between the structure of L_{BUQ} and the unstable manifolds of hyperbolic trajectories present in Equation (6.23).

We continue the discussion considering that the observation $\mathbf{x_1}$ is the orange mark at the Gaza coast (C) on the 19th of February 2021. For it, we consider that the position (A) on the 25th of January 2021 is its backward time target: $\mathbf{x}^* = (32.319813°\text{E}, 31.350392°\text{N})$. Figure 6.6 displays the results both for CMEMS global and Mediterranean products. Panels a) and c) display the outputs of L_{BUQ}, and the red box highlights the neighborhood $\mathbf{X_1}$ used to characterize the performance of the model. Panels b) and d) again confirm the similarities between the unstable manifolds of hyperbolic trajectories in Equation (6.23) and the structure of L_{BUQ}.

It is remarkable that for both cases examined in figures 6.5 and 6.6, L_{BUQ} takes, in the neighborhood $\mathbf{X_1}$, considerably larger values for the CMEMS Mediterranean product than for the global one. Table 6.1 confirms this point by providing the averages in both domains in the column labeled as “Remote Targets", suggesting the better performance of the global model for these cases.

Figure 6.4 shows that related to the oil arrivals marked in green (F) and orange (C), there exist additional targets $\mathbf{x}^*$ nearer and closer to the observation $\mathbf{x_1}$, than those previously discussed. These backward-in-time targets, labeled (B) and (E), were identified from satellite imagery between the dates of the original sources and the dates of arrival on shore. These spills, after several days have elapsed since their leak, spread out on the ocean surface due

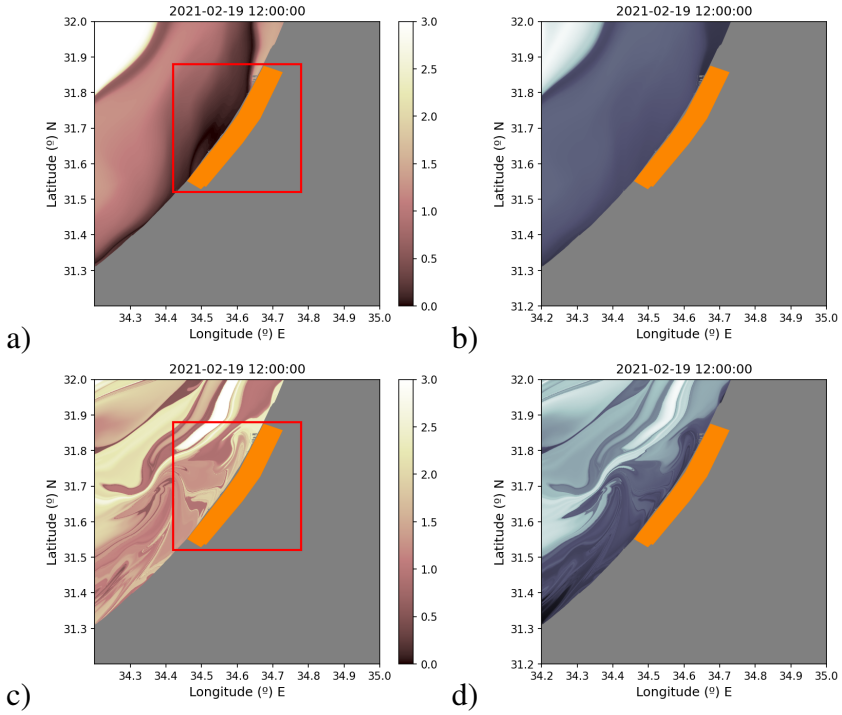

Figure 6.6 Evaluation on the 19th of February 2021 of L_{BUQ} using the target, $\mathbf{x}^* = (34.32°\text{E}, 31.35°\text{N})$ and of $M^{(b)}$ using $\tau = 25$ days; a) L_{BUQ} with the CMEMS global product; b) $M^{(b)}$ with the CMEMS global product; c) L_{BUQ} with the CMEMS Mediterranean product; d) M^b with the CMEMS Mediterranean product.

to the ocean movement, which stretches and folds them in a chaotic dynamic. Indeed, this description matches well the appearance of targets (B) and (E), as discussed in (García-Sánchez et al., 2022b). Now we consider the evaluation of L_{BUQ} using these new $\mathbf{x}^*$ to assess both models. We start considering the green observation (F) ($\mathbf{x_1}$) on the Israeli coast. For it, central coordinates of the spill contour on the 12th of February 2021 are $\mathbf{x}^* = (34.72008°\text{E}, 32.59311°\text{N})$. Other target positions within the extended spill could have been considered, but they do not lead to substantial changes either in the results or in the discussions. Panels a) and b) in Figure 6.7 display the evaluation L_{BUQ} for this target, considering the CMEMS global and Mediterranean products respectively. Regarding the orange observation (C) coordinates that correspond to its backward-in-time target on the 12th of February 2021 are $\mathbf{x}^* = (34.2891°\text{E}, 32.59311°\text{N})$. As before, given that this is a rather spread contour, other target positions could have been considered, but we do not discuss them as they provide no changes in the conclusions. For these assumptions panels c) and d) of Figure 6.7 display L_{BUQ} considering the CMEMS global and Mediterranean products respectively. In these pictures, the red box delimits the boundaries of the neighborhood $\mathbf{X_1}$

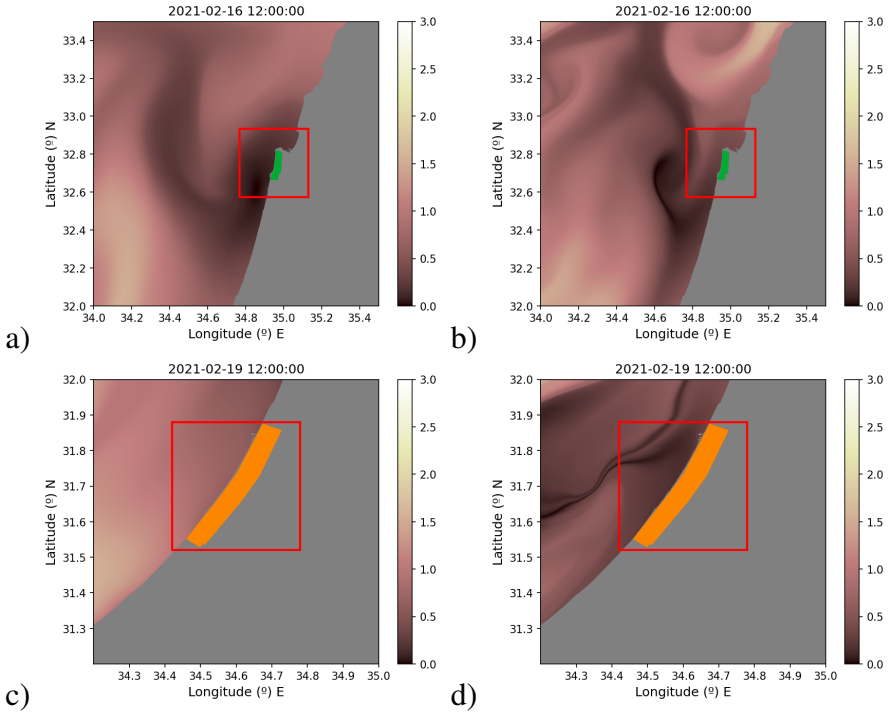

Figure 6.7 Evaluation L_{BUQ} on the Israel and Gaza coast for the close targets using the global and the Mediterranean data. L_{BUQ} on 16th of February 2021 using the target, $\mathbf{x}^* = (34.72°\text{E}, 32.59°\text{N})$; a) L_{BUQ} on the Israel coast with the CMEMS global product; b) $M^{(b)}$ on the Israel coast with the CMEMS Mediterranean product. L_{BUQ} on 19th of February 2021 using the target, $\mathbf{x}^* = (34.28°\text{E}, 32.59°\text{N})$; c) L_{BUQ} on the Gaza coast with the CMEMS Global product; d) $M^{(b)}$ on the Gaza coast with the CMEMS Mediterranean product.

used to evaluate the model performance. In this case the column “Close Targets" in Table 6.1 shows the results for both models.

A discussion of these results requires highlighting the sizes involved in the different settings. The distance between the remote targets and the Gaza (orange) and Israeli (green) shore impact points are, respectively, $\sim$ 215 km and 127 km. These size ranges involve ocean mesoscale structures, which seem to be better represented in the global model. The close targets are at distances $\sim$ 28 km and 33 km respectively of the Gaza and Israel arrival points (C) and (F). These sizes involve ocean submesoscale structures, which should be better represented by the higher resolution model, which is the CMEMS Mediterranean product. Indeed, this is the one that on average performs better for the closer targets, although the global model shows a good performance as well for the Israel case, despite its lower resolution.

	Remote Targets		Close Targets	
Case	Global	Mediterranean	Global	Mediterranean
Israel	0.2989	0.9434	0.1642	0.3375
Gaza	0.34074	1.5426	0.7810	0.24666

Table 6.1 Averages of L_{BUQ} within the $\mathbf{X_1}$ domains highlighted with red boxes.

6.4. Conclusions

This article proposes a new definition for uncertainty quantification that extends those recently proposed in oceanic contexts in (García-Sánchez et al., 2022b; García-Sánchez et al., 2021). The new definition is referred to as Lagrangian Uncertainty Quantification in Backward time (L_{BUQ}), and it is suited to measure if a given transport model consistently describes the source of an observation whose origin is unknown.

We have found that the defined quantity L_{BUQ}, when evaluated in the neighborhood of an observation with respect to its backward-in-time target, has a *structure* which has been linked to the unstable invariant manifolds of the hyperbolic trajectories present in the model vector field. This link has been rigorously proven in a simple example, and numerically verified in a real inspired case: the oil spill accident that affected the Eastern Mediterranean in 2021, which was studied in (García-Sánchez et al., 2022b).

The new definition, L_{BUQ}, has been exploited to quantify the performance of different CMEMS products to describe the sequence of events reported in (García-Sánchez et al., 2022b) regarding the oil spill accident in the Eastern Mediterranean in 2021. In this event, some of the backward-in-time targets are very far from the impact point, and their evolution involves mesoscale structures, which our analysis shows are better represented in the CMEMS global model. On the contrary for targets that are close, involving submesoscale structures, on average the CMEMS Mediterranean product performs better, although in some cases CMEMS global product also performs well.

Our results are set within a different framework compared to other inverse uncertainty studies. In those studies, the model typically consists of a dissipative partial differential equation with adjustable parameters, and the uncertainty analysis aims to determine the best-fitting parameters based on observations. However, in our framework, the model comprises a two-dimensional set of volume-preserving (non-dissipative) non-autonomous differential equations, and their exact form is unknown as they rely on approximated velocity fields. Many classical inverse problems, such as the inverse heat equation, are ill-posed, meaning that inferring a previous temperature distribution from final data is highly sensitive to changes in the final data. Although our framework differs from such cases, we still observe a high

sensitivity to the uncertainty measured around a final observation, as demonstrated in Figures 6.5, 6.6, 6.7. In the neighborhood surrounding the final observation, the uncertainty exhibits a complex structure with high oscillations, and we have established a connection with the unstable manifolds of hyperbolic trajectories. Thus, we illustrate how concepts from dynamical systems are linked to uncertainty quantification, whereas a statistical perspective has traditionally been the main focus in this context. Finally, we have shown how to implement these concepts for the practical purpose of discriminating the best data set performer on specific environmental applications.

Chapter 7

Dynamical Systems and Satellite Imagery for Hydrodynamic Models

This chapter is based on the results described in the paper by García-Sánchez et al. (2023b), which is a continuation of the IMPRESSIVE collaborative effort. For the sake of completeness and consistency, we will recall the methodological aspects described in Chapter 2.

Ocean numerical models help to understand and predict the ocean variables that have an impact on the environment, climate, and human activities. Oceanic data produced by models are increasingly becoming available, with various services providing valuable information on the ocean's physical state and dynamics. For instance, the Copernicus Marine Environment Monitoring Service (CMEMS) offers regular and systematic data on current and future variables, as well as retrospective data records (reanalysis) of the global and European regional seas. Alternatively, the HYbrid Coordinate Ocean Model (HYCOM), a multi-institutional effort sponsored by the National Ocean Partnership Program (NOPP) as part of the US Global Ocean Data Assimilation Experiment (GODAE), is dedicated to developing and evaluating data-assimilative hybrid coordinate ocean models. The products offered by these services typically have resolutions of the order of 2.5-8 km and have been successful in describing events above those scales (Garcia-Garrido et al., 2015; García-Garrido et al., 2016; García-Sánchez et al., 2022b). More recently, it has been pointed out (García-Sánchez et al., 2021) the necessity of using products with much higher resolution to address management needs at the coastal level. These needs may include navigation, harmful algae blooms, effluent dispersion, search and rescue operations, oil spill response, etc. In these cases, models are particularly valuable for understanding and predicting ocean currents for the management of aspects that affect life in these areas, including beach conditions and near-shore environments.

In situ measurements are incorporated into ocean models through different methodologies to achieve outputs that are accurate and consistent with the real ocean state. Among the instruments employed for in situ measurements are moored current meters, drifters, shipboard current profilers that measure sea surface velocity, etc. The deployment and maintenance of this equipment is expensive and, in general, its spatial coverage is limited to hotspot areas where the investment in these measurements is worth it. There exist however wide coastal and marine protected areas, where high-resolution models can be very valuable for management purposes, but for which in situ measurements are not available and therefore their validation is challenging. However, observations in these areas are possible through satellites that today are equipped with multiple remote sensing systems capable of providing valuable information on the dynamic properties of extensive oceanic coastal areas. In this work, we will explore the use of methodologies based on dynamical systems and satellite imagery for feedback and adjustment of ocean model outputs and as a validation method.

More specifically, this chapter starts with the creation of a very high-resolution hydrodynamic model in an area for which no in situ measurements were available. This is the area of the Rafina port in Greece, which was taken as a study case in the framework of the IMPRESSIVE project. Sentinel 2 and Sentinel 3 images near the coast provide images in the optical band that after being processed are able to identify turbidity caused by suspended particles, including particulate and dissolved organic and inorganic matter. These materials may derive from sources such as primary production blooms and wastewater. The spread of these compounds makes visible convoluted shapes, which are linked to invariant dynamical objects, called Lagrangian Coherent Structures (LCS), obtained from the currents. Thus, patterns visible in remote sensing images can be correlated to patterns obtained from the hydrodynamic model. We will utilize this idea to explore an effective methodology for validating the transport capacity of the model outputs. This approach differs from classical validations that compare in situ measurements of currents, sea level, etc. with those obtained from the models. Our comparison is systematically implemented by adjusting the parameters and parameterizations required by the model, which include closure relationships for unresolved turbulent scales, lateral boundary conditions for the nested model, and the coupling of surface ocean motion with atmospheric winds, among others. In addition, an index is defined to quantify the degree of fitting of each parameter set to the satellite observations.

The manuscript is structured as follows. Section 7.1 provides a description of the equations and software utilized to set up the hydrodynamical model for the Rafina Port. It also discusses the boundary conditions and settings specific to the temporal window of October-December 2019. In Section 7.2, the available remote sensing products for that temporal window are described. Section 7.3 delves into the dynamical systems concepts

used to establish the connection between the hydrodynamical model outputs and the satellite imagery. Section 7.4 outlines the various settings for the experiments conducted and details the procedure used to quantify their performance. The results are presented in Section 7.5, and finally, the conclusions are explained in Section 7.6.

7.1. The hydrodynamic model

7.1.1. The oceanic regional model

To set up the hydrodynamic model we have used the Regional Oceanic Modeling System (ROMS). ROMS is a member of a general class of numerical models that solve the unsteady Reynolds-averaged Navier–Stokes equations under the hydrostatic and Boussinesq assumptions (Haidvogel et al., 2000; Shchepetkin and McWilliams, 2005). The Reynolds-averaged Navier-Stokes (RANS) equations are derived from the Navier-Stokes equations by applying Reynolds decomposition, which decomposes the instantaneous velocity field ($\mathbf{v}_T$) into a time-averaged ($\overline{\mathbf{v}}_T$) and a fluctuating component ($\mathbf{v}'_T$). In this work, the mean velocity is the velocity field solved in equations (7.1)-(7.3), which is referred to as $\mathbf{v} = (u, v, w)$ there. The fluctuating component $\mathbf{v}'_T = (u', v', w')$ is solved using turbulent closure relations. ROMS has been employed in numerous operational oceanography systems on regional scales. Examples include the NOAA operational forecast systems for locations such as Tampa Bay, Chesapeake Bay, and the Gulf of Maine, and the SAMOA system, which the Spanish Public State Port Agency developed to offer tailored operational meteorological and oceanographic data (Sotillo et al., 2020). ROMS has also been utilized in diverse applications like estuarine modeling (Cerralbo et al., 2015), sediment transport (Grifoll et al., 2014), oceanic basin modeling (Malanotte-Rizzoli et al., 2000), climate research (Di Lorenzo et al., 2008), and the study of atmosphere-wave-current interactions (Warner et al., 2010). A key advantage of ROMS is its modular structure and efficient parallelization using the Message Passing Interface (MPI), enabling rapid computational performance (Wang et al., 2005).

ROMS solves the governing dynamical equations in flux form. The vertical take terrain-following coordinates that are named sigma vertical coordinates. We have used Cartesian coordinates in the horizontal, although other choices are available. These equations take the form (Haidvogel et al., 2008):

$$\frac{\partial u}{\partial t} + \mathbf{v} \cdot \nabla u - fv = -\frac{\partial \phi}{\partial x} - \frac{\partial}{\partial z}\left(\overline{u'w'} - \nu \frac{\partial u}{\partial z}\right) + \mathscr{F}_u + \mathscr{D}_u, \tag{7.1}$$

Parameters	p	m	n	σ_k	σ_ψ	c_μ^0	c_1	c_2	c_3^+	c_3^-	$k_{\min}$	$\psi_{\min}$	F_{wall}	c	ν	ν_θ
Values for $k-\varepsilon$ model	3	1.5	-1	1.0	1.3	0.5544	1.44	1.92	1.0	-0.518	$7.6\cdot10^{-6}$	$1.0\cdot10^{-12}$	1.0	1	$5.0\cdot10^{-6}$	$5.0\cdot10^{-6}$

Table 7.1 Parameters for the generic length scale turbulence- $k-\varepsilon$ model and Kantha-Clayson stability functions (see (Warner et al., 2005)).

$$\frac{\partial v}{\partial t}+\mathbf{v}\cdot\nabla v+fu=-\frac{\partial \phi}{\partial y}-\frac{\partial}{\partial z}\left(\overline{v'w'}-\nu\frac{\partial v}{\partial z}\right)+\mathscr{F}_v+\mathscr{D}_v, \tag{7.2}$$

In the Boussinesq approximation, changes in density are disregarded in the momentum equations, except for their influence on the buoyancy force within the vertical momentum equation. When the hydrostatic approximation is employed, it is additionally presumed that the buoyancy force is counterbalanced by the vertical pressure gradient:

$$\frac{\partial \phi}{\partial z}=-\frac{\rho g}{\rho_0} \tag{7.3}$$

where $\phi = p/\rho_0$ and $p \approx -\rho_0 g z$ is the total pressure. The continuity equation for an incompressible fluid:

$$\frac{\partial u}{\partial x}+\frac{\partial v}{\partial y}+\frac{\partial \omega}{\partial z}=0 \tag{7.4}$$

Here $\mathbf{v}=(u,v,\omega)$ and u, v, and ω are the components of velocity in the horizontal (x and y) and vertical (scaled sigma coordinate, s) directions respectively; and f is the Coriolis parameter. An over-bar represents a time average, and a prime ($'$) represents turbulent fluctuations. ρ and ρ_0 are total and reference densities; g is the acceleration due to gravity; ν is the molecular viscosity. Here all $\mathscr{F}$ are forcing terms and $\mathscr{D}$ are horizontal diffusive terms.

Temperature (T) and salinity (S) scalar tracers, generically denoted as C, are coupled to the momentum equations, and their transport equation is given by:

$$\frac{\partial C}{\partial t}+\mathbf{v}\cdot\nabla C=-\frac{\partial}{\partial z}\left(\overline{c'w'}-\nu_\theta\frac{\partial C}{\partial z}\right)+C_{\text{source}}+\mathscr{F}_C+\mathscr{D}_C \tag{7.5}$$

Here C_{source} represents scalar source/sink terms; ν_θ is the molecular diffusivity. Again $\mathscr{F}$ are forcing terms and $\mathscr{D}$ are horizontal diffusive terms. A function $\rho=\rho(T,S,p)$ is required to specify the equation of state. We have selected the option of the nonlinear equation of state introduced by Jackett and Mcdougall (1995).

Equations (7.1)-(7.2) and (7.5) are closed by parameterizing the Reynolds stresses and turbulent tracer fluxes as:

$$\overline{u'w'}=-K_M\frac{\partial u}{\partial z};\quad \overline{v'w'}=-K_M\frac{\partial v}{\partial z};\quad \overline{c'w'}=-K_H\frac{\partial \rho}{\partial z} \tag{7.6}$$

with

$$K_M = c\sqrt{2k}lS_M + \nu \qquad K_H = c\sqrt{2k}lS_H + \nu_\theta \tag{7.7}$$

In these equations, K_M represents the eddy viscosity for momentum and K_H represents the eddy diffusivity for tracers. S_M and S_H are stability functions that describe the effects of shear and stratification. From the several possibilities available in ROMS, we have chosen the Kantha-Clayson stability functions (see (Warner et al., 2005)). The replacement of Eqs. (7.6) into Eqs.(7.1)-(7.2) and (7.5) leads to the standard harmonic form for vertical viscous/diffusive terms. The turbulent quantities k (turbulence kinetic energy) and l (turbulent length scale) must be determined in order to close the set of equations. ROMS contains a variety of methods to do this. In this work, we considered the generic lengthscale (GLS), proposed by Umlauf and Burchard (2003) and implemented in ROMS by Warner et al. (2005). This is a generic two-equation turbulence closure scheme. The first equation represents the conventional transport equation for the turbulent kinetic energy (k),

$$\frac{\partial k}{\partial t} + \mathbf{v}\cdot\nabla k = \frac{\partial}{\partial z}\left(\frac{K_M}{\sigma_k}\frac{\partial k}{\partial z}\right) + P + B - \varepsilon, \tag{7.8}$$

where σ_k is the turbulence Schmidt number for k. P and B represent production sources by shear and buoyancy, and ε is the dissipation. They are given by:

$$P = K_M\left[\left(\frac{\partial u}{\partial z}\right)^2 + \left(\frac{\partial v}{\partial z}\right)^2\right],\ B = K_H\left(\frac{g}{\rho_0}\frac{\partial \rho}{\partial z}\right),\ \varepsilon = (c_\mu^0)^{3+p/n}k^{3/2+m/n}\psi^{-1/n}, \tag{7.9}$$

here the stability coefficient c_μ^0 is determined based on experimental data for the unstratified channel flow with a log-layer solution. The second equation of the GLS model describes the evolution of ψ, a generic parameter used to establish the turbulence length scale:

$$\frac{\partial \psi}{\partial t} + \mathbf{v}\cdot\nabla\psi = \frac{\partial}{\partial z}\left(\frac{K_M}{\sigma_\psi}\frac{\partial \psi}{\partial z}\right) + \frac{\psi}{k}(c_1 P + c_3 B - c_2\varepsilon F_{\text{wall}}), \tag{7.10}$$

The parameter σ_ψ represents the turbulence Schmidt number for ψ, indicating the ratio of momentum diffusivity to the diffusivity of ψ. Coefficients c_1 and c_2 are chosen to be consistent with experimental observations of decaying homogeneous, isotropic turbulence (Wilcox et al., 1998). The parameter c_3 assumes different values for stable (c_3^+) or unstable (c_3^-) stratification. Also,

$$\psi = (c_\mu^0)^p k^m l^n. \tag{7.11}$$

The parameters in expressions (11)-(13) for the $k-\varepsilon$ model, which is considered in our simulations, take values summarized in Table 7.1 (see (Warner et al., 2005)).

We further explain the sigma vertical coordinates used in ROMS. The variables related to this coordinate are ζ, representing the wave-averaged free-surface elevation, and h, denoting the depth of the sea floor relative to the mean sea level. In a topography-following vertical coordinate system, there is a transformation,

$$z = z(x, y, \sigma), \tag{7.12}$$

where z is the Cartesian height and σ is the vertical distance from the surface measured as the fraction of the local water column thickness; i.e, $-1 \leq \sigma \leq 0$, where $\sigma = 0$ correspond to the free surface, $z = \zeta$, and $\sigma = -1$ corresponds to the oceanic bottom or bathymetry, $z = h(x, y)$. In the case of the classical σ-coordinate, (7.12) reduces to

$$z = \sigma \cdot h(x, y) \tag{7.13}$$

This may be combined with nonlinear stretching, $S(\sigma)$,

$$z(x, y, \sigma) = S(\sigma) \cdot h(x, y). \tag{7.14}$$

ROMS allows to use a general vertical coordinate system *S*-coordinate (Song and Haidvogel, 1994):

$$z(x, y, \sigma) = \zeta(x, y, t) + [\zeta(x, y, t) + h(x, y)]\, S(x, y, \sigma) \tag{7.15}$$

$$S(x, y, \sigma) = \frac{h_c \sigma + h(x, y) C(\sigma)}{h_c + h(x, y)} \tag{7.16}$$

where $h_c \leq h_{min}$ is a free parameter that must be adjusted for each application. h_c is a depth above which the vertical grid spacing of the sigma layers becomes (a) nearly uniform and (b) nearly independent of local depth, h, as long as $h \gg h_c$. In our case h_c = 84 m and $C(\sigma)$ can take different forms. In our application, we are assuming that

$$S(x, y, \sigma) = \begin{cases} 0 & \text{if } \sigma = 0,\ C(\sigma) = 0, \text{ at the free-surface,} \\ -1 & \text{if } \sigma = -1,\ C(\sigma) = -1, \text{ at the ocean-bottom,} \end{cases} \tag{7.17}$$

and $C(\sigma)$ is defined as a continuous, double-stretching function controlled at the surface by θ_s and at the bottom layer by θ_b. In our particular case, we have selected $\theta_S = 5$ and $\theta_B = 0.4$. The refinement function is then defined in two steps. First, we consider for the surface:

$$C_s(\sigma) = \frac{1 - \cosh(\theta_S \sigma)}{\cosh(\theta_S) - 1}, \quad \text{for } \theta_S > 1 \tag{7.18}$$

Then we consider the bottom refinement function:

$$C(\sigma) = \frac{\exp(\theta_B C_s(\sigma)) - 1}{1 - \exp(-\theta_B)}, \quad \text{for } \theta_B > 0. \tag{7.19}$$

7.1.2. The geographical domain

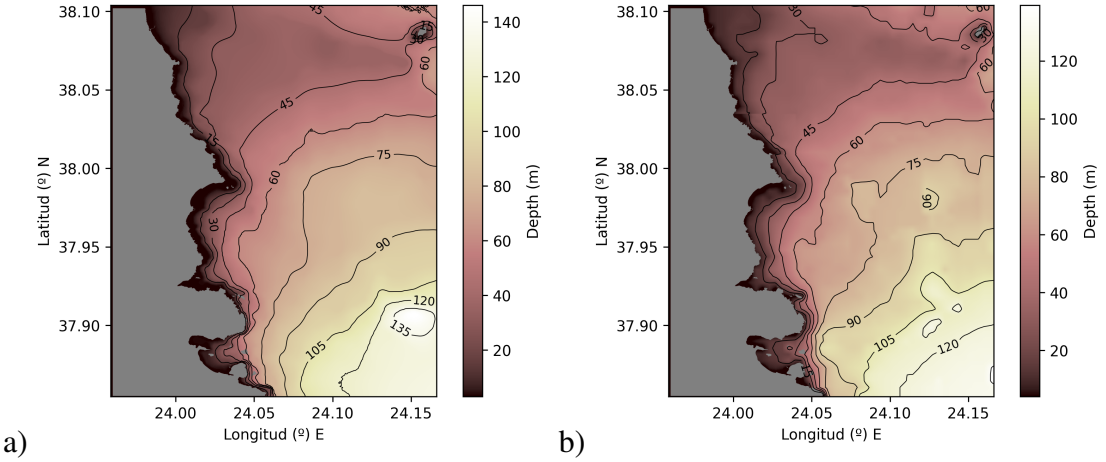

Figure 7.1 Bathymetry of the Rafina area in the domain L_0. The color intensity corresponds to the depth of the sea floor, with brighter colors indicating greater depths. a) NAVIONICS source data; b) GEBCO source data.

Our study sets up a hydrodynamic model in the neighborhood of Rafina Port. The area lies on the Aegean Sea coast, east of the Penteli mountains and northeast of the Mesogaia plain. It is 5 km (3 mi) north of Artemida, 7 km (4 mi) south of Nea Makri, and 25 km (16 mi) east of Athens city center. Specifically, the selected domain L_0 is between latitudes 37.8541-38.1042 degrees North and longitudes 23.9583-24.1667 degrees East.

Figure 7.1 illustrates the domain where equations are solved with two different choices for the function $h(x,y)$ representing the sea bed. Panel a) shows a bathymetry in the area obtained from contour levels that follow a NAVIONICS chart, which we have computed with a resolution of up to 10×10 meters. Panel b) displays the sea floor offered by GEBCO. This is a publicly-available bathymetry of the world's oceans. It operates under the joint auspices of the International Hydrographic Organization (IHO) and the Intergovernmental Oceanographic Commission (IOC) (of UNESCO). Its resolution is about 15 arc seconds. Sigma-coordinates employed by ROMS require that topographic steepness is limited to prevent pressure gradient errors. For this reason, topographies in Figure 7.1 are smoothed by selectively applying a local filter to reduce the r-factor below 0.2. The r-factor is a measure of the sharpness of the variations in the bathymetry. It is defined as the ratio of the maximum

height difference between adjacent points (Δh) to the average height of those points ($2h$); see, for example, (D. B. Haidvogel and A. Beckmann , 1999). Additionally, all depths in L_0 shallower than 0.5 m are reset to 0.5 m.

Although the appearance of both bathymetries is very similar we will explore their influence on the model outputs in section 7.5. Indeed, the sea floor has a number of impacts on ocean circulation. It helps steer large-scale circulation, and small gaps in the ocean floor can even influence the direction of dominant currents. In addition, small-scale bathymetric features can also affect ocean circulation. When ocean currents flow over the rough sea floor, energy is converted from horizontal flow into vertically propagating waves, leading to increased vertical mixing over rough topography (Gille and Smith, 2003).

7.1.3. Discretization and numerical algorithms

Regarding the spatial resolution implemented in the domain of interest, we have adopted a horizontal resolution of $80\times$ 80 meters, which is achieved with the grid of dimensions $Lm \times Mm$ reported in Table 7.2. The horizontal discretization implemented by ROMS is on an Arakawa 'C' grid and spatial derivatives are computed with a centered, second-order finite difference approximation.

Discretization of the vertical coordinate introduces a set of coordinate surfaces,

$$\{z_{k+\frac{1}{2}} = z_{k+\frac{1}{2}}(x,y), k = 0,1,\cdots N\} \tag{7.20}$$

In particular, for our application we have considered $N = 10$, that is 10 sigma levels. Figure 7.2 illustrates the $\sigma-$levels used at longitude 24.15 °E.

The stability of numerical models are affected by the numerical time-integration method, the spatial discretization, and the permitted modes in the equations. Advection is characterized by a velocity scale, U. The shortest advective timescale in a numerical model is Δ/U, where Δ is the spatial grid scale and U is a measure of the maximum characteristic velocity. The CFL number is the ratio of this characteristic timescale to the model time step:

$$CFL = \frac{U\Delta t}{\Delta}. \tag{7.21}$$

In the case of ROMS' time scheme, CFL must be less than a number on the order of unity. Then, the largest time step that can support numerical stability for a given flow and grid spacing scales is

$$\Delta t^u_{\max} \propto \frac{\Delta}{U}. \tag{7.22}$$

As we said before, $\Delta = 80$ meters so we consider $\Delta t = 10$ seconds.

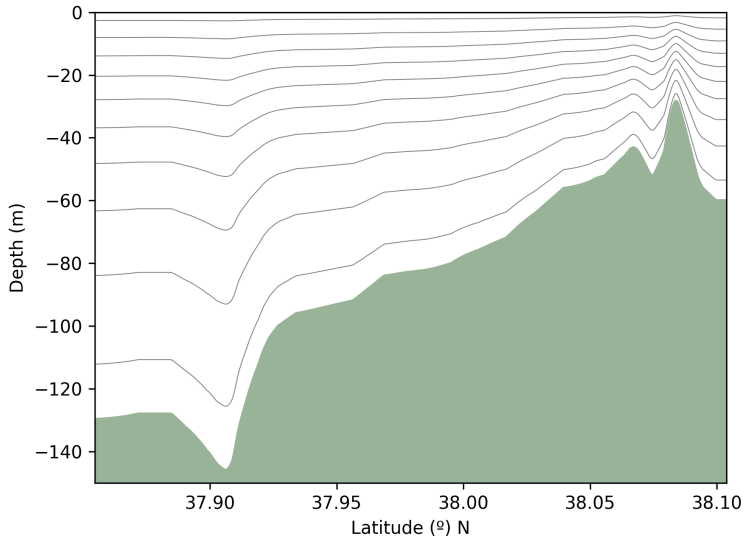

Figure 7.2 Vertical discretization at longitude 24.15 °E. The green color represents the bathymetry, while the lines indicate the different $\sigma-$levels based on the stretching function utilized.

The horizontal viscous and diffusivity terms $\mathscr{D}$ are given by the harmonic expressions:

$$\mathscr{D}_X = A_X \nabla^2 X, \quad \text{for } X = \{u, v, T, S\}, \tag{7.23}$$

where $A_{u,v}$ is the horizontal viscosity coefficient for u, v and A_T and A_S are the horizontal diffusivity coefficients for T, S. In our application, we will explore optimal settings of A_X for $X = \{u, v, T, S\}$ according to values given in Table 7.4.

ROMS uses a computational kernel that combines temporal averaging of the barotropic mode with modified pressure-gradient terms to accurately resolve barotropic processes and reduce errors in the density field, while maintaining the efficiency of the split-explicit formulation. In this process, two time steps are used to advance 3D momentum and tracer variables in the numerical model to effectively capture the complex interactions between the barotropic and baroclinic modes in the ocean. The first time step (Δ_t) is used to compute the right side of the 3D momentum equations, while the second time step (Δ_{tt}) is used for updating the barotropic mode. Vertical interpolation is carried out using either fourth-order centered schemes or conservative parabolic splines. The combination of moderate-order spatial approximations, quasi-monotone advection operators, and enhanced conservation properties leads to more robust, accurate, and less diffusive solutions than those produced by earlier terrain-following ocean models (Haidvogel et al., 2008). More details on the numerical

methods used in ROMS can be found in the literature (Shchepetkin and Mcwilliams, 1998; Shchepetkin and McWilliams, 2003, 2005).

7.1.4. Boundary Conditions

The ocean near coastlines experiences dynamic interactions at various scales. Coastal currents are influenced by local wind forcing, tides, and remote factors transmitted offshore and along the coastal waveguide. Offshore currents may be generated as part of the large-scale circulation or emerge from near-shore regions. However, it is impractical to accurately resolve all types of currents. Instead, regional models can be used to calculate local currents under the influence of local forcing and the larger-scale circulation, given a suitable prescription for lateral boundary forcing (Marchesiello et al., 2001). We detail next how boundary conditions are chosen in order to implement an appropriate downscaled high-resolution model.

Bottom boundary layer (BBL)

The dynamics of the Bottom Boundary Layer (BBL) affect the stress on the flow exerted by the bottom, which is incorporated into the Reynolds-averaged Navier–Stokes equations as boundary conditions for momentum. ROMS can use either of two sub-models to represent BBL processes: (i) simple drag-coefficient expressions, or (ii) more complex formulations that consider the interactions of waves and currents over a moveable bed. In our application, we use the former.

$$K_M \frac{\partial u}{\partial z} = \tau_b^x(x,y,t); \quad K_M \frac{\partial v}{\partial z} = \tau_b^y(x,y,t); \quad K_H \frac{\partial T}{\partial z} = 0; \quad K_H \frac{\partial S}{\partial z} = 0 \tag{7.24}$$

The drag-coefficient methods implement formulae for linear bottom friction, quadratic bottom friction, or a logarithmic profile. For our application, we have considered the quadratic bottom friction:

$$\tau_b^x(x,y,t) = C_d^b \cdot u\sqrt{u^2+v^2}; \quad \tau_b^y(x,y,t) = C_d^b \cdot v\sqrt{u^2+v^2} \tag{7.25}$$

$$\tau_b^x(x,y,t) = C_d^b \cdot (u-u_b)\|\mathbf{u}-\mathbf{u}_b\|, \quad \tau_b^y(x,y,t) = C_d^s \cdot (v-v_b)\|\mathbf{u}-\mathbf{u}_b\|, \tag{7.26}$$

where u_b, v_b refers to the eastward and northward bottom speed components and $\mathbf{u} = (u,v)$. We consider that $u_b, v_b = 0$. The values we will explore of C_d^b are given in Tables 7.3 and 7.4.

We also examined the effect of the oceanic topography's bottom drag in two different scenarios: free-slip and no-slip. In the no-slip scenario, the normal and tangential components of the fluid velocity field are both equal to zero at the interface between a moving fluid and a stationary wall. In the free-slip scenario, the normal component of the fluid velocity field is equal to zero at the interface, but the tangential component is unrestricted. This condition is also known as the no-penetration condition.

Atmospheric forcing

The surface conditions, evaluated at $z = \zeta$ are

$$K_M \frac{\partial u}{\partial z} = \tau_s^x(x,y,t); \quad K_M \frac{\partial v}{\partial z} = \tau_s^y(x,y,t); \quad K_H \frac{\partial T}{\partial z} = 0; \quad K_H \frac{\partial S}{\partial z} = 0 \tag{7.27}$$

Where τ_s^x and τ_s^y are the components of the wind stress acting on the free surface in the x and y directions, respectively. We have assumed there is no exchange of heat and salinity with the atmosphere. Moreover, we have chosen a simple wind stress given by

$$\tau_s^x(x,y,t) = C_d^s \cdot (u - u_w)\|\mathbf{u} - \mathbf{u}_w\|, \quad \tau_s^y(x,y,t) = C_d^s \cdot (v - v_w)\|\mathbf{u} - \mathbf{u}_w\|, \tag{7.28}$$

where u_w, v_w refers to the eastward and northward wind speed components and $\mathbf{u} = (u,v)$. The C_d^s values we have explored are given in Tables 7.3 and 7.4.

The winds were computed using the NCAR Weather Research Forecasting (WRF) model version 4.0. which is a fully compressible, Eulerian non-hydrostatic equations model (with a run-time hydrostatic option) that uses Arakawa-C grid staggering for horizontal discretization and the time-split 3rd ordered Runge Kutta integration scheme. It includes various parameterizations and schemes for microphysical processes, cumulus parameterization, land-surface modeling, boundary layer parameterization, long-wave and short-wave radiation interactions in the atmosphere. For this study, the parameterizations and schemes used were as follows: surface layer based on the Monin-Obukhov Similarity scheme, incorporating a Carlson-Boland viscous sub-layer and standard similarity functions (Beljaars, 1995); land-surface parametrization from the Thermal Diffusion scheme, using a soil temperature-only scheme with five layers; boundary-layer YSU scheme (Hong et al., 2006); and the Noah land-surface model. The model domain encompasses the geographical region of the Greek territory, ranging from 23.64 °N to 24.36 °N in latitude and from 33.7 °E to 34.35 °E in longitude. The horizontal grid spacing is set at 800 meters, and there are 34 vertical levels within the model.

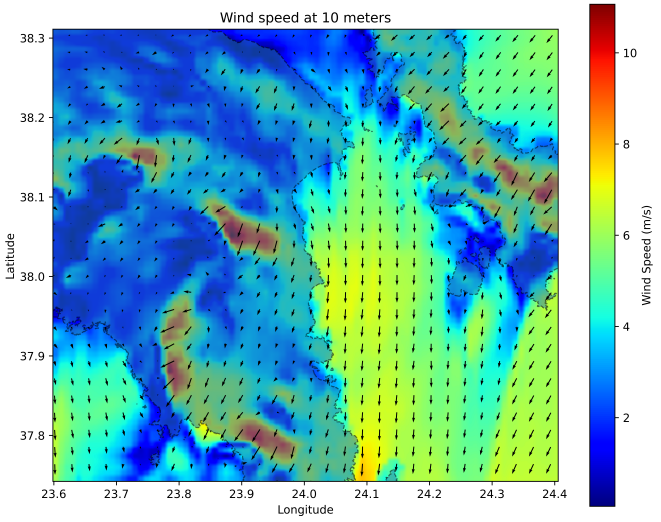

Figure 7.3 The figure depicts the WRF domain, with the wind speed intensity at 10 meters above the ground visualized in the background. The visualization corresponds to the specific date and time of November 2, 2019, at 12:00:00. Arrows are employed to indicate the direction of the wind.

The model assimilates the ERA5 data, obtained from both single and pressure levels, as a data source (Hersbach et al., 2020). Figure 7.3 displays the plotted wind speed at a height of 10 meters.

Open boundary conditions

In this study, we have set up a model that aspires to provide realistic and informative high-resolution fields in the sense of operational oceanography. This requires careful nesting on the boundaries and in our setting, we have considered that the CMEMS product in the Mediterranean Sea offers good estimations for the required external fields on the described boundaries below. The Mediterranean Forecasting System's physical component (Med-Physics) consists of a combined hydrodynamic-wave model that covers the entire Mediterranean Basin, including tides. The model has a horizontal grid resolution of about 4 km (1/24°) and features 141 unevenly spaced vertical levels. The hydrodynamics are derived from the Nucleus for European Modelling of the Ocean (NEMO v3.6) and incorporate tidal representation, while the wave component comes from Wave Watch-III. Model solutions are adjusted using a 3DVAR assimilation scheme (OceanVar) that incorporates temperature and

salinity vertical profiles, as well as satellite Sea Level Anomaly observations along the track (Clementi et al., 2019).

We define now conditions at the lateral boundaries. First, we take into consideration tides that constrain sea surface height and barotropic velocities at the boundaries. ROMS adjusts tides through the Chapman and Flather boundary conditions, which we detail next.

Chapman boundary condition. This condition for surface elevation was investigated by Chapman (D. C. Chapman , 1985), assuming all outgoing signals leave at the shallow-water wave speed of $\sqrt{gD}$.

$$\frac{\partial \zeta}{\partial t} = \pm\sqrt{gh}\frac{\partial \zeta}{\partial x} \tag{7.29}$$

where ζ is the sea surface elevation at an open boundary.

Flather boundary condition For the normal component of the barotropic velocity, one option is to radiate out deviations from exterior values at the speed of the external gravity waves (R. A. Flather , 1976). The radiation condition for the normal component of the barotropic velocity $\overline{u}_n$ applied in the outwardly normal direction at an open boundary is:

$$\overline{u}_n = \overline{u}_n^{\text{ext}} - \sqrt{\frac{g}{h}}\left(\zeta - \zeta^{\text{ext}}\right) \tag{7.30}$$

where $\overline{u}_{\text{ext}}$ represents the external barotropic velocity and h is the local water depth.

The exterior values are used to provide tidal boundary conditions to the barotropic mode. In limited area coastal domains -as it is our case- the tides can be treated as being entirely remotely forced, i.e., the influence of the gravitational tide generating forces within the domain is negligible. The principal challenge to modeling tides accurately is the proper representation of tidal elevation and velocity boundary conditions around the entire model perimeter (R. He and J. L. Wilkin , 2006), but as explained those values are taken from CMEMS products.

For the rest of the fields, that is baroclinic velocities, salinity, and temperature, which we refer to generically as ϕ, ROMS has various types of boundary conditions including open, closed, and periodic. See (Marchesiello et al., 2001) for a more thorough exploration of the options. We examined the effects of several of those conditions: mixed radiation-nudging open boundary conditions, clamped boundary conditions, and the use of a sponge layer.

Clamped boundary condition. This is a Dirichlet type of boundary condition. It consists in setting the boundary value to a known exterior value:

$$\phi = \phi_{\text{ext}} \tag{7.31}$$

Here ϕ_{ext} represents the exterior value of the field ϕ, provided in our case by the CMEMS Med-Physics data.

Mixed radiation-nudging boundary condition. Open boundary conditions in coastal ocean modeling can be challenging to implement due to the possibility of incoming and outgoing flow at the same boundary or at different depths at the same horizontal location. A mixed boundary condition combining radiation and nudging, first introduced in (Marchesiello et al., 2001), has been proposed as a solution. This boundary condition uses the radiation condition to determine whether the boundary is passive (outward propagation) or active (inward propagation). In the passive case, the solution is allowed to pass through the boundary using radiation extrapolation to prevent excessive reflection. In the active case, the solution is nudged towards external data sources, such as observed climatologies or large-domain model outputs, to provide the necessary information for the dynamical equations without over-specifying the solution. One-way nesting can also be used when the external data is taken from time-evolving large-domain model solutions.

The radiation condition for a prognostic model variable ϕ is:

$$\frac{\partial \phi}{\partial t} = -\left(c_x \frac{\partial \phi}{\partial t} + c_y \frac{\partial \phi}{\partial t} \right) \tag{7.32}$$

where (x, y) are respectively, the normal and tangential directions to the boundary in local Cartesian coordinates. The phase speeds (c_x, c_y) are projections of the oblique radiation, calculated from the ϕ field surrounding the boundary point as follows:

$$c_x = -\frac{\partial \phi}{\partial t} \frac{\partial \phi / \partial x}{\left(\frac{\partial \phi}{\partial x}\right)^2 + \left(\frac{\partial \phi}{\partial y}\right)^2} \tag{7.33}$$

and

$$c_y = -\frac{\partial \phi}{\partial t} \frac{\partial \phi / \partial y}{\left(\frac{\partial \phi}{\partial x}\right)^2 + \left(\frac{\partial \phi}{\partial y}\right)^2}. \tag{7.34}$$

In the active boundary, we apply the nudge equation. The nudging layer is a region where model data is relaxed towards external data. For this region, a nudging term is added to the equations of tracers and surface elevation. Its mathematical form is added to the right-hand side of the prognostic equations as follows:

$$\frac{\partial \phi}{\partial t} = \text{r.h.s} - \frac{1}{\tau_{\text{nud}}} (\phi - \phi^{\text{ext}}). \tag{7.35}$$

Parameter	Value	Description
Lm	344	number of points in longitude direction
Mm	228	number of points in latitude direction
N	10	number of vertical (sigma) levels
$h_{\max}$	146	maximum depth of the domain (metres)
$h_{\min}$	0.29	minimum depth of the domain (metres)
θ_s	5.0	sigma coordinate surface stretching factor
θ_b	0.4	sigma coordinate bottom stretching factor
Δ_t	10	baroclinic time-step (seconds)
Δ_{tt}	7	barotropic time-step (seconds)

Table 7.2 Numerical values for the parameters associated with the setup of the ocean model.

In our work, when mixed radiation-nudging boundary condition is used, $\tau_{\text{nud}} = 10$ days. The selected value was determined based on a typical advective timescale: Given our grid size of 80 m and maximum velocities of 0.01 m/s, we derive a timescale of 80/0.01 = 8000 seconds, which equates to approximately 10 days for the inflow.

Sponge layer. It is typically used to dump noisy effects at the boundaries due to discrepancies between the evolving model solution in the domain and the external data in which it is nested. This is implemented by increasing there the coefficients that enhance the horizontal mixing. Both a factor that multiplies the horizontal mixing and its width are indicated (see Table 7.4).

7.2. Remote sensing

The waters surrounding the Rafina Port and its vicinity are oligotrophic-like (clear and transparent), which limited the number of available turbidity images that could contribute to the qualification of the Rafina Port hydrodynamic model. To qualify the hydrodynamic model, data from the Sentinel 2A and 2B Multi-Spectral Instrument (MSI) were examined for the period ranging from November 1st, 2019 to January 31st, 2020.

Sentinel 2A and 2B had a revisiting cycle of 5 days. Level 1C Top of Atmosphere reflectance products from Sentinel 2 were downloaded from the Sentinel Data Hub. The standard SEN2COR library of atmospheric correction algorithms, provided by Scihub Copernicus, for the Sentinel 2 MSI sensor was initially designed for land applications. However, for the purpose of reporting ocean color-derived products and qualifying the hydrodynamic model outputs, Level 2 data required an atmospheric correction algorithm specifically designed to handle the radiometric constraints of water pixels data. As a result, the ACOLITE toolbox (Q. Vanhellemont and K. Ruddick , 2018) was selected. ACOLITE enabled easy

and efficient processing to correct Sentinel-2 Level 1C data and generate value-added derived products for both coastal and inland waters through the use of a dark spectrum algorithm for atmospheric correction (Vanhellemont, 2019).

The ACOLITE atmospheric correction generates Level 2 images that include biogeochemical-derived products such as turbidity (Nechad et al., 2009) and suspended matter (Nechad et al., 2010), among others. Additionally, the ACOLITE toolbox includes sunglint correction developed by T. Harmel and M. Chami and T. Tormos and others (2018). These images are useful for model qualification as ACOLITE produces both well-corrected and water discoloration products, including phytoplankton blooms, turbidity, and suspended matter. The spread of these compounds, as evidenced by water discoloration, makes visible the convoluted shapes of the dynamical objects that we will explain in detail in the next section. As a result, the patterns shown in remote sensing images can be correlated with patterns obtained from the hydrodynamic model. Conversely, in the absence of these compounds, the use of very high-resolution images for this purpose is limited. Figure 7.4 shows patterns visible on the sea surface in the Rafina Port area on November 22, 2019, as captured by Sentinel 2 satellite images. Figure 7.4a) depicts a quasi-true color image in RGB (using band 4, band 3, and band 2 of the MSI sensor), while Figure 7.4b) shows a pseudocolor turbidity image in Formazin Nephelometric Units (FNU).

Ocean and Land Colour Instrument (OLCI) Level 1B data, covering the study area, were acquired from Sentinel 3A and 3B via the Sentinel Data Hub. These data underwent processing using SeaDAS version 8.2 to produce the required outputs. Ancillary files needed for atmospheric correction were obtained using the "getanc.py" routine. The l2gen SeaDAS binary was utilized to derive geophysical variables, resulting in Level 2 files. These files include remote sensing reflectances and [Chlorophyll-a], among other ocean color products. To produce projected images onto a geographical Lat/Lon WGS84 GeoTIFF, Sentinel 3 Level 2 files were mosaicked by satellite and day using the Graphic Processing Tool (gpt.sh) Mosaic operator. Figure 7.5 displays the sea surface patterns captured by Sentinel 3 A and B in the same area. Despite the lower resolution, higher frequency passes enabled the identification of a longer series during the study period. This series also includes an image taken on November 22nd, where Sentinel 2 provided a higher resolution.

7.3. The dynamical systems perspective

Images displayed in section 7.2 show patterns that correspond to Particulate or Dissolved, Organic or Inorganic Matter (POM, DOM, PIM, DIM), Chlorophyll, Turbidity, etc., with different origins (primary production blooms, sediments, wastewater plumes). These light

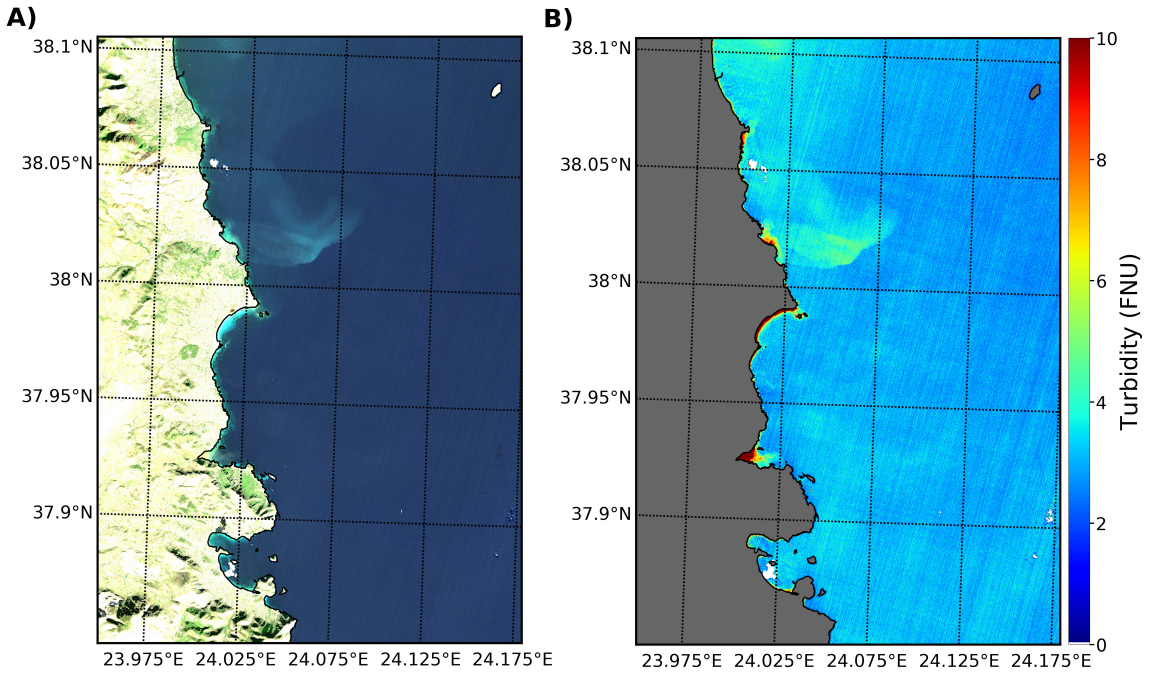

Figure 7.4 Sentinel 2 images on the 22nd of November 2019 in the Rafina Port area showing convoluted shapes. (a) Quasi-true RGB color image;(b) turbidity image obtained from ACOLITE algorithms.

passive particles, suspended in the ocean, are described by a concentration field, C, whose general evolution is given by equation (7.5). Assuming that at the surface motion is mainly horizontal, equation (7.5) can be reduced to the following advection-diffusion equation:

$$\frac{\partial C}{\partial t} + \mathbf{v}_h \cdot \nabla C = \mu \nabla^2 C, \tag{7.36}$$

where μ is the horizontal molecular diffusion and $\mathbf{v}_h$ is the vector with the horizontal velocity components of the ocean model. Assuming that at our scales advection is the dominant factor in transport (see (Garcia-Garrido et al., 2015; García-Sánchez et al., 2022b; García-Sánchez et al., 2021; Lekien and Marsden, 2005; Olascoaga and Haller, 2012)) then $\mu \sim 0$ and equation (7.36) reduces to:

$$\frac{\partial C}{\partial t} + \mathbf{v}_h \cdot \nabla C = \frac{dC}{dt} = 0. \tag{7.37}$$

This equation assumes that C is conserved along the fluid parcel trajectories. Fluid parcels on the ocean surface follow trajectories in longitude/latitude coordinates $\vec{x}(t) = (\lambda(t), \phi(t))$

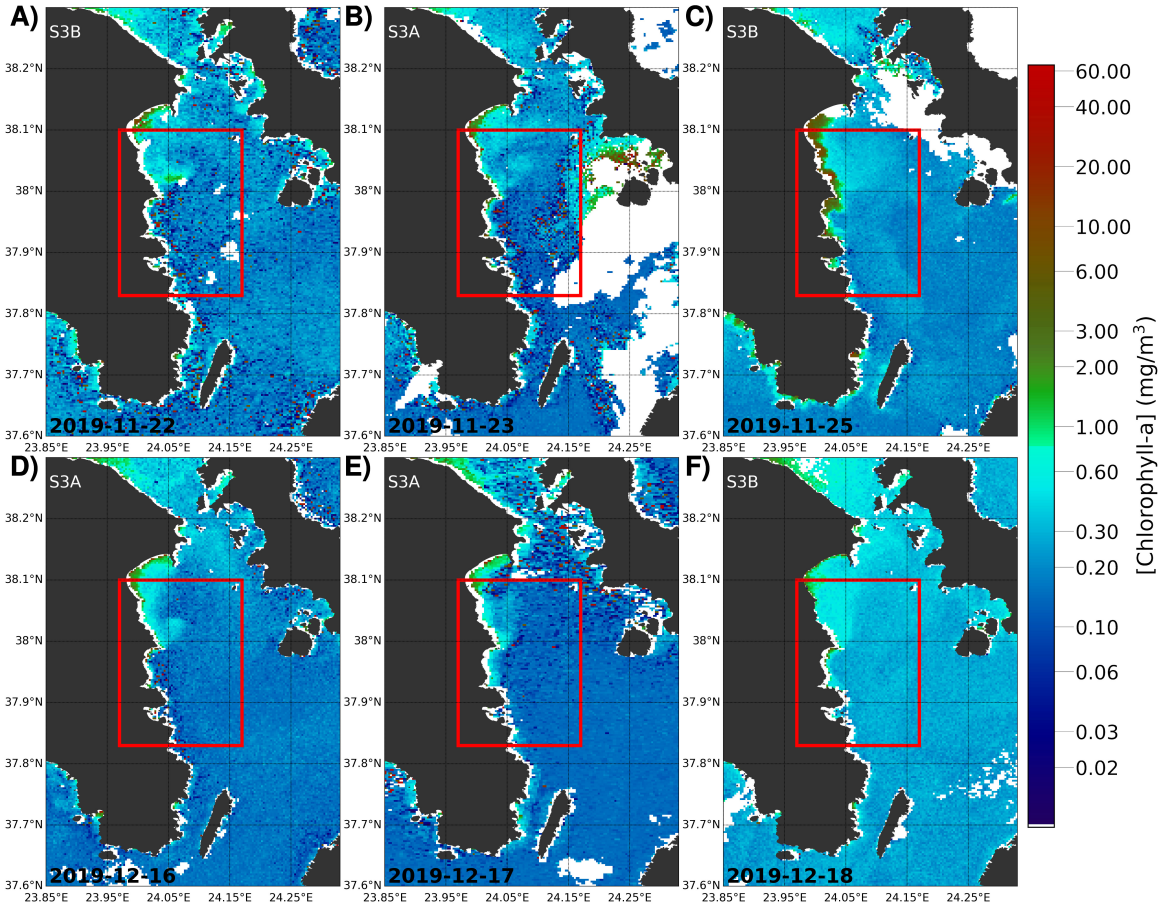

Figure 7.5 Sentinel 3A and B images in the Rafina Port area showing convoluted shapes of chlorophyll. (a) on the 22th of November 2019, (b) on the 23th of November 2019, (c) on the 25th of November, (d) on the 16th of December, (e) on the 17th of December, and (f) on the 18th of December. Red rectangles mark the region where very high-resolution simulations have been performed.

that evolve according to the dynamical system:

$$\begin{aligned} \frac{d\lambda}{dt} &= \frac{u(\lambda,\phi,t)}{R\cos\phi}, \\ \frac{d\phi}{dt} &= \frac{v(\lambda,\phi,t)}{R}. \end{aligned} \tag{7.38}$$

where R is the Earth's radius and u and v are the eastwards and northwards velocity components provided by the hydrodynamical model at the surface layer.

In order to characterize the performance of u and v to consistently describe patterns observed in satellite images in Figures 7.4 and 7.5, we are going to extract geometrical structures from Equation (7.38) using specific velocity fields obtained under different settings of the hydrodynamical model. The geometrical structures that we will use, the Lagrangian Coherent Structures (LCS), provide a signature for a specific velocity field that highlights the essential transport features associated with it. LCS form time-dependent material surfaces that separate fluid paths that behave differently. An important mathematical result is that these Lagrangian patterns are robust against velocity field perturbations, whereas the comparison of two individual trajectories is not. This allows a better characterization of the velocity fields produced by the model, by allowing to establish as different outputs those that have a different Lagrangian signature, while those that present a similar Lagrangian pattern, can be characterized as similar. This perspective has been successfully employed in pollution contexts (García-Sánchez et al., 2022b).

The LCS spatio-temporal template can be constructed with the technique referred to as Lagrangian Descriptors (LDs). The particular LD that we use is a function referred to as M (Madrid and Mancho, 2009; Mancho et al., 2003, 2013) which is defined as follows:

$$M(\vec{x}_0,t_0,\tau) = \int_{t_0-\tau}^{t_0+\tau} \|\mathbf{v}_h(\vec{x}(t),t)\| = \int_{t_0}^{t_0+\tau} \|\mathbf{v}_h(\vec{x}(t),t)\| + \int_{t_0-\tau}^{t_0} \|\mathbf{v}_h(\vec{x}(t),t)\|. \tag{7.39}$$

where $\|\cdot\|$ stands for the modulus of the velocity vector. In this expression, the computation of the function M is split into its forward time (M^f) and backward time (M^b) contributions. At a given time t_0, the function $M(\vec{x}_0,t_0,\tau)$ measures the arc length traced by the trajectory starting at $\vec{x}_0 = \vec{x}(t_0)$ as it evolves forward and backward in time for a time interval τ. For a sufficiently large τ, the function M exhibits a distinct structure that reveals singular features emphasizing the Lagrangian Coherent Structures (LCS). Figure 7.6 displays the calculation of M^b in the vicinity of Rafina port for $\tau = 3$ days on selected dates consistent with those of Figure 7.5. To compute Figure 7.6, trajectories in Equation (7.39) are integrated with a 5^{th} order Runge-Kutta method, and arc length is computed by the addition of linear segments connecting successive steps of the Runge-Kutta method.

Parameter	Value
Horizontal Viscosity $A_{u,v}$	2
Horizontal Diffusivity $A_{T,S}$	2
Bottom Drag factor C_d^b	0.003
Sponge factor	1
Wind drag factor C_d^s	$6.0 \cdot 10^{-5}$
Bathymetry	NAVIONICS
Boundary conditions	Clamped

Table 7.3 This table presents the numerical values associated with each parameter utilized in the base solution

In Equation (7.39) the backward integration (M^b) highlights the structure of attracting LCS and we expect that suspended material will eventually, after a transient time, be aligned with these features. Patterns visible from satellite imagery correspond to suspended material that could decay towards these features (García-Sánchez et al., 2022a,b; García-Sánchez et al., 2021). Additionally dynamical barriers on the sea surface could also be made visible by the suspended matter, as barriers would keep the suspended material on both sides unmixed as far as the original distribution of the suspended material was only on one side of the barrier.

7.4. Numerical experiment setups and performance quantification

The hydrodynamical model can be set up with different parameters and boundary conditions, which can lead to different outputs, particularly in the currents. Typically, these free parameters are adjusted by benchmarking ocean model outputs against in situ Eulerian metrics obtained from Acoustic Doppler Current Profiler (ADCP), mooring data, and other sources. In this work, we aim to evaluate the performance of these models from a Lagrangian perspective by using satellite imagery, as described in the previous section.

We begin by establishing a configuration for a Base Solution (BS) with parameters provided in Table 7.3, which complement those shown in Table 7.2 and are kept constant. We execute this configuration during the timeframe for which reference images are accessible. These consist of two consecutive periods in 2019 (refer to Figures 7.4 and 7.5), with a total of six images. The first period ranges from 2019-11-22 to 2019-11-25, while the second period spans from 2019-12-15 to 2019-12-18. To ensure that these outputs are not dependent on the initial conditions used, the system is initialized prior to the period of interest and run

for a sufficient period of time to converge to the global attractor. Given that our system is subject to time-dependent boundary conditions (such as winds and open lateral boundary conditions), the type of attractor involved is called a pullback attractor (T. Tachim Medjo, 2018). When LCS are computed using velocity fields from different initial conditions, there are no discrepancies observed once the solutions have converged to the pullback attractor.

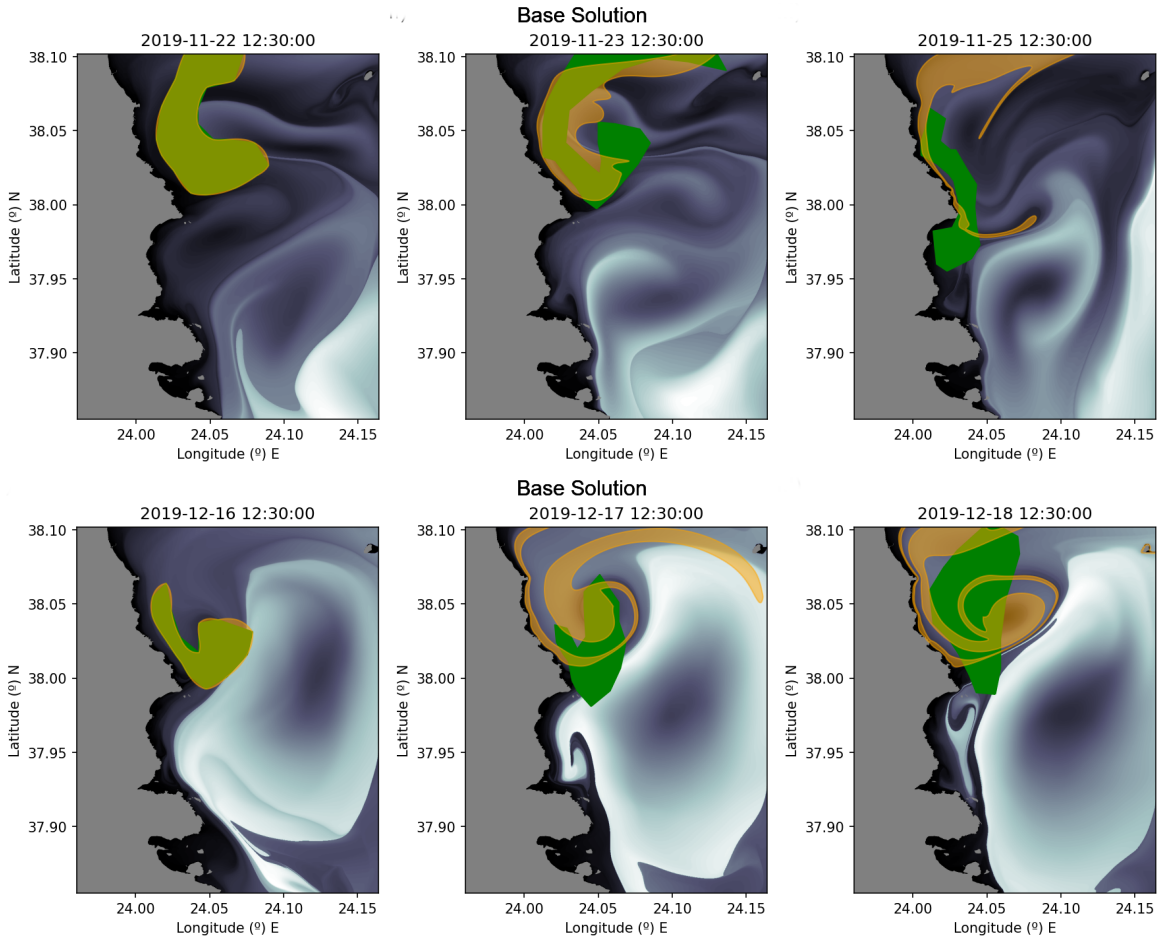

Figure 7.6 Evaluation of M^b on the BS model for $\tau = 3$ days. Patterns are displayed in a gray tone. Panels a), b), and c) show the results on the time series correlated to the satellite imagery displayed in panels a), b), and c) of Figure 7.5. Panels d), e), and f) show the results on the time series correlated to the satellite imagery displayed in panels d), e), and f) of the same figure. The green blobs show the contours of an estimation of the evolution of chlorophyll from the satellite images. The brown blobs show the evolution according to the model of the green blob at the initial date of each time series.

Defining a metric that provides a quantification to compare the sequence of satellite observations with the performance of the hydrodynamic model outputs is not an easy task. The reason for this difficulty is that it involves comparing complicated and subtle dynamical

objects. To accomplish this, we have proposed a methodology that makes assumptions about both the observations and the models. Regarding observations, we have extracted polygons from the satellite imagery that represent zones where the chlorophyll is homogeneously distributed. Figure 7.6 shows a sequence of green polygons for the two periods. Assuming that these structures are formed by suspended particles and are purely advected by the currents, they provide a ground truth or benchmark to be recovered by the model. This figure also shows, in brown, the evolution of the chlorophyll blobs that were initialized on the first day of the sequence by using the velocity fields from the base solution set. In the background, for interpretation purposes, we have represented the evaluation of M^b for $\tau = 3$ days, which highlights, through singular features, the attracting material curves of the flow. There is a nice consistency between these features and the evolution of the brown blob. Ideally, if the model is good we would expect a lot of overlap between the green and brown blobs. Certainly, for the suspended particulate matter there may be sinks and/or sources and this is reflected in the fact that the sequence of green blobs does not preserve the area. Additionally, diffusion adds to spreading on the ocean surface. These phenomena are not described by pure advection, but still, the overlap is an intuitive measure to consider. For each sequence, in the days after the first one, we establish as a measure the area fraction of the green blob that is covered with the brown blob. This will be a number $\mathscr{A}$ satisfying $0 \leq \mathscr{A} \leq 1$ that we interpret as follows, close to 1 means good performance while close to 0 implies poor performance. We will comment further on these images in the results section.

We complete this section by describing a series of free parameter configurations in the hydrodynamic model. These are defined from variations of the parameters taken for the base solution and define a series of experiments. Our study aims to qualify the results of all these experiments, using the newly defined metric. The experiments are divided into six categories:

- C1: Varying horizontal mixing coefficients (viscosity and diffusivity) in two experiments compared to the Base Solution (BS).
- C2: Investigating two different bottom drag coefficients in comparison to the BS.
- C3: Assessing two distinct surface forcing wind stress fields relative to the BS.
- C4: Conducting a single experiment with bathymetry replaced by GEBCO data.
- C5: Implementing a sponge layer with six times the base horizontal viscosity and diffusivity in one experiment.
- C6: Executing two experiments where the Open Boundary Condition (OBC) was replaced by the mixed radiation-nudging boundary condition, modifying the factor between passive (outflow) and active (inflow).

Details of the parameters taken for each experiment can be found in Table 7.4.

Summary of experiments

Category	**Experiment**	**Parameters**
C1: Horizontal Mixing Coefficient	Exp 1	$A_{u,v} = A_{T,S} = 0.2m^2/s$
	Exp 2	$A_{u,v} = A_{T,S} = 5m^2/s$
C2: Bottom Drag Coefficient	Exp 1	$C_d^b = 0.03$ (non-dimensional)
	Exp 2	$C_d^b = 3 \cdot 10^{-5}$ (non-dimensional)
C3: Wind stress	Exp 1	$C_d^s = 6 \cdot 10^{-4}$
	Exp 2	$C_d^s = 6 \cdot 10^{-7}$
C4: Modified Bathymetry	Exp 1	GEBCO data (Fig. 7.1 b))
C5: Sponge at Boundary	Exp 1	$6 \cdot A_{u,v,T,S}$
C6: Mixed Radiation-Nudging BC	Exp 1	No sponge, $\tau_{\text{nud}} = 10$ days,
	Exp 2	Sponge, $\tau_{\text{nud}} = 10$ days

Table 7.4 Setting the varying parameters for defining categories and experiments to conduct sensitivity tests.

7.5. Results

First, we comment on the results displayed in Figure 7.6. The upper row shows a sequence of satellite imagery captured between November 22nd and 25th, 2019, where chlorophyll is visible. On November 23rd, the tracer appears to swirl, while on November 25th, the chlorophyll in the upper half of the domain has diffused, weakening all features except for a large concentration aligned with the coast. A material barrier transverse to the coast at around 38 degrees North appears to persist in all these upper panels. The dynamical structure of the currents of the BS model is obtained from M^b, whose pattern is displayed in the gray tones in the background. The attracting material curves are visible through the singular features and consistently show the transverse barrier to the coast present in the observations. The evolution of the blob according to the BS model is depicted in brown, which also exhibits swirling (panel b) and contraction towards the coast (panel c). The bottom row displays satellite imagery where chlorophyll is visible between December 16th and 18th, 2019. On December 16th, the chlorophyll tracer has a swirling shape. The boundary of this shape progressively weakens on December 17th and 18th. A pronounced transverse barrier to the coast in a northeasterly direction evolves progressively, bringing its alignment closer to the north. The M^b pattern is shown in the gray tones in the background of the image. It confirms the presence of a barrier in a northeasterly direction, although with a slightly different inclination than that of the satellite images. According to the BS model, the brown

blobs swirl counterclockwise as they evolve. The first row of Table 7.5 provides values of the computed $\mathscr{A}$ for the first chlorophyll series on November 23rd and 25th, 2019, and for the second chlorophyll series on December 17th and 18th, 2019, quantifying the performance of the BS model. In addition to this data, Table 7.6 shows the averages of these quantities for the first and second periods as well as for the total period.

Tables 7.5 and 7.6 also provide quantification of the performance of all experiments. Results for $\mathscr{A}$ fluctuate between 0 and 0.75 for individual experiments, and between 0.2 and 0.65 for averaged values. Averaged values of $\mathscr{A} \sim 0.2$ or individual values of $\mathscr{A} \sim 0.1$ indicate poor performance. During the first period, extremely low performances on individual days are obtained for instance on 25, November 2019 for the category 4 model that uses the GEBCO bathymetry (C4, exp1) and for the sponge layer experiment (C5,exp1) that introduces high diffusivity and viscosity on the boundaries of the domain. Explicit representations for selected poor-performing cases are provided in Figure 7.7, where the top two rows are represented the cases (C4,exp1) and (C5,exp1). The highest-performing model for the first period corresponds to the (C6, exp2) experiment that implements a mixed sponge and radiation-nudging condition. The last row in Figure 7.7 provides a visualization of the performance of this model. Remarkably, its dynamical structure allows the blob to be maintained elongated along the coast, although the model also shows incursions towards the interior of the sea.

Regarding the second period, the top two rows of Figure 7.8 represent simulations performed with the (C1, exp1) model, which decreased the horizontal viscosity and diffusivity coefficients, and the (C6, exp1) model, which considers only a radiation-nudging condition. Both simulations perform poorly. The (C1, exp1) model presents invariant dynamical structures that are very rich and involve very small scales. Some of these structures remain within the observed green blob. The (C6, exp1) model performs poorly. The absence of a sponge effect at the boundary in the (C6, exp1) model influences the solution compared to what is obtained by considering it in the (C6, exp2) model. The latter is illustrated in the bottom row, the (C6, exp2) model. According to the values given in Table 7.5, the performance is rather good on the 17th but decays on December 18th, 2019.

The effects of different models performing differently on different days and periods can be clearly observed in Table 7.5 and Table 7.6. For example, model (C6, exp2) obtained with the mixed sponge radiation-nudging condition performs rather consistently in the first period, but worse in the second period. The same occurs for the experiment that considers only the radiation-nudging condition (C6, exp1). On the contrary, the model (C1, exp2) obtained by increasing horizontal viscosity and diffusivity performs more consistently in the second period, than in the first period. Similarly occurs for the model (C2, exp1) which increases the

bottom drag coefficient. All in all, the total average column in Table 7.6 confirms that (C6, exp2), with the mixed radiation-nudge condition, has the best performance and the initial BS choice has moderate performance.

Experiments	**2019-11-23**	**2019-11-25**	**2019-12-17**	**2019-12-18**
B.S	0.49919	0.085	0.3669	0.2720
C1. Horizontal mixing exp 1	0.3953	0.1185	0.2065	0.2802
C1. Horizontal mixing exp 2	0.4654	0.3188	0.4875	0.3815
C2. Bottom drag exp 1	0.4224	0.1096	0.3618	0.4835
C2. Bottom drag exp 2	0.4375	0.3165	0.2282	0.3676
C3. Wind stress exp 1	0.4462	0.4343	0.3164	0.3224
C3. Wind stress exp 2	0.4883	0.087	0.3793	0.2848
C4. Modified bathymetry exp 1	0.4491	0.005	0.1305	0.2363
C5. Sponge exp 1	0.3778	0.0278	0.29965	0.2528
C6. Mixed radiation-nudging exp 1	0.5315	0.3682	0.2337	0.1660
C6. Mixed radiation-nudging exp 2	0.5555	0.7476	0.5192	0.2551

Table 7.5 Results of measured index $\mathscr{A}$ obtained for the sensitivity experiments. they include the first period (2019-11-23 and 2019-11-25), and the second period (2019-12-17 and 2019-12-18).

Experiments	**Avg First Period**	**Avg Second Period**	**Total Avg**
B.S.	0.2922	0.3195	0.3058
C1. Horizontal mixing exp 1	0.2569	0.2433	0.2501
C1. Horizontal mixing exp 2	0.3921	0.4345	0.4133
C2. Bottom drag exp 1	0.2660	0.4226	0.3443
C2. Bottom drag exp 2	0.3770	0.2980	0.3375
C3. Wind stress exp 1	0.4402	0.3194	0.3798
C3. Wind stress exp 2	0.2876	0.3321	0.3099
C4. Modified bathymetry exp 1	0.2273	0.1834	0.2054
C5. Sponge exp 1	0.2028	0.2762	0.2395
C6. Mixed radiation-nudging exp 1	0.4498	0.1998	0.3249
C6. Mixed radiation-nudging exp 2	0.6515	0.3871	0.5194

Table 7.6 Averages of measured index $\mathscr{A}$ for the first and second periods.

7.6. Conclusions

In this paper, we explore a methodology based on the use of dynamical systems ideas to assess the quality of results from different configurations of a high-resolution coastal ocean model. Our aim is to leverage satellite imagery, which provides observations at a lower

cost than in situ observations, and to propose a strategy for quantifying the quality of model results using an $\mathscr{A}$ index. The models are defined by specifying parameters or boundary conditions of the system with various options that are not known beforehand.

We have found that many model configurations produce reasonable results and that the choice of boundary conditions for nesting has a significant impact. Among these, radiation-nudging lateral boundary conditions appear to be particularly suitable. The coupling with the wind at the surface, the adherence at the bottom, and parameters related to the horizontal mixing can all cause distortions in the solutions, leading to deviations from observations.

We expect that this methodology will be useful for adjusting high-resolution coastal models in regions where in situ observations are scarce, and it also opens up new avenues for the application and exploitation of satellite imagery.

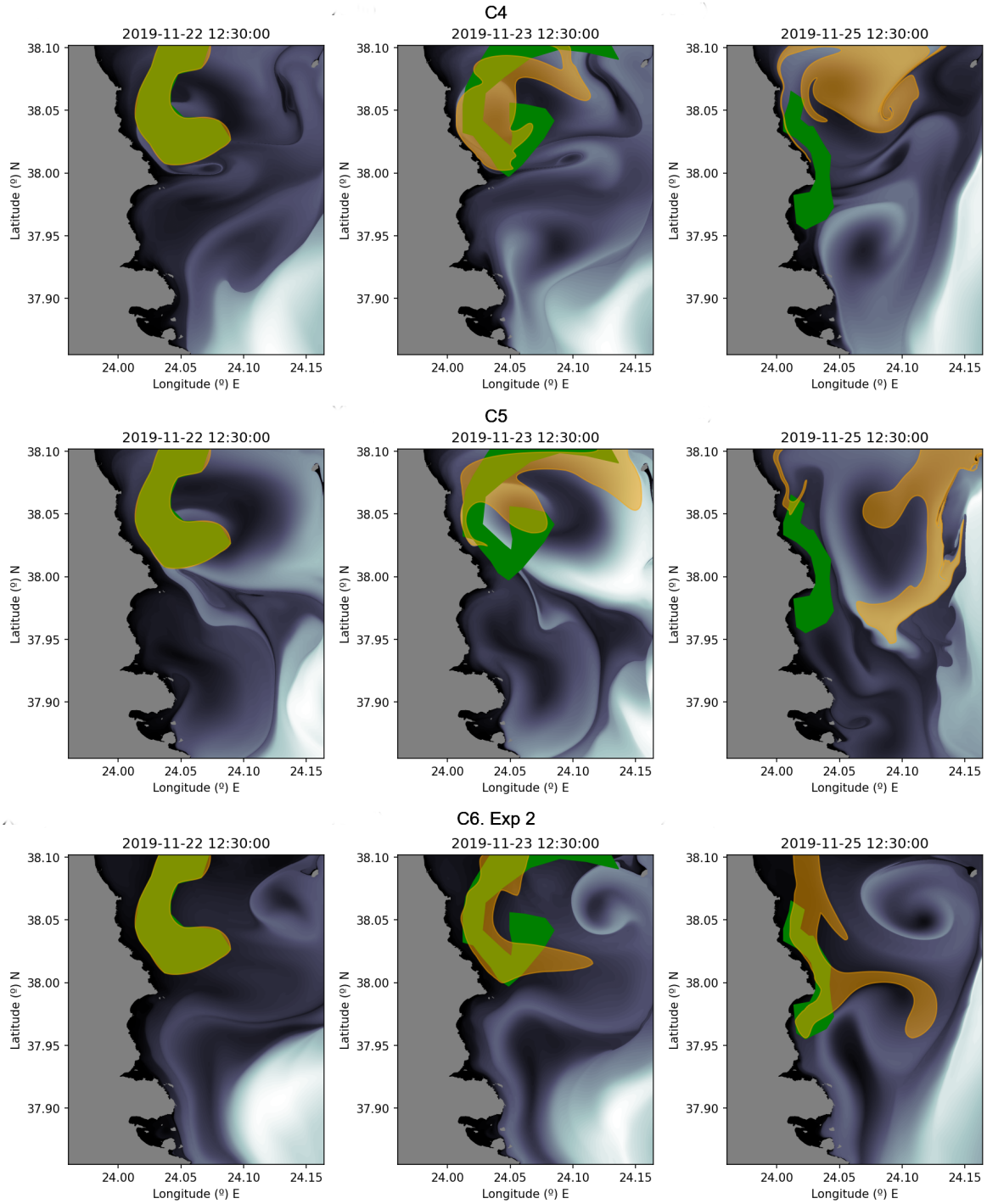

Figure 7.7 Evaluation of M^b on several models for $\tau = 3$ days. Patterns are displayed in a gray tone. The first, second, and third columns show the results on the time series correlated to the satellite imagery displayed in panels a), b), and c) of Figure 7.5. The first row shows the results for Category 2, experiment 2, on the bottom drag condition. The second row shows the results for Category 5, experiment 1, on the sponge conditions. The third row shows the results for Category 6, experiment 2, on the mixed radiation-nudging conditions. The green blobs show the contours of an estimation of the evolution of chlorophyll from satellite images. The brown blobs show the evolution according to each model of the green blob at the initial date of each time series.

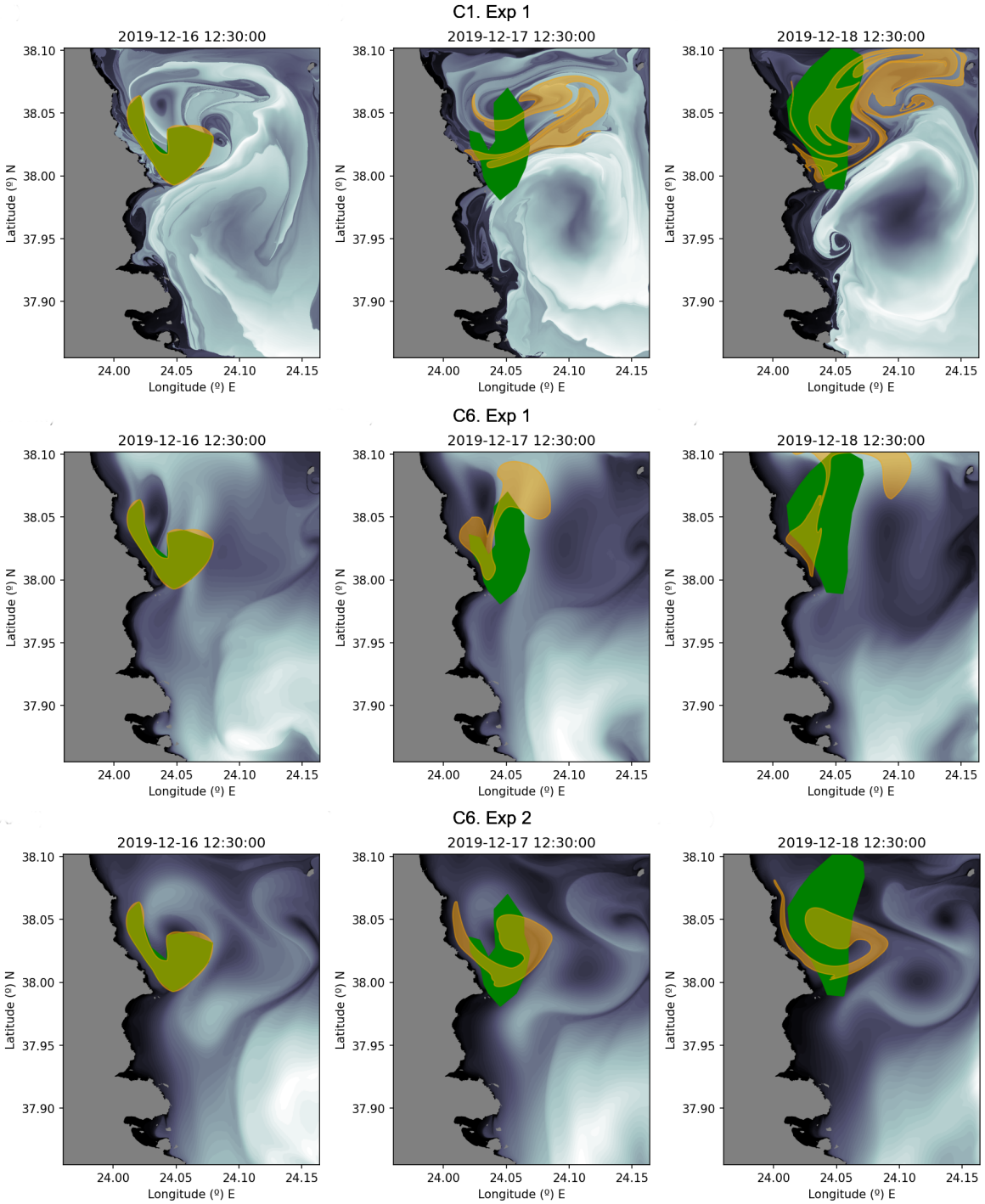

Figure 7.8 Evaluation of M^b on several models for $\tau = 3$ days. Patterns are displayed in a gray tone. The first, second, and third columns show the results on the time series correlated to the satellite imagery displayed in panels d), e), and f) of Figure 7.5. The first row shows the results for Category 1, experiment 1, on the horizontal diffusion and viscosity coefficients. The second row shows the results for Category 3, experiment 1, on the wind stress conditions. The third row shows the results for Category 6, experiment 2, on the mixed radiation-nudging conditions. The green blobs show the contours of an estimation of the evolution of chlorophyll from satellite images. The brown blobs show the evolution according to each model of the green blob at the initial date of each time series.

Chapter 8

Conclusions and Outlook

The results of the research conducted in this PhD thesis have been discussed in the conclusion sections of Chapters 3, 4, 5, 6, 7. To facilitate the readers, this final chapter provides a compilation of these conclusions. Additionally, a brief discussion on potential avenues for future research is presented.

8.1. Research conclusions

In conclusion, the chapters presented in this thesis highlight the advancements and insights gained through the application of emerging tools, which involve high-resolution models, remote sensing techniques, and dynamical systems approaches in coastal and oceanic contexts. These findings have important implications for the management of pollution, the quantification of uncertainties, the assessment of models, and environmental protection.

Chapter 3 demonstrates the effectiveness of using high-resolution hydrodynamic models, remote sensing satellite images and dynamical systems tools to manage a specific pollution event. The use of such tools provides accurate responses and reduces uncertainties in the prediction of oil spills, thus supporting real-time decision-making by emergency services. In particular, the use of LCS on different data sets provided by various services, emphasize their role in understanding the transport in the analysed data and capturing essential features that control dispersion. A consistent geometric pattern has been identified, particularly a hyperbolic trajectory in a detachment configuration and its unstable and stable manifolds. Although both elements are present in the data, the high-resolution models provide superior quantitative results.

The introduction of a new definition for UQ in Chapter 4 expands the traditional understanding of UQ in oceanic contexts. This definition enables quantitative comparisons of transport properties associated with different ocean data sources. The rich structure revealed

by this definition, incorporating dynamical systems theory, relates uncertainty with the stable invariant manifolds of hyperbolic trajectories and goes beyond statistical moments usually used on the field of UQ. This brings new perspectives to our understanding of uncertainty in oceanic processes.

The application of dynamical systems ideas in Chapter 5 provides essential insights into an oil spill dispersion at a large scale in the Eastern Mediterranean. This spill is different from the one discussed in Chapter 3 not only because of the scale involved, but also because the source of the spill is unknown. The observed alignment of oil spills with the attracting material curves (which are related to the unstable LCS) confirms the assumptions made and underscores the potential of the combined technologies based on Copernicus services and dynamical systems in predicting and managing oil spills, thus enhancing environmental protection.

Chapter 6 introduces a novel definition, Backward Lagrangian Uncertainty Quantification (BLUQ), which quantifies the consistency of transport models in describing the source of observations with unknown origins. This definition exhibits a structural link to unstable invariant manifolds of hyperbolic trajectories, and its application to an oil spill accident in the Eastern Mediterranean highlights the performance of different CMEMS products in representing mesoscale and submesoscale structures.

In Chapter 7, a methodology based on ideas of dynamical systems is proposed to assess, using remote observations, the quality of the results of a high-resolution coastal ocean models. The findings emphasize the significant impact of boundary conditions on model performance and identify radiation-nudging lateral boundary conditions as particularly suitable. This methodology enables model adjustment and enhances, to this end, the utilization of satellite imagery in regions with limited in situ observations.

In conclusion, this research has demonstrated the potential of combining advanced simulation techniques, satellite-based observations, and dynamical system theories to improve our approach to marine and coastal issues. This convergence of methodologies provides a new perspective to understand oceanic processes, as well as the tools to proactively address environmental threats, improve the accuracy of our models, and promote a more sustainable relationship with our oceans and coastlines.

8.2. Outlook

The results obtained in this thesis, except for those in Chapter 7, are mainly focused on transport processes at the ocean surface. In this context, several opportunities emerge to expand these results and to explore further applications of the implemented methodologies.

3D Oceanic Transport

Comprehending the complexities of oceanic phenomena requires a transition to a three-dimensional perspective. This is of particular relevance to improve our understanding of significant environmental issues such as the spread and deposition of microplastics in marine ecosystems, which has been widely discussed in (Cai et al., 2023; Sutherland et al., 2023). In order to implement dynamical system concepts in this context, it is essential to incorporate the key concepts outlined in (Branicki and Wiggins, 2009). Recognizing this, we have taken steps in this direction, although referred to other phenomena involving 3D transport in fluids. In (Bruera et al., 2023), we have explored transport across the fully 3D Atlantic Meridional Overturning Circulation (AMOC) and (Amahjour et al., 2023) the dissemination of infectious organisms in a 3D turbulent environment. Studies in high-dimensional systems in which I have been involved, in the context of Celestial Mechanics, is for instance (Daquin et al., 2022).

Advancing Oceanic Models

Emergency services face a major challenge in selecting the most suitable dataset from the large amount of data available (Futch and Allen, 2019). Our research, discussed in Chapters 4 and 6, introduces a novel index for dataset comparison. This approach is further explored by the findings in our preprint (García-Sánchez et al., 2023), emphasizing the importance of robust dataset evaluation methods. Furthermore, the UQ metrics we developed, both forward and backward, have the potential to improve the methodology described in Chapter 7. In this context, our main objective was to acquire reliable oceanic data for the analysis of transport in coastal zones, typically characterized by data scarcity. Such advances offer the potential for the development of high-resolution models in regions with limited available data, addressing a critical concern for emergency services.

As we advance our models, understanding waves and storm surges becomes increasingly crucial, particularly in the context of rising sea levels and concerns about climate change (Vousdoukas et al., 2018). Despite the progress in current large-scale coastal models, there remains a significant gap in representing near-shore dynamics, attributable mainly to their coarse resolutions. These omissions could lead to potential inaccuracies in risk assessments. To address this, we highlight the importance of high-resolution models that intricately detail near-shore processes of waves and storm surges, as reinforced by the collaboration with the Joint Research Centre (JRC) (Mentaschi et al., 2023).

Bibliography

A. Junginger and G. T. Craven and T. Bartsch and others (2016). Transition state geometry of driven chemical reactions on time-dependent double-well potentials. . *Phys. Chem. Chem. Phys*, 18:30270.

A. M. Mancho and D. Small and S. Wiggins (2006). A tutorial on dynamical systems concepts applied to Lagrangian transport in oceanic flows defined as finite time data sets: theoretical and computational issues. . *Physics Reports*, 437(3–4):55–124.

D. B. Haidvogel and A. Beckmann (1999). *Numerical Ocean Circulation Modeling* . Imperial College Press.

D. C. Chapman (1985). Numerical treatment of cross-shelf open boundaries in a barotropic coastal ocean model . *Journal of Physical oceanography*, 15(8):1060–1075.

G. T. Craven and R. Hernandez (2016). Deconstructing field-induced ketene isomerization through Lagrangian descriptors. . *Phys. Chem. Chem. Phys*, 18:4008.

Marcos G Sotillo and P Cerralbo and P Lorente and others (2020). Coastal ocean forecasting in Spanish ports: the SAMOA operational service . *Journal of Operational Oceanography*, 13(1):37–54.

Q. Vanhellemont and K. Ruddick (2018). Atmospheric correction of metre-scale optical satellite data for inland and coastal water applications . *Remote Sensing of Environment*, 216:586–597.

R. A. Flather (1976). A tidal model of the north-west European continental shelf. .

R. He and J. L. Wilkin (2006). Barotropic tides on the southeast New England shelf: A view from a hybrid data assimilative modeling approach . *Journal of Geophysical Research: Oceans*, 111.

Sarah Ben-Nun (2021). *Israel's beaches see more tar as oil spill consequences continue*. Jerusalem Post, https://www.jpost.com/breaking-news/israels-beaches-see-more-tar-as-oil-spill-consequences-continue-661788.

T. Harmel and M. Chami and T. Tormos and others (2018). Sunglint correction of the Multi-Spectral Instrument (MSI)-SENTINEL-2 imagery over inland and sea waters from SWIR bands . *Remote Sensing of Environment*, 204:308–321.

T. Tachim Medjo (2018). Pullback attractors for the multi-layer quasi-geostrophic equations of the ocean . *Nonlinear Analysis: Real World Applications*, 17:365–382.

Adcroft, A. J. (1995). *Numerical algorithms for use in a dynamical model of the ocean*. PhD thesis, University of London 1995.

Agaoglou, M., Aguilar-Sanjuan, B., García-Garrido, V. J., et al. (2019). *Chemical Reactions: A Journey into Phase Space*. zenodo:10.5281/zenodo.3568210.

Agaoglou, M., Aguilar-Sanjuan, B., García-Garrido, V. J., et al. (2020). *Lagrangian Descriptors: Discovery and Quantification of Phase Space Structure and Transport*. zenodo: 10.5281/zenodo.3958985.

Álvaro Peliz, Dubert, J., Haidvogel, D. B., et al. (2003). Generation and unstable evolution of a density-driven eastern poleward current: The iberian poleward current. *Journal of Geophysical Research: Oceans*, 108.

Amahjour, N., García-Sánchez, G., Agaoglou, M., and Mancho, A. M. (2023). Analysis of the spread of sars-cov-2 in a hospital isolation room using cfd and lagrangian coherent structures. *Physica D: Nonlinear Phenomena*, page 133825.

Amo, A., Reffray, G., Sotillo, M. G., et al. (2020). *Product User Manual Atlantic -Iberian Biscay Irish- Ocean Physics Analysis and Forecast Product: IBI_ANALYSIS_FORECAST_PHYS_005_001*. https://resources.marine.copernicus.eu/documents/PUM/CMEMS-IBI-PUM-005-001.pdf.

Aref, H. (1984). Stirring by chaotic advection. *Journal of Fluid Mechanics*, 143:1–21.

Asce (1996). State-of-the-art review of modeling transport and fate of oil spills. committee on modeling oil spills.water resources engineering division. *Journal of Hydraulic Engineering*, 122.

Aurell, E., Boffetta, G., Crisanti, A., Paladin, G., and Vulpiani, A. (1997). Predictability in the large: an extension of the concept of lyapunov exponent. *Journal of Physics A: Mathematical and General*, 30(1):1.

Aznar, R., Sotillo, M., Cailleau, S., et al. (2016). Strengths and weaknesses of the CMEMS forecasted and reanalyzed solutions for the Iberia-Biscay-Ireland (IBI) waters. *Journal of Marine Systems*, 159:1–14.

Balibrea-Iniesta, F., Xie, J., García-Garrido, V. J., et al. (2019). Lagrangian transport across the upper arctic waters in the canada basin. *Quarterly Journal of the Royal Meteorological Society*, 145.

Barker, C. H., Kourafalou, V. H., Beegle-Krause, C. J., et al. (2020). Progress in operational modeling in support of oil spill response. *Journal of Marine Science and Engineering*, 8.

Beljaars, A. (1995). The parametrization of surface fluxes in large-scale models under free convection. *Quarterly Journal of the Royal Meteorological Society*, 121(522):255–270.

Bengtsson, L., Andrae, U., Aspelien, T., et al. (2017). The harmonie-arome model configuration in the aladin-hirlam nwp system. *Monthly Weather Review*, 145.

Bolaños, R., Osuna, P., Wolf, J., Monbaliu, J., and Sanchez-Arcilla, A. (2011). Development of the polcoms–wam current–wave model. *Ocean Modelling*, 36(1-2):102–115.

Branicki, M. and Wiggins, S. (2009). An adaptive method for computing invariant manifolds in non-autonomous, three-dimensional dynamical systems. *Physica D: Nonlinear Phenomena*, 238.

Branicki, M. and Wiggins, S. (2010). Finite-time lagrangian transport analysis: Stable and unstable manifolds of hyperbolic trajectories and finite-time lyapunov exponents. *Nonlinear Processes in Geophysics*, 17.

Bruera, R., Curbelo, J., García-Sánchez, G., and Mancho, A. M. (2023). Mixing and geometry in the north atlantic meridional overturning circulation. *Geophysical Research Letters*, 50(7):e2022GL102244.

Brushett, B. A., King, B. A., and Lemckert, C. (2011). Evaluation of met-ocean forecast data effectiveness for tracking drifters deployed during operational oil spill response in australian waters. *Journal of Coastal Research*, pages 991–994.

Bryan, K. (1963). A numerical investigation of a nonlinear model of a wind-driven ocean. *Journal of the Atmospheric Sciences*, 20.

Budgell, W. P. (2005). Numerical simulation of ice-ocean variability in the barents sea region. *Ocean Dynamics*, 55.

Cai, C., Zhu, L., and Hong, B. (2023). A review of methods for modeling microplastic transport in the marine environments. *Marine Pollution Bulletin*, 193:115136.

Cámara, A. D. L., Mechoso, C. R., Mancho, A. M., et al. (2013). Isentropic transport within the antarctic polar-night vortex: Rossby wave breaking evidence and lagrangian structures. *Journal of the Atmospheric Sciences*, 70.

Capet, A., Fernández, V., She, J., et al. (2020). Operational modeling capacity in european seas–an eurogoos perspective and recommendations for improvement. *Frontiers in Marine Science*, 7.

Carswell, C. (2018). *Unique oil spill in East China Sea frustrates scientists*. Nature, https://doi.org/10.1038/d41586-018-00976-9.

Cartwright, J. H., Feudel, U., Károlyi, G., et al. (2010). Dynamics of finite-size particles in chaotic fluid flows. *Understanding Complex Systems*, 2010.

Casulli, V. and Walters, R. A. (2000). An unstructured grid, three-dimensional model based on the shallow water equations. *International Journal for Numerical Methods in Fluids*, 32.

Cerralbo, P., Grifoll, M., and Espino, M. (2015). Hydrodynamic response in a microtidal and shallow bay under energetic wind and seiche episodes. *Journal of Marine Systems*, 149:1–13.

Chassignet, E. P., Hurlburt, H. E., Smedstad, O. M., Halliwell, G. R., Hogan, P. J., Wallcraft, A. J., Baraille, R., and Bleck, R. (2007). The hycom (hybrid coordinate ocean model) data assimilative system. *Journal of Marine Systems*, 65(1):60–83. Marine Environmental Monitoring and Prediction.

Cheng, Y., Li, X., Xu, Q., et al. (2011). Sar observation and model tracking of an oil spill event in coastal waters. *Marine Pollution Bulletin*, 62.

Ciaim (2018). Informe de colisión del buque RO/PAX VOLCÁN DE TAMASITE contra el dique Nelson Mandela del puerto de Las Palmas de Gran Canaria, el 21 de abril de 2017. CIAIM-05/2018. Ministerio de Fomento. Gobierno de España. 27pp.

Clementi, E., Pistoia, J., Escudier, R., et al. (2019). Mediterranean sea analysis and forecast (cmems med-currents 2016-2019).

CMCC, ORBITALEOS, and ORION (2021). *MEDSLIK-II simulations of transport and fate of a massive oil spill from the Banias electrical plant in the coastal area of Syria*. Cmcc, https://www.cmcc.it/wp-content/uploads/2021/08/CMCC_ORION_ORBITALEOS_Report_n5_V1.pdf.

Consel, C. (1990). The schism manual. *Yale University, New Haven, Connecticut*.

Copernicus Climate Change Service (2023). Era5 single levels reanalysis dataset.

Copernicus Marine Service (2023). Operational Oceanography: History.

Danilov, S., Kivman, G., and Schröter, J. (2004). A finite-element ocean model: Principles and evaluation. *Ocean Modelling*, 6.

Daquin, J., Pédenon-Orlanducci, R., Agaoglou, M., García-Sánchez, G., and Mancho, A. M. (2022). Global dynamics visualisation from lagrangian descriptors. applications to discrete and continuous systems. *Physica D: Nonlinear Phenomena*, 442:133520.

Darwish, A., Norouzi, S., Di Labbio, G., and Kadem, L. (2021). Extracting lagrangian coherent structures in cardiovascular flows using lagrangian descriptors. *Physics of Fluids*, 33(11).

de Crècy, A. (1996). Determination of the uncertainties of the constitutive relationships in the calthare 2 code. Technical report, American Society of Mechanical Engineers, New York, NY (United States).

de la Cámara, A., Mechoso, C. R., Ide, K., et al. (2010). Polar night vortex breakdown and large-scale stirring in the southern stratosphere. *Climate Dynamics*, 35.

Decker, C. J. and Reed, C. (2009). The national oceanographic partnership program: a decade of impacts on oceanography. *Oceanography*, 22(2):208–227.

Delandmeter, P., Lambrechts, J., Legat, V., et al. (2018). A fully consistent and conservative vertically adaptive coordinate system for slim 3d v0.4 with an application to the thermocline oscillations of lake tanganyika. *Geoscientific Model Development*, 11(3):1161–1179.

Di Lorenzo, E., Schneider, N., Cobb, K. M., et al. (2008). North pacific gyre oscillation links ocean climate and ecosystem change. *Geophysical Research Letters*, 35(8).

Dominicis, M. D., Bruciaferri, D., Gerin, R., et al. (2016). A multi-model assessment of the impact of currents, waves and wind in modelling surface drifters and oil spill. *Deep-Sea Research Part II: Topical Studies in Oceanography*, 133.

Dominicis, M. D., Pinardi, N., Zodiatis, G., et al. (2013). Medslik-ii, a lagrangian marine surface oil spill model for short-term forecasting-part 1: Theory. *Geoscientific Model Development*, 6.

Domitr, P., Włostowski, M., Laskowski, R., and Jurkowski, R. (2022). Comparison of inverse uncertainty quantification methods for critical flow test. *Energy*, page 125640.

Dritschel, D. G. and Ambaum, M. H. (1997). A contour-advective semi-lagrangian numerical algorithm for simulating fine-scale conservative dynamical fields. *Quarterly Journal of the Royal Meteorological Society*, 123.

EFE (2017). *La punta de la mancha, de 13 km. de largo, ya está a la altura de La Garita pero a 1.000 metros de la costa*. Telde Actualidad, https://www.teldeactualidad.com/hemeroteca/noticia/medioambiente/2017/04/23/2402.html.

ESA (1998). *Oil pollution monitoring*. ESA brochure: ERS and its applications–Marine, BR-128, 1, https://earth.esa.int/web/guest/-/ers-and-its-applications-marine-4680.

European Commission (2014). *About Copernicus*. European Space Agency, https://www.copernicus.eu/en/about-copernicus.

Federico, I., Pinardi, N., Coppini, G., et al. (2017). Coastal ocean forecasting with an unstructured grid model in the southern adriatic and northern ionian seas. *Natural Hazards and Earth System Sciences*, 17.

Feng, D., Passalacqua, P., and Hodges, B. R. (2019). Innovative approaches for geometric uncertainty quantification in an operational oil spill modeling system. *Journal of Marine Science and Engineering*, 7.

Fernandes-Salvador, J. A., Davidson, K., Sourisseau, M., Revilla, M., Schmidt, W., Clarke, D., Miller, P. I., Arce, P., Fernández, R., Maman, L., et al. (2021). Current status of forecasting toxic harmful algae for the north-east atlantic shellfish aquaculture industry. *Frontiers in Marine Science*, 8:666583.

Fingas, M. (2015). *Handbook of Oil Spill Science and Technology*.

Frenklach, M., Packard, A., Garcia-Donato, G., et al. (2016). Comparison of statistical and deterministic frameworks of uncertainty quantification. *SIAM-ASA Journal on Uncertainty Quantification*, 4.

Fringer, O. B., Gerritsen, M., and Street, R. L. (2006). An unstructured-grid, finite-volume, nonhydrostatic, parallel coastal ocean simulator. *Ocean Modelling*, 14.

Froyland, G. and Padberg-Gehle, K. (2014). Almost-invariant and finite-time coherent sets: Directionality, duration, and diffusion. volume 70.

Futch, V. and Allen, A. (2019). Search and rescue applications: On the need to improve ocean observing data systems in offshore or remote locations. *Frontiers in Marine Science*, 6.

García-Garrido, V. J., Balibrea-Iniesta, F., Wiggins, S., Mancho, A. M., and Lopesino, C. (2018). Detection of phase space structures of the cat map with lagrangian descriptors. *Regular and Chaotic Dynamics*, 23:751–766.

García-Garrido, V. J., Curbelo, J., Mancho, A. M., et al. (2018). The application of lagrangian descriptors to 3d vector fields. *Regular and Chaotic Dynamics*, 23.

Garcia-Garrido, V. J., Mancho, A. M., Wiggins, S., et al. (2015). A dynamical systems approach to the surface search for debris associated with the disappearance of flight mh370. *Nonlinear Processes in Geophysics*, 22.

García-Garrido, V. J., Ramos, A., Mancho, A. M., et al. (2016). A dynamical systems perspective for a real-time response to a marine oil spill. *Marine Pollution Bulletin*, 112:1–10.

García-Sánchez, G., Agaoglou, M., Smith, E. M. C., and Mancho, A. M. (2023). Validation of the transport capacity of ocean models: a lagrangian uncertainty quantification approach. Preprint.

García-Sánchez, G., Mancho, A., and Wiggins, S. (2022a). A bridge between invariant dynamical structures and uncertainty quantification. *Communications in Nonlinear Science and Numerical Simulation*, 104:106016.

García-Sánchez, G., Mancho, A. M., Ramos, A. G., et al. (2022b). Structured pathways in the turbulence organizing recent oil spill events in the eastern mediterranean. *Scientific Reports*, 12:3662.

García-Sánchez, G., Mancho, A. M., Agaoglou, M., and Wiggins, S. (2023a). New links between invariant dynamical structures and uncertainty quantification. *Physica D: Nonlinear Phenomena*, 453:133826.

García-Sánchez, G., Mancho, A. M., Ramos, A. G., Coca, J., and Madrid, J. A. J. (2023b). Dynamical systems for remote validation of very high-resolution ocean models. Preprint.

García-Sánchez, G., Mancho, A. M., Ramos, A. G., Coca, J., Pérez-Gómez, B., Álvarez Fanjul, E., Sotillo, M. G., García-León, M., García-Garrido, V. J., and Wiggins, S. (2021). Very high resolution tools for the monitoring and assessment of environmental hazards in coastal areas. *Frontiers in Marine Science*, 7.

Giles, M. A. (1979). Marine pollutant transfer. *Journal of the Fisheries Research Board of Canada*, 36.

Gille, S. and Smith, S. L. (2003). Bathymetry and ocean circulation. *Charting the Secret World of the Ocean Floor. The GEBCO Project 1903-2003*.

Griffies, S. M., Böning, C., Bryan, F. O., et al. (2000). Developments in ocean climate modelling. *Ocean Modelling*, 2.

Grifoll, M., Gracia, V., Aretxabaleta, A., et al. (2014). Formation of fine sediment deposit from a flash flood river in the m editerranean s ea. *Journal of Geophysical Research: Oceans*, 119(9):5837–5853.

Grifoll, M., Jordà, G., Sotillo, M. G., et al. (2012). Water circulation forecasting in spanish harbours. *Scientia Marina*, 76.

Haidvogel, D. B., Arango, H., Budgell, W. P., et al. (2008). Ocean forecasting in terrain-following coordinates: Formulation and skill assessment of the regional ocean modeling system. *Journal of Computational Physics*, 227:3595–3624.

Haidvogel, D. B., Arango, H. G., Hedstrom, K., et al. (2000). Model evaluation experiments in the north atlantic basin: Simulations in nonlinear terrain-following coordinates. *Dynamics of Atmospheres and Oceans*, 32.

Haller, G. (2001). Distinguished material surfaces and coherent structures in three-dimensional fluid flows. *Physica D: Nonlinear Phenomena*, 149.

Haller, G. (2002). Lagrangian coherent structures from approximate velocity data. *Phys. Fluids*, 14:1851–1861.

Haller, G. and Yuan, G. (2000). Lagrangian coherent structures and mixing in two-dimensional turbulence. *Physica D: Nonlinear Phenomena*, 147:352–370.

Haza, A. C., Griffa, A., Martin, P., et al. (2007). Model-based directed drifter launches in the Adriatic Sea: Results from the DART experiment. *Geophys. Res. Lett*, 34:L10605.

Haza, A. C., Özgökmen, T., Griffa, A., et al. (2010). Transport properties in small-scale coastal flows: relative dispersion from VHF radar measurements in the Gulf of La Spezia. *Ocean Dynam.*, 60:861–882.

Hedström, K. S. (1994). *Technical manual for a coupled sea-ice/ocean circulation model (version 1)*. Minerals Management Service, Alaska OCS Region.

Hersbach, H., B. Bell, P. B., et al. (2020). The era5 global reanalysis. *Quarterly Journal of the Royal Meteorological Society*, 146(730):1999–2049.

Hong, S., Noh, Y., and Dudhia, J. (2006). A new vertical diffusion package with an explicit treatment of entrainment processes. *Monthly weather review*, 134(9):2318–2341.

Hu, Z.-Z., Xue, Y., Huang, B., Kumar, A., Wen, C., Xie, P., Zhu, J., Pegion, P. J., Ren, L., and Wang, W. (2022). Global ocean monitoring and prediction at noaa climate prediction center: 15 years of operations. *Bulletin of the American Meteorological Society*, 103(12):E2701–E2718.

Huntley, H. S., Lipphardt, B. L., and Kirwan, A. D. (2011). Lagrangian predictability assessed in the east china sea. *Ocean Modelling*, 36.

Ide, K., Small, D., and Wiggins, S. (2002). Distinguished hyperbolic trajectories in time-dependent fluid flows: Analytical and computational approach for velocity fields defined as data sets. *Nonlinear Processes in Geophysics*, 9.

Ivorra, B., Gomez, S., Glowinski, R., et al. (2017). Nonlinear advection–diffusion–reaction phenomena involved in the evolution and pumping of oil in open sea: Modeling, numerical simulation and validation considering the prestige and oleg naydenov oil spill cases. *Journal of Scientific Computing*, 70.

Jackett, D. R. and Mcdougall, T. J. (1995). Minimal adjustment of hydrographic profiles to achieve static stability. *Journal of Atmospheric and Oceanic Technology*, 12(2):381–389.

Ju, N., Small, D., and Wiggins, S. (2003). Existence and computation of hyperbolic trajectories of aperiodically time dependent vector fields and their approximations. *International Journal of Bifurcation and Chaos in Applied Sciences and Engineering*, 13.

Kaplan-Zantopp, M. (2021). *Israel oil spill: How did it happen and what will we do going forward?* Jerusalem Post, https://www.jpost.com/israel-news/israel-oil-spill-how-did-it-happen-and-what-will-we-do-going-forward-660242.

Kaszás, B. and Haller, G. (2020). Universal upper estimate for prediction errors under moderate model uncertainty. *Chaos: An Interdisciplinary Journal of Nonlinear Science*, 30(11).

Katsanikas, M., Agaoglou, M., and Montoya, F. G. (2022). Introduction to special issue: Chaos indicators, phase space and chemical reaction dynamics. *Physica D: Nonlinear Phenomena*, 439:133385.

Kirwan, A. D., Toner, M., and Kantha, L. (2003). Predictability, uncertainty, and hyperbolicity in the ocean. volume 41.

Kourafalou, V. H., Mey, P. D., Hénaff, M. L., et al. (2015). Coastal ocean forecasting: System integration and evaluation. *Journal of Operational Oceanography*, 8.

Kundu, A. (2021). *Syrian Oil Spill Spreads Across The Mediterranean, Endangers Northern Cyprus Coast*. FleetMon, https://www.fleetmon.com/maritime-news/2021/35177/syrian-oil-spill-spreads-across-mediterranean-enda/.

Kuznetsov, L., M., T., D., K. A., et al. (2002). The Loop Current and adjacent rings delineated by Lagrangian analysis of the near-surface flow. *J. Mar. Res.*, 60:405–429.

Large, W. G. and Yeager, S. (2004). *Diurnal to decadal global forcing for ocean and sea-ice models: The data sets and flux climatologies*. University Corporation for Atmospheric Research., http://www.doi.org/10.5065/D6KK98Q6.

Le Traon, P. Y., Reppucci, A., Alvarez Fanjul, E., Aouf, L., Behrens, A., Belmonte, M., Bentamy, A., Bertino, L., Brando, V. E., Kreiner, M. B., et al. (2019). From observation to information and users: The copernicus marine service perspective. *Frontiers in Marine Science*, 6:234.

Lekien, F. and Marsden, J. (2005). Tricubic interpolation in three dimensions. *International Journal for Numerical Methods in Engineering*, 63.

Liu, Y., Weisberg, R. H., Vignudelli, S., et al. (2014). Evaluation of altimetry-derived surface current products using lagrangian drifter trajectories in the eastern gulf of mexico. *Journal of Geophysical Research: Oceans*, 119.

Lopesino, C., Balibrea, F., Wiggins, S., et al. (2015). Lagrangian descriptors for two dimensional, area preserving, autonomous and nonautonomous maps. *Communications in Nonlinear Science and Numerical Simulation*, 27(1–3):40–51.

Lopesino, C., Balibrea-Iniesta, F., García-Garrido, V. J., et al. (2017). A theoretical framework for lagrangian descriptors. *International Journal of Bifurcation and Chaos*, 27:1730001.

Lorente, P., Sotillo, M. G., Amo-Baladrón, A., et al. (June 12–14, 2019). *Proceedings of the 19th International Conference on Computational Science*, volume Part IV, chapter The NARVAL Software Toolbox in Support of Ocean Models Skill Assessment at Regional and Coastal Scales., pages Doi: 10.1007/978–3–030–22747–0_25. ICCS 2019, Faro, Portugal.

Lorenzo, E. D., Schneider, N., Cobb, K. M., et al. (2008). North pacific gyre oscillation links ocean climate and ecosystem change. *Geophysical Research Letters*, 35.

Madec, G. and the NEMO team (2008). *NEMO ocean engine*. Institut Pierre-Simon Laplace (IPSL), France, No 27, ISSN No 1288-1619., https://zenodo.org/record/3248739#.X0UXgpNLgSQ.

Madrid, J. A. and Mancho, A. M. (2009). Distinguished trajectories in time dependent vector fields. *Chaos*, 19:013111.

Malanotte-Rizzoli, P., Hedstrom, K., Arango, H., and Haidvogel, D. B. (2000). Water mass pathways between the subtropical and tropical ocean in a climatological simulation of the north atlantic ocean circulation. *Dynamics of Atmospheres and Oceans*, 32(3-4):331–371.

Malenovskỳ, Z., Rott, H., Cihlar, J., Schaepman, M. E., García-Santos, G., Fernandes, R., and Berger, M. (2012). Sentinels for science: Potential of sentinel-1,-2, and-3 missions for scientific observations of ocean, cryosphere, and land. *Remote Sensing of environment*, 120:91–101.

Mancho, A. M., Small, D., and Wiggins, S. (2004). Computation of hyperbolic trajectories and their stable and unstable manifolds for oceanographic flows represented as data sets. *Nonlinear Processes in Geophysics*, 11.

Mancho, A. M., Small, D., and Wiggins, S. (2006). A tutorial on dynamical systems concepts applied to lagrangian transport in oceanic flows defined as finite time data sets: Theoretical and computational issues. *Physics Reports*, 437.

Mancho, A. M., Small, D., Wiggins, S., et al. (2003). Computation of stable and unstable manifolds of hyperbolic trajectories in two-dimensional, aperiodically time-dependent vector fields. *Physica D: Nonlinear Phenomena*, 182.

Mancho, A. M., Wiggins, S., Curbelo, J., et al. (2013). Lagrangian descriptors: A method for revealing phase space structures of general time dependent dynamical systems. *Communications in Nonlinear Science and Numerical Simulation*, 18(12):3530–3557.

Marchesiello, P., McWilliams, J. C., and Shchepetkin, A. (2001). Open boundary conditions for long-term integration of regional oceanic models. *Ocean Modelling*, 3.

Marta-Almeida, M., Ruiz-Villarreal, M., Pereira, J., et al. (2013). Efficient tools for marine operational forecast and oil spill tracking. *Marine Pollution Bulletin*, 71.

Martin, P. J., Barron, C. N., Smedstad, L. F., Campbell, T. J., Wallcraft, A. J., Rhodes, R. C., Rowley, C., Townsend, T. L., and Carroll, S. N. (2009). User's manual for the navy coastal ocean model (ncom) version 4.0. Technical report, Naval Research Lab Stennis Space Center MS Ocean Dynamics and Prediction Branch.

Max Planck Institute for Meteorology (2023). Icon public.

Maxey, M. R. and Riley, J. J. (1983). Equation of motion for a small rigid sphere in a nonuniform flow. *Physics of Fluids*, 26.

McIlroy, J. W., Smith, R. W., and McGuffin, V. L. (2018). Fixed- and variable-temperature kinetic models to predict evaporation of petroleum distillates for fire debris applications. *Separations*, 5.

Mendoza, C., Mancho, A., and Wiggins, S. (2014). Lagrangian descriptors and the assessment of the predictive capacity of oceanic data sets. *Nonlinear Processes in Geophysics*, 21(3):677–689.

Mendoza, C. and Mancho, A. M. (2010). Hidden geometry of ocean flows. *Physical Review Letters*, 105(3):038501.

Mendoza, C. and Mancho, A. M. (2012). Review article: "the lagrangian description of aperiodic flows: A case study of the kuroshio current". *Nonlinear Processes in Geophysics*, 19.

Mentaschi, L., Vousdoukas, M. I., García-Sánchez, G., Fernández-Montblanc, T., Roland, A., Voukouvalas, E., Federico, I., Abdolali, A., Zhang, Y. J., and Feyen, L. (2023). A global unstructured, coupled, high-resolution hindcast of waves and storm surge. *Frontiers in Marine Science*, 10.

Mezić, I. and Wiggins, S. (1999). A method for visualization of invariant sets of dynamical systems based on the ergodic partition. *Chaos*, 9.

Monitor, A. (2021). *Oil spill in Mediterranean reaches besieged Gaza Strip*. Al-Monitor, https://www.al-monitor.com/originals/2021/03/gaza-beach-oil-spill-israel-environment-pollution.html.

Monroy, P. (2019). *Doctoral Thesis: Lagrangian Studies of Sedimentation and Transport. Impact on marine ecosystems.* Universitat de les Illes Balears, https://ifisc.uib-csic.es/es/publications/lagrangian-studies-of-sedimentation-and-transport/.

Monroy, P., Hernández-García, E., Rossi, V., et al. (2017). Modeling the dynamical sinking of biogenic particles in oceanic flow. *Nonlinear Processes in Geophysics*, 24.

Montero, A. R. (2017). La reducción de la mancha de gasoil un 80% permite abrir las ocho playas. *La Provincia*.

Moser, J. (1956). The analytic invariants of an area-preserving mapping near a hyperbolic fixed point. *Communications on pure and applied mathematics*, 9:673–692.

Muhammad, A. (2015). Exploring salinity issues in the texas coast using selfe: Semi-implicit finite-element/volume eulerian-lagrangian algorithm.

Nagheeby, M. and Kolahdoozan, M. (2010). Numerical modeling of two-phase fluid flow and oil slick transport in estuarine water. *International Journal of Environmental Science and Technology*, 7.

National Centers for Environmental Information (2023). Global forecast system.

Nechad, B., Ruddick, K., and Neukermans, G. (2009). Calibration and validation of a generic multisensor algorithm for mapping of turbidity in coastal waters . *SPIE Europe Remote Sensing. International Society for Optics and Photonics*, page 74730H–74730H.

Nechad, B., Ruddick, K., and Neukermans, G. (2010). Calibration and validation of a generic multisensor algorithm for mapping of total suspended matter in turbid waters . *Remote Sensing of Environment*, 114(4):854–866.

Nese, J. M. (1989). Quantifying local predictability in phase space. *Physica D: Nonlinear Phenomena*, 35.

News Agencies (2021). *Aljazeera*. Aljazeera, https://www.aljazeera.com/news/2021/2/27/lebanon-begins-cleaning-beaches-after-oil-spill.

O'Connor, W. P. (1991). A user's manual for the princeton numerical ocean model. Technical report, Institute for Naval Oceanography Stennis Space Center MS.

Olascoaga, M., Beron-Vera, F., Brand, L., and Kocak, H. (2008). Tracing the early development of harmful algal blooms on the west florida shelf with the aid of lagrangian coherent structures. *Journal of Geophysical Research: Oceans*, 113(C12).

Olascoaga, M. J. and Haller, G. (2012). Forecasting sudden changes in environmental pollution patterns. *Proceedings of the National Academy of Sciences of the United States of America*, 109.

Ottino, J. M., Jana, S. C., and Chakravarthy, V. S. (1994). From reynolds's stretching and folding to mixing studies using horseshoe maps. *Physics of Fluids*, 6.

Palis, J. (1969). On morse-smale dynamical systems. *Topology*, 8.

Pavlakis, P., Sieber, A., and Alexandry, S. (1996). Monitoring oil-spill pollution in the mediterranean with ers sar. *Earth Observation Quarterly*, 52.

Petruzzi, A. (2019). The casualidad method for uncertainty evaluation of best-estimate system thermal-hydraulic calculations. *Nuclear Technology*, 205(12):1554–1566.

Pisano, A., Bignami, F., and Santoleri, R. (2015). Oil spill detection in glint-contaminated near-infrared modis imagery. *Remote Sensing*, 7.

Pisano, A., Marullo, S., Artale, V., Falcini, F., Yang, C., Leonelli, F. E., Santoleri, R., and Buongiorno Nardelli, B. (2020). New evidence of mediterranean climate change and variability from sea surface temperature observations. *Remote Sensing*, 12(1):132.

Polidura, A. (2021). *Israel's oil spill now affects entire Lebanese coastline*. Atalayar, https://atalayar.com/en/content/israels-oil-spill-now-affects-entire-lebanese-coastline.

Prants, S. V., Budyansky, M. V., and Uleysky, M. Y. (2014). Lagrangian study of surface transport in the kuroshio extension area based on simulation of propagation of fukushima-derived radionuclides. *Nonlinear Processes in Geophysics*, 21.

Prants, S. V., Uleysky, M. Y., and Budyansky, M. V. (2011). Numerical simulation of propagation of radioactive pollution in the ocean from the fukushima dai-ichi nuclear power plant. *Doklady Earth Sciences*, 439.

Ramos, A. G., Martel, A., Codd, G. A., Soler, E., Coca, J., Redondo, A., Morrison, L. F., Metcalf, J. S., Ojeda, A., Suárez, S., et al. (2005). Bloom of the marine diazotrophic cyanobacterium trichodesmium erythraeum in the northwest african upwelling. *Marine Ecology Progress Series*, 301:303–305.

Revuelta, F., Benito, R. M., and Borondo, F. (2019). Unveiling the chaotic structure in phase space of molecular systems using lagrangian descriptors. *Physical Review E*, 99:032221.

Robbin, J., Palis, J., and de Melo, W. (1984). Geometric theory of dynamical systems: An introduction. *The American Mathematical Monthly*, 91.

Rutgers Staff (2021). *Oil spill off Israel reaches south Lebanese beaches*. Rutgers, https://www.reuters.com/article/us-israel-environment-oil-spill-lebanon-idUSKBN2AM19V.

Rypina, I. I., Scott, S. E., Pratt, L. J., et al. (2011). Investigating the connection between complexity of isolated trajectories and lagrangian coherent structures. *Nonlinear Processes in Geophysics*, 18.

Schrope, M. (2013). Minor oil spills are often bigger than reported. *Nature*.

Serra, M., Sathe, P., Rypina, I., Kirincich, A., Ross, S. D., Lermusiaux, P., Allen, A., Peacock, T., and Haller, G. (2020). Search and rescue at sea aided by hidden flow structures. *Nature communications*, 11(1):2525.

Shadden, S. C., Lekien, F., and Marsden, J. E. (2005). Definition and properties of lagrangian coherent structures from finite-time lyapunov exponents in two-dimensional aperiodic flows. *Physica D: Nonlinear Phenomena*, 212.

Shadden, S. C., Lekien, F., Paduan, J. D., et al. (2009). The correlation between surface drifters and coherent structures based on high-frequency radar data in Monterey Bay. *Deep Sea Res. II*, 56:161–172.

Shapiro, R. (1970). Smoothing, filtering, and boundary effects. *Reviews of Geophysics*, 8.

Shchepetkin, A. F. and Mcwilliams, J. C. (1998). Quasi-monotone advection schemes based on explicit locally adaptive dissipation. *Monthly Weather Review*, 126.

Shchepetkin, A. F. and McWilliams, J. C. (2003). A method for computing horizontal pressure-gradient force in an oceanic model with a nonaligned vertical coordinate. *Journal of Geophysical Research: Oceans*, 108.

Shchepetkin, A. F. and McWilliams, J. C. (2005). The regional oceanic modeling system (roms): A split-explicit, free-surface, topography-following-coordinate oceanic model. *Ocean Modelling*, 9.

Shu, Y., Wang, D., Feng, M., et al. (2018). The contribution of local wind and ocean circulation to the interannual variability in coastal upwelling intensity in the northern south china sea. *Journal of Geophysical Research: Oceans*, 123.

Shu, Y., Xue, H., Wang, D., et al. (2014). Meridional overturning circulation in the south china sea envisioned from the high-resolution global reanalysis data glba0.08. *Journal of Geophysical Research: Oceans*, 119.

Song, Y. and Haidvogel, D. (1994). A semi-implicit ocean circulation model using a generalized topography-following coordinate system. *Journal of Computational Physics*, 115.

Sotillo, M. G., Cailleau, S., Lorente, P., et al. (2015). The myocean ibi ocean forecast and reanalysis systems: Operational products and roadmap to the future copernicus service. *Journal of Operational Oceanography*, 8(1):63–79.

Sotillo, M. G., Cerralbo, P., Lorente, P., et al. (2020). Coastal ocean forecasting in spanish ports: the samoa operational service. *Journal of Operational Oceanography*, 13(1):37–54.

Speetjens, M. F., Clercx, H. J., and van Heijst, G. J. (2004). A numerical and experimental study on advection in three-dimensional stokes flows. *Journal of Fluid Mechanics*, 514:77–105.

Stolzenbach, K. D., Madsen, O. S., Adams, E. E., et al. (1977). Review and evaluation of basic techniques for predicting the behavior of surface oil slicks. *MIT Dep Civ Eng Ralph M. Parsons Lab Water Resour Hydrodyn Rep*.

Sullivan, T. J. (2015). *Introduction to Uncertainty Quantification*. Springer.

Surkes, S. (2021). *Satellite images of oil slicks off coast show recent spill far from a one-off*. Times of Israel, https://www.timesofisrael.com/satellite-images-of-oil-slicks-off-coast-show-recent-spill-far-from-a-one-off/.

Susuki, Y. and Mezić, I. (2009). Ergodic partition of phase space in continuous dynamical systems.

Sutherland, B. R., DiBenedetto, M., Kaminski, A., and Van Den Bremer, T. (2023). Fluid dynamics challenges in predicting plastic pollution transport in the ocean: A perspective. *Physical Review Fluids*, 8(7):070701.

T. Joffre and R. Tercatin (2021). *Israel investigates tar spill calamity, places inquiry under gag order*. Jerusalem Post, https://www.jpost.com/israel-news/israel-oil-spill-disaster-investigation-details-placed-under-censor-659765.

Tercatin, R. (2021). *Damage to Israeli marine environment from tar spill extreme, experts say*. Jerusalem Post, https://www.jpost.com/israel-news/damage-to-israeli-marine-environment-from-tar-spill-extreme-experts-say-659716.

Umgiesser, G., Canu, D. M., Cucco, A., et al. (2004). A finite element model for the venice lagoon. development, set up, calibration and validation. *Journal of Marine Systems*, 51.

Umlauf, L. and Burchard, H. (2003). A generic length-scale equation for geophysical turbulence models. *Journal of Marine Research*, 61(2):235–265.

Van Sebille, E., Aliani, S., Law, K. L., Maximenko, N., Alsina, J. M., Bagaev, A., Bergmann, M., Chapron, B., Chubarenko, I., Cózar, A., et al. (2020). The physical oceanography of the transport of floating marine debris. *Environmental Research Letters*, 15(2):023003.

Vanhellemont, Q. (2019). Adaptation of the dark spectrum fitting atmospheric correction for aquatic applications of the landsat and sentinel-2 archives. *Remote Sensing of Environment*, 225:175–192.

Vieira, G. S., Rypina, I. I., and Allshouse, M. R. (2020). Uncertainty quantification of trajectory clustering applied to ocean ensemble forecasts. *Fluids*, 5.

Vousdoukas, M. I., Mentaschi, L., Voukouvalas, E., et al. (2018). Global probabilistic projections of extreme sea levels show intensification of coastal flood hazard. *Nature Communications*, 9.

Walters, R. A. (2005). Coastal ocean models: Two useful finite element methods. *Continental Shelf Research*, 25.

Wang, P., Song, Y. T., Chao, Y., and Zhang, H. (2005). Parallel computation of the regional ocean modeling system. *The International Journal of High Performance Computing Applications*, 19(4):375–385.

Warner, J. C., Armstrong, B., He, R., and Zambon, J. B. (2010). Development of a coupled ocean–atmosphere–wave–sediment transport (coawst) modeling system. *Ocean modelling*, 35(3):230–244.

Warner, J. C., Sherwood, C. R., Arango, H. G., et al. (2005). Performance of four turbulence closure models implemented using a generic length scale method. *Ocean Modelling*, 8.

Westerink, J. J., Luettich Jr, R., Blain, C., and Scheffner, N. W. (1994). Adcirc: an advanced three-dimensional circulation model for shelves, coasts, and estuaries. report 2. user's manual for adcirc-2ddi. Technical report, Army engineer waterways experiment stations Vicksburg MS.

Wiggins, S. (1992). *Chaotic Transport in Dynamical Systems*. Springer-Verlag, New York.

Wiggins, S. (2003). *Introduction to applied nonlinear dynamical systems and applications*. Springer-Verlag Heidelberg.

Wiggins, S. (2005). The dynamical systems approach to lagrangian transport in oceanic flows. *Annu. Rev. Fluid Mech.*, 37:295–328.

Wikimedia Foundation (2021). *2021 Mediterranean Oil Spill.* Wikipedia, https://en.wikipedia.org/wiki/2021_Mediterranean_oil_spill.

Wilcox, D. C. et al. (1998). *Turbulence modeling for CFD*, volume 2. DCW industries La Canada, CA.

Wilkin, J. L., Arango, H. G., Haidvogel, D. B., et al. (2005). A regional ocean modeling system for the long-term ecosystem observatory. *Journal of Geophysical Research: Oceans*, 110.

Wu, X., Kozlowski, T., Meidani, H., and Shirvan, K. (2018). Inverse uncertainty quantification using the modular bayesian approach based on gaussian process, part 2: Application to trace. *Nuclear Engineering and Design*, 335:417–431.

Xu, Q., Li, X., Wei, Y., et al. (2013). Satellite observations and modeling of oil spill trajectories in the bohai sea. *Marine Pollution Bulletin*, 71.

Z. Rinat and A. Ben Zikri (2021). *Oil Spill Off Israel's Coast Is Its Worst Maritime Pollution in Decades, and Cleanup 'Could Take Years'*. Haaretz, https://www.haaretz.com/israel-news/.premium-oil-spill-off-israel-s-coast-is-its-worst-maritime-pollution-in-decades-1.9553528.

Zafirakou, A. (2019). *Oil Spill Dispersion Forecasting Models*.

Zhang, X., Cheng, L., Zhang, F., Wu, J., Li, S., Liu, J., Chu, S., Xia, N., Min, K., Zuo, X., et al. (2020). Evaluation of multi-source forcing datasets for drift trajectory prediction using lagrangian models in the south china sea. *Applied Ocean Research*, 104:102395.

Zodiatis, G., Lardner, R., Alves, T. M., et al. (2017). Oil spill forecasting (prediction). *Journal of Marine Research*, 75.